

2003 SUMMER RESEARCH PROGRAM FOR HIGH SCHOOL JUNIORS

AT THE

UNIVERSITY OF ROCHESTER'S

LABORATORY FOR LASER ENERGETICS

STUDENT RESEARCH REPORTS

PROGRAM COORDINATOR

Dr. R. Stephen Craxton

March 2004

Laboratory Report 332

2003 SUMMER RESEARCH PROGRAM FOR HIGH SCHOOL JUNIORS

AT THE

UNIVERSITY OF ROCHESTER'S

LABORATORY FOR LASER ENERGETICS

STUDENT RESEARCH REPORTS

PROGRAM COORDINATOR

Dr. R. Stephen Craxton

LABORATORY FOR LASER ENERGETICS

University of Rochester

250 East River Road

Rochester, NY 14623-1299

During the summer of 2003, 15 students from Rochester-area high schools participated in the Laboratory for Laser Energetics' Summer High School Research Program. The goal of this program is to excite a group of high school students about careers in the areas of science and technology by exposing them to research in a state-of-the-art environment. Too often, students are exposed to "research" only through classroom laboratories, which have prescribed procedures and predictable results. In LLE's summer program, the students experience many of the trials, tribulations, and

rewards of scientific research. By participating in research in a real environment, the students often become more excited about careers in science and technology. In addition, LLE gains from the contributions of the many highly talented students who are attracted to the program.

The students spent most of their time working on their individual research projects with members of LLE's scientific staff. The projects were related to current research activities at LLE and covered a broad range of areas of interest including laser optics modeling, laser-beam alignment, analysis of OMEGA implosion experiments, plasma physics modeling, cryogenic target physics, liquid crystal chemistry, molecular modeling, and the development and control of laser fusion diagnostics. The students, their high schools, their LLE supervisors, and their project titles are listed in the table. Their written reports are collected in this volume.

The students attended weekly seminars on technical topics associated with LLE's research. Topics this year included lasers, fusion, holographic optics, atomic force microscopy, experimental error analysis, computer-controlled optics manufacturing, and microcontrollers and their applications. The students also received safety training, learned how to give scientific presentations, and were introduced to LLE's resources, especially the computational facilities.

The program culminated on 27 August with the "High School Student Summer Research Symposium," at which the students presented the results of their research to an audience including parents, teachers, and LLE staff. Each student spoke for approximately ten minutes and answered questions. At the symposium the William D. Ryan Inspirational Teacher award was presented to Mr. Michael Carges, a former physics

teacher at Pittsford-Mendon High School and currently at Greece Athena High School. This annual award honors a teacher, nominated by alumni of the LLE program, who has inspired outstanding students in the areas of science, mathematics, and technology. Mr. Carges was nominated by Joy Yuan and Siddhartha Ghosh, participants in the 2002 Summer Program.

A total of 160 high school students have participated in the program since it began in 1989. The students this year were selected from approximately 60 applicants. Each applicant submitted an essay describing their interests in science and technology, a copy of their transcript, and a letter of recommendation from a science or math teacher.

In the past, several participants of this program have gone on to become semifinalists and finalists in the prestigious, nationwide Intel Science Talent Search. This year, the program was particularly productive, resulting in the selection of three students (Rohan Kekre, Nadine Lippa, and Anthony Noto) as among the 300 semifinalists nationwide in this competition.

LLE plans to continue this program in future years. The program is strictly for students from Rochester-area high schools who have just completed their junior year. Applications are generally mailed out in early February with an application deadline near the end of March. For more information about the program or an application form, please contact Dr. R. Stephen Craxton at LLE.

This program was supported by the U.S. Department of Energy Office of Inertial Confinement Fusion under Cooperative Agreement No. DE-FC03-92SF19460.

High School Students and Projects (Summer 2003)

Name	High School	Supervisor	Project Title
Christine Beaty	Livonia High School	C. Stoeckl	Controlling Scientific Instruments Using JAVA on LINUX
Ryan Blair	Canandaigua Academy	R. Boni/ M. Millechia	Characterization of the OMEGA Sixty-Channel UV Spectrometer
George Dahl	Allendale Columbia	M. Guardalben	Pulse-Shaping Effects in Optical Parametric Amplifications
Margot Epstein	Sodus Central High School	W. Bittle/ J. Depatie	Automated Laser-Beam Steering
Wen-fai Fong	Pittsford Sutherland	R. Epstein	Non-LTE Effects on the Speed of Sound in Plasmas
Christopher Forbes	Eastridge Senior High	P. Jaanimagi	Energy and Angular Distributions of Secondary Electrons Under High Electric Field
Nathaniel Gindele	Brighton High School	J. Knauer	Analyzing an Array of Diamond Photodetector Detectors
Rohan Kekre	McQuaid Jesuit	S. Craxton	Tuning Multiple Triplers Using a UV Spectrometer
Kathryn Knowles	Churchville-Chili	J. Delettrez	Analysis of Silicon Emission in Rayleigh–Taylor Unstable Imploded Layered Targets
Nadine Lippa	Byron-Bergen	A. Schmid/ S. Lukishova	Single Dye Molecule Fluorescence in Liquid Crystal Hosts
Anthony Noto	Greece Athena	K. Marshall	Development of Weighted Chirality Indices: Their Use in Modeling Nickel Dithiolene Systems
Benjamin Schmitt	Greece Arcadia	F. Marshall	X-Ray Microscope Mirror Characterization
Nicole Toscano	Greece Arcadia	V. Smalyuk	Compressed Core Characterization of a Cryogenic D ₂ Target at Peak Neutron Production
Cam Tran	Wilson Magnet	K. Marshall	Photochemically Induced Alignment of Liquid Crystals on a Polymer Surface
Michael Wozniak	Greece Athena	D. Harding/ S. Craxton	The Effect of Nonuniform Illumination on the Shape of Deuterium Ice Layers

Controlling Scientific Instruments Using JAVA on LINUX

Christine Beaty

Controlling Scientific Instruments Using JAVA on LINUX

C. Beaty
Advised by Dr. Christian Stoeckl

Laboratory for Laser Energetics
University of Rochester
250 East River Road
Rochester, NY 14623

Abstract

Motivated by the increased use of the Linux operating system at LLE, a program has been built in that environment to control the operation of CCD cameras. CCD cameras are used in several diagnostics, including UV spectrometers and streak cameras, that analyze the 60 of the OMEGA laser. This program, written in Java, allows users with little or no knowledge of the intricacies of CCD camera command logic to set up the camera and acquire data in the form of an image. Among the issues examined during programming lay the optimization of reading the image, leading to faster acquisition of the image, and the synchronization of threads in a multi-threaded program, which ensures that the camera control program will adequately respond to the user. The program was created using special care to facilitate easy reuse of the code for similar applications without requiring considerable modification.

Introduction

The Laboratory for Laser Energetics (LLE) at the University of Rochester conducts inertial confinement fusion (ICF) experiments with the sixty-beam OMEGA laser. Several of the diagnostics used in OMEGA both to measure the laser performance and in the target experiments are dependent upon the images acquired by CCD (Charged Couple Device) cameras. Therefore, controlling CCD cameras is vital to the success of the experiments at LLE.

Several versions of software for controlling CCD cameras have been developed by scientists at LLE in the past, all designed for use in the Microsoft Windows operating system. However, with an increasing interest in the Linux operating system at LLE, it was interesting to explore if software to operate CCD cameras could be created in the Linux environment. Since the Java programming language has several built-in features useful for software development, such as multi-threading, it was logical to write the software in that language.



Figure 1
CCD camera

Uses of CCD Cameras at LLE

CCD cameras are utilized in a variety of areas at LLE, including ultra-violet (UV) spectroscopy, X-ray diagnostics, and streak cameras. The images acquired by the cameras in use in the UV spectrometers capture the spectral lines of a laser beam. These spectral lines are then used to analyze the wavelength of the beam. In this manner, the different

wavelengths of the sixty beams in OMEGA can be analyzed.

The CCD cameras are also crucial when coupled with a streak tube and implemented as streak cameras in the generic streak camera platform. Light from a laser beam passes through the streak tube and is converted to a beam of electrons through the use of a photocathode. Any change in the intensity of the laser beam changes the intensity of the electron beam, so the electron beam is an accurate copy of the laser beam. This electron beam is then swept across a phosphor plate, causing it to glow. The changing intensities of the electron beam cause the glow to reflect the intensity variations of the laser beam. The CCD camera on the other side of this phosphor plate then photographs the glowing phosphor and, in effect, the intensity of light in the laser beam. Images from the camera can then be analyzed to measure the time history of the laser beam.

Program Function

The purpose of the CCDControl program is to provide an easy-to-use interface between the user and the CCD camera. The camera itself is connected to a device driver in the computer through a fiber-optic cable. The computer inside the camera recognizes certain letters as commands to perform a specified task. For example, sending the command "J" to the camera causes the camera to prepare itself to receive 32 configurations from the user's computer, and the command "L" causes the camera to send those configurations back to the user's computer. The CCDControl program automatically sends the specific commands to initialize the camera when it begins running, and other commands are sent during the course of the run as the user wishes.

The user, therefore, does not need to have any knowledge about which command to use to perform a task.

During the process of programming, several minimum values for the proper functioning of the camera were discovered. For example, the camera cannot safely process exposure times fewer than ten milliseconds (ms) for a timed image acquisition. Any exposure time less than ten ms may result in a failure to acquire the image, so an exposure time limit was encoded to ensure that the camera operates correctly at all times. In addition, monitoring the remaining exposure time, which is done by sending a command at regular intervals, cannot be done faster than every 50 ms and has to stop 200 ms before the end of the exposure. Smaller values may cause the camera to function incorrectly when acquiring the image.

User Interface

The GUI (Graphical User Interface) of the CCDControl program was based upon an earlier program written in Java that operates in Windows, with a few additions. It was meant to be as user-friendly as possible, with clear intentions of how it should be utilized. It provides important and

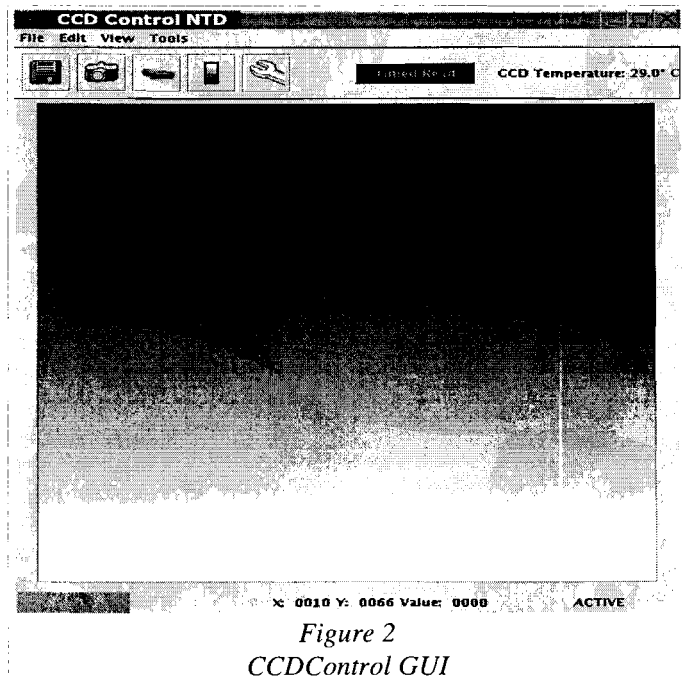
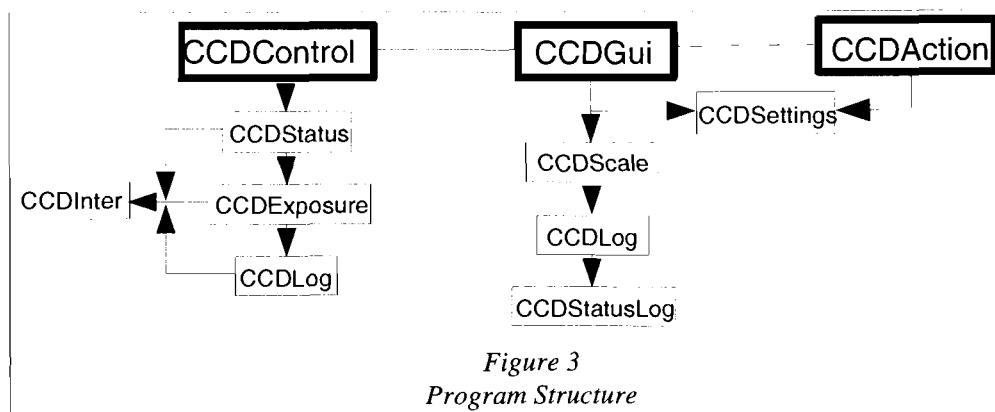


Figure 2
CCDControl GUI

real-time information regarding the status of the camera and each image acquisition, so the user knows exactly what the camera is doing. The temperature of the CCD is displayed in the GUI and automatically updated every second, and progress bars show the remaining exposure time and percent of the image read. The values of the 32 configurations and readout parameters are also displayed in a panel in the GUI to allow for easy user alteration. Any applied changes are then stored and used for subsequent initializations.

Program Structure

One advantage that the Java language brought to the program was the ability to create reusable code through the layering of the classes, allowing for easy future



modification. Since very little of the program is hardcoded, the classes are more versatile. The layered classes can easily be reused for other, similar applications without requiring major alterations in the code. The organization of the individual classes increases code readability and makes program comprehension much easier. Understandable code is crucial for a program which may undergo future modifications, and the layering provides for easy alteration of one class without drastically affecting the others around it.

The majority of the programs within CCDControl were written in Java; however, the methods of the interface that controls the camera needed to be written using the Java Native Interface and C because Java cannot interact directly with devices. There are several layers of software, beginning with the device driver which interacts directly with the camera, followed by the interface in C and Java, and then the CCDControl program.

Optimization

One of the key issues in designing this program was the efficiency at which the image could be acquired and displayed. Since the image is acquired in a grid of 2200 by 2200 pixels, and the typical size of a computer monitor is 1280 by 1024 pixels, it was clear that the image had to be reduced in size. It was determined that the image should be reduced in size to 550 by 550 pixels, or one-sixteenth of the original size, for test readings. This was done by a process called undersampling, displaying only every fourth pixel in every fourth row.

Several algorithms were tested to find the most efficient method of condensing the image, as it is often the case with CCD cameras that the image needs to be displayed very soon after the reading commences. The method that is used in the program takes

approximately six ms
per image, a
reasonably small
amount of time. The
original algorithm

<u>Algorithm A</u>	<u>Algorithm B</u>
<pre>int l, j=0, i=0; while (i<550*550) { l = i + 550; for (int k = i, k<l;k++) { image[k] = ImgArray[j]; j = j + 4; } i = i + 550; j = j + 2200 * 3; }</pre>	<pre>int k = 0; for (int i=0; i<2200*2200; i++) { if ((i/2200)%4 == 0 && i%4 == 0) { image[k] = ImgArray[i]; k++; } }</pre>

*Figure 4
Undersampling Algorithms*

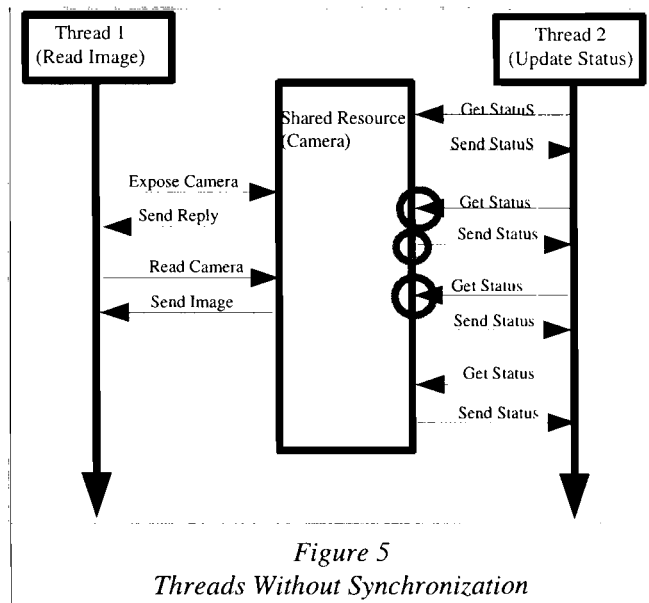
tested took about 166 ms per image, so the speed of the final algorithm was increased by a factor of 28. This remarkable increase is due to the number of operations performed. The first algorithm, algorithm “B” in the above table, has two divisions in each of 4840000 (2200 by 2200) iterations. Because division is a very time-consuming operation and there were so many divisions per run of the algorithm, the time required for the algorithm to complete its task was much greater than that of the final algorithm, algorithm “A.” The latter has two multiplication operations, which are less time-consuming than divisions, in each of 550 iterations and one addition and one multiplication in each of 302500 iterations. Not only does algorithm “A” avoid the use of divisions, it also has fewer loops to go through, which both contribute to the remarkable increase in efficiency. Thus, the user of the program significantly benefits from the optimization of the undersampling process.

Synchronizing Threads

Another issue examined in the development of this program was the synchronization of the threads that accessed the camera at different points in the program. Because the camera is a resource that many parts of the program have to share, it was necessary to synchronize the running of these threads so as to ensure that every thread could execute as planned and the camera wouldn't have any problems functioning as the user intended.

If the threads were not synchronized, several potential problems would arise. The CCD camera is a device that can only handle one task at once, whether that task be

reading the image, sending the status, or configuring itself to the users' specifications. If the camera is assigned one task, and then assigned another task without having first completed the first, serious problems can arise that range from sending back wrong data to freezing the system. In the diagram, potential problem spots are circled.



The first and third circles indicate points at which the camera has been given two commands, “Expose Camera” and “Get Status”, without having the chance to reply to the first command. These errors could result in incorrect data being sent back. The second circle illustrates two problems. One problem is that the camera has been commanded to send back two replies (Reply and Status) without first getting the command to acquire the status. The second problem is much more serious, as it affects the acquisition of the image. The camera has been designed so that the command to read the camera must be sent directly after the command to expose the camera. However, in the diagram, the camera has been directed to “Send Status” in between the “Send Reply” and “Read Camera.” This could easily result in the freezing of the system or other disruptive events.

Synchronization, however, prevents such errors from occurring by allowing only one set of commands to be sent to the CCD camera at one point. The synchronizing logic blocks all other threads from accessing the camera until the camera has finished. This

blocking is represented by the shaded oval. When the “Reserve Camera” command is sent, a shield of sorts is constructed, and the commands from the “Update Status” thread cannot get at the camera. Only after the camera has finished its task is the camera released and another set of commands may be sent by a different thread and

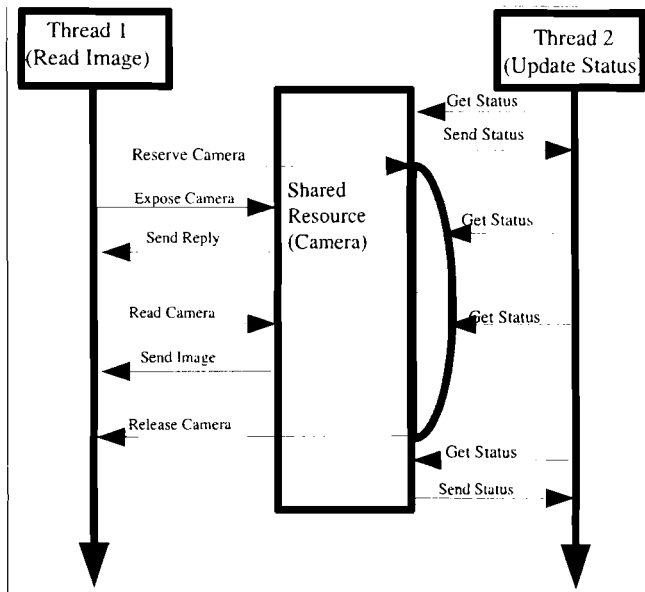


Figure 6
Threads With Synchronization

a new task performed. Thus, the “Update Status” thread resumes. This solves the problems posed by the first and third circles in the above diagram, and some additional logic solves the problem of exposing and reading in the second circle.

Advantages

The advantages of the CCD Control program include real-time status updates and increased flexibility in manipulating the acquisition of the image. The temperatures of the CCD and the backplate, as well as the vacuum chamber pressure, are newly acquired and displayed every second, and progress bars indicate remaining exposure time and acquisition time each time an image is acquired. These serve to keep the user informed as to the camera's current status.

Several methods were employed that increase the user's ability to manipulate the image acquisition. A panel was constructed that holds a few of the most used settings in

one place. This allows for easier modification of the settings, as the user does not need to know the number of the specific configuration or parameter that holds the value of the desired setting.

The scaling process was also updated to keep in place with new technologies in the CCD cameras. Older models of the camera sent image data back in 12-bit format, while the newer ones have changed to 16-bit. To accommodate this, the scaling was changed from 12-bit to 16-bit, the highest value (represented by white) changing from 4096 (2^{12}) to 65536 (2^{16}). Because of this rise in values, the process of selecting a value was made somewhat easier and more exact with the addition of text boxes where the user can input the desired scale values, instead of depending on the accuracy of the slider.

Conclusion

The successful development of a Linux-based program to control CCD cameras is of great assistance to diagnostic scientists at LLE. Scientists now have the ability to choose which operating system to use to control CCD cameras, which is of importance as Linux use increases. The CCD Control program allows users with little knowledge of the individual commands sent to the camera to interact with the CCD camera efficiently and effectively. The program has been tested in the Generic Streak Camera Platform (GSCP) and will undergo further improvements in the future before its implementation.

Acknowledgments

First and foremost, I would like to extend my greatest thanks to Dr. Christian Stoeckl for advising me on this project. Without a doubt, it is due to his expertise and guidance, as well as his remarkable patience and dedication, that this was completed. I would also like to thank Dr. R. Stephen Craxton for giving me the opportunity to participate in this program.

Characterization of the OMEGA Sixty-Channel UV Spectrometer

Ryan Blair

Characterization of the OMEGA Sixty-Channel UV Spectrometer

Ryan Blair

*Laboratory for Laser Energetics, University of Rochester
Rochester, New York 14623-1299*

Abstract

A UV spectrometer has been built for installation on OMEGA to analyze the UV wavelength spectrum of the laser system. Before implementing the spectrometer on OMEGA, the spectral resolution was determined. After the optics of the spectrometer were assembled, aligned, and focused, a neon spectral lamp was used to verify that the spectral dispersion and imaging quality of the system agreed with theoretical values. The experimentally determined resolution of 3.5 pm compares well to the theoretical value of 3.2 pm. The performance was evaluated for installation requirements on OMEGA.

Introduction

At the Laboratory for Laser Energetics, the OMEGA laser system has continued to support the National Inertial Confinement Fusion (ICF) program. In supporting this program, implosion experiments and basic physics experiments are conducted to further research related to high-energy-density phenomena. A major goal of ICF is to develop what will one day become a vast source of power in the future, fusion-based energy production. Currently fusion energy output is only one percent of the input energy, but through the efforts at the LLE, Lawrence Livermore, and other laboratories it is a possible future energy source.

The OMEGA system delivers pulses of laser energy to targets in order to measure the resulting nuclear and fluid dynamics.¹ The system, which is approximately ten meters high and one hundred meters long, is capable of delivering 30kJ of energy on a target of less than one millimeter in diameter in approximately 1 billionth of a second. At the front end of OMEGA, a seed laser pulse from an infrared (IR) laser enters and then propagates through the system where it is amplified, shaped, split into sixty beams, frequency converted into green, frequency converted again into ultraviolet (UV) and then pointed and focused onto the target. These beams are analyzed after conversion into UV by a spectrometer to better understand important processes of the OMEGA system. In measuring these spectra the spectrometer will assist in observing frequency conversion crystal tuning, detecting pinhole clipping, observing B-integral effects, and detecting noise entering the Pulse Generation Room.

Background

Spectrometers use spectral dispersion to produce and observe the spectrum of a light source. Dispersion can occur by two methods: refraction and diffraction. In the case of refraction, light enters a medium and exits according to Snell's Law

$$n_1 \sin \theta_1 = n_2 \sin \theta_2 \quad (1)$$

where n_1 and n_2 are the indices of refraction of two adjacent media, θ_1 is the incident angle, and θ_2 is the exiting angle. Because different wavelengths of light travel through different media at different speeds, their refraction angles differ and dispersion occurs.

The other method of dispersion, diffraction, is much more useful for building spectrometers for several reasons. The fundamental grating equation

$$\sin \alpha + \sin \beta = 10^{-6} kn\lambda \quad (2)$$

dictates how light travels when it hits a grating where α is the incident angle, β is the angle of diffraction, k is the diffraction order integer, n is the groove density (grooves/mm) and λ is the wavelength in nm.² According to this equation, it can be shown that diffraction can produce a much larger dispersion as compared to using a refractive medium for dispersion within the same space constraints.

Diffraction gratings are the source of dispersion in spectrometers and allow for resolving spectral lines of angstrom differences. The OMEGA UV Spectrometer was built to analyze the sixty beams produced from the propagation of the initial beam in the OMEGA system. After passing through frequency conversion crystals the sixty beams all have spectral features of interest within Angstroms of each other so a large dispersion is needed to resolve them. It is because of this high resolving power required that diffraction gratings are important as they produce the high dispersion necessary. The spectrometer shown in Figure 1.1 contains three Jobin Yvon 3600 grooves/mm aluminum coated diffraction gratings to meet the required resolution specifications.

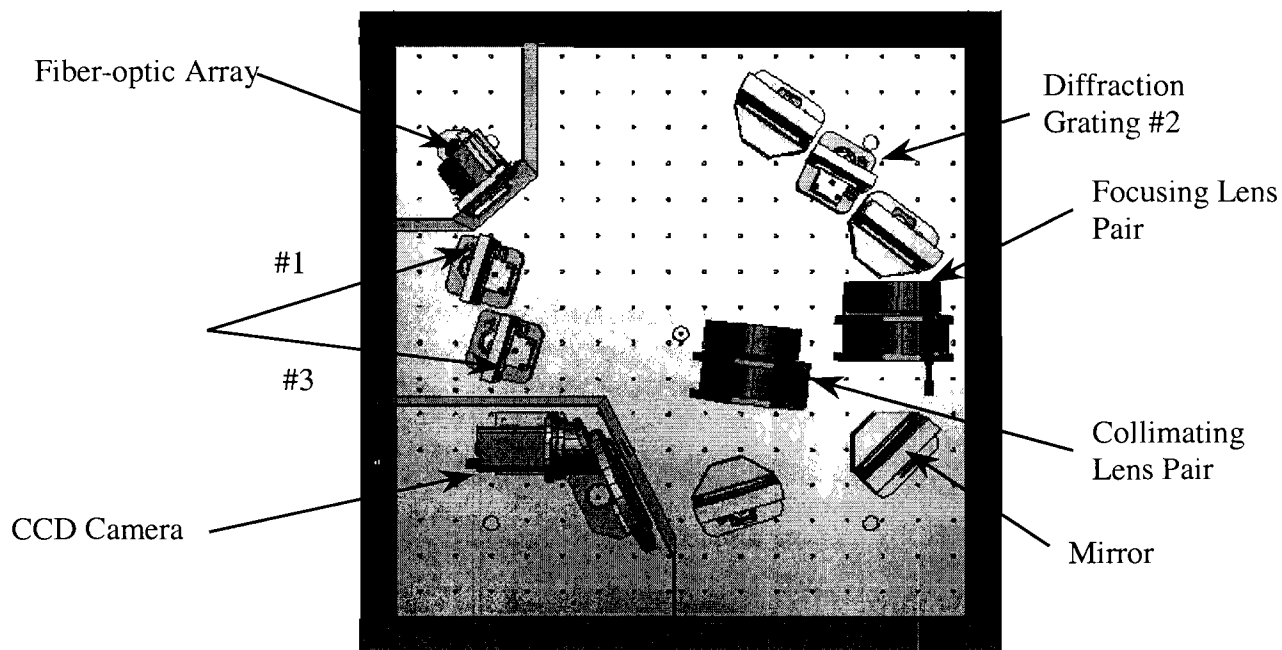


Figure 1.1. An overhead view of the UV spectrometer. Contained in the spectrometer are three Jobin Yvon diffraction gratings, four UV high-reflection coated fused silica mirrors, a collimating lens pair, a focusing lens pair, a fiber-optic cable housing where light enters the system and the CCD camera that records the image of the slit of the fiber-optic cable.

Experiment

The spectrometer is housed on a 4 ft x 4 ft lightweight breadboard. Four aluminum black anodized panels serve as the sides of the spectrometer and a 4 ft x 4 ft Plexiglas cover cut into four removable pieces composes the cover. The spectrometer is composed of three Jobin Yvon 3600 lines/mm holographic reflection gratings, UV anti-reflection coated fused silica lenses and windows, UV high-reflection coated fused silica mirrors, and a Spectral Instruments Series 800 Camera with a 2k x 2k 13.5 μm pixel Marconi CCD chip. Two shrouds were manufactured to house the fiber-optic cable input and the CCD camera respectively.

A one-to-one blueprint of the positions of the mounts was created and laid on the breadboard and then the mounts were installed on the breadboard with positions and angles relative to each other as dictated by the one-to-one tracing. To ensure the optics were properly aligned a 351-nm wavelength, 300-ps pulse width, 0.5-mJ 10-Hz rep rate laser was propagated through the system. At each interface a fluorescent card was used to determine the position of the beam and the orientation of the optics. After fine-tuning and adjustments were made the optics directed the beam path to the next optical interface. This was repeated for all mirrors, lenses, and gratings until the beam arrived at the CCD camera. The reason for this alignment was to ensure that the orientation of all optics was correct and the beam would propagate through the system correctly before the beam was focused.

In order to focus the beam the two lenses, the focusing lens and the collimating lens were adjusted until the width of the image recorded on the CCD camera was minimized. The lamp used for focusing was an Oriel Neon pencil-style spectral calibration lamp with an Oriel 6045 power supply. This lamp also provided multiple spectral lines around 351 nm that allowed for the calculation of the spectral dispersion. This setup also gave an estimation of the width of wavelengths the spectrometer could analyze. The beam path can be seen below in Figure 1.2.

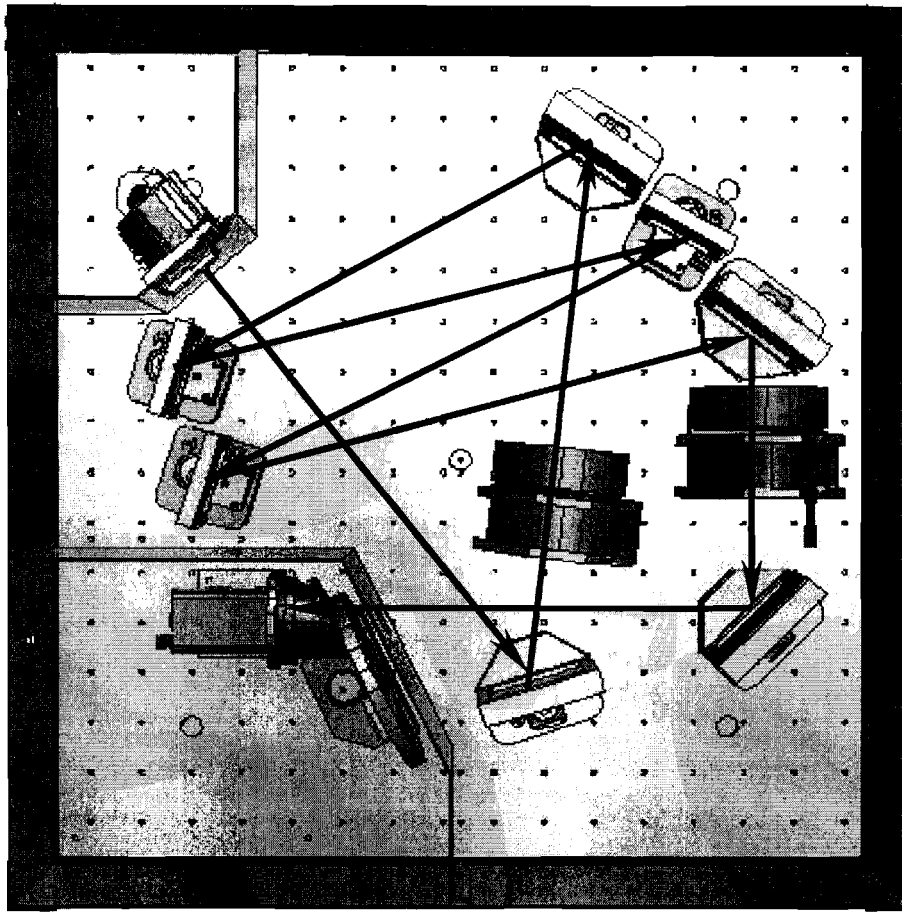


Figure 1.2. The beam propagates from the top left at the fiber optic cable to the bottom left at the CCD camera. The beam path is shown with black arrows.

Results

A neon spectral lamp was used to determine the imaging ability and spectral dispersion of the spectrometer. A Polymicro 300- μm core UV optical fiber with a 40- μm slit was used as the input of the neon source light into the spectrometer. The image of the slit on the CCD camera (figure 1.3) was found to be 40 μm at full width half max (FWHM). This is very close to the predicted image width of 35 μm (due to demagnification of the optical system). A possible explanation for the small discrepancy between the experimental and predicted values is that the optical system was not perfectly focused.

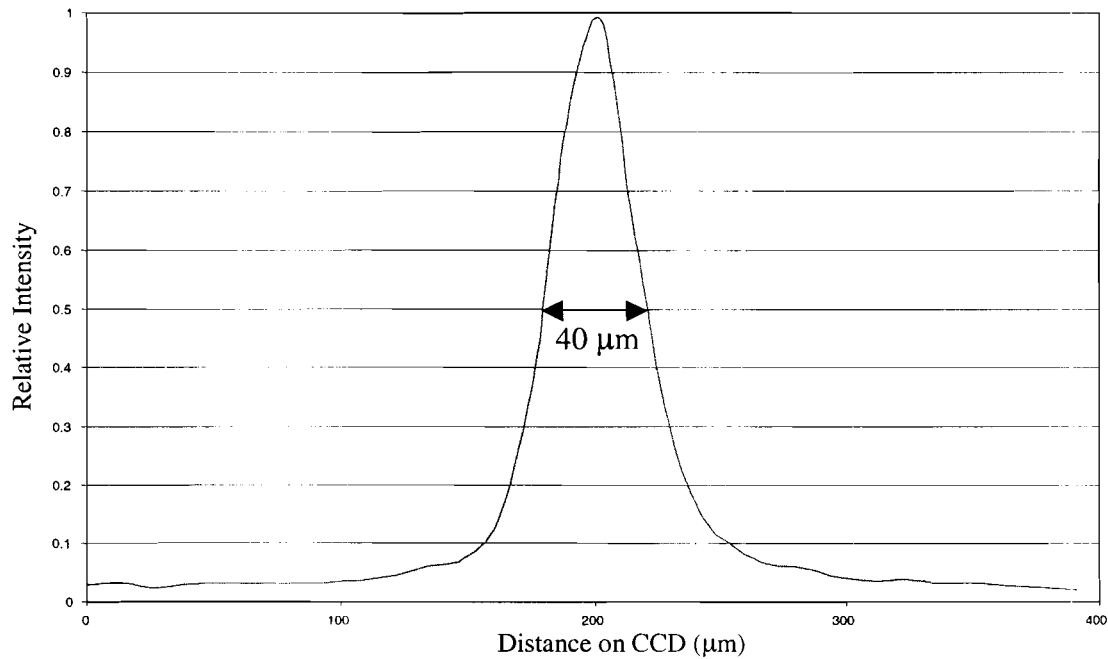


Figure 1.3 Image on the CCD resulting from a single spectrum line input to the spectrometer through a 40- μm slit.

To determine the spectral dispersion, defined as the change in CCD position divided by the change in wavelength, five known Neon I spectral lines were compared to the CCD spectrum data. As seen on the accompanying figures 1.4 and 1.5 the CCD data matches the relative positions of five known Neon I spectral lines. The spectral dispersion was calculated from this data to be 11.6 $\mu\text{m}/\text{pm}$.

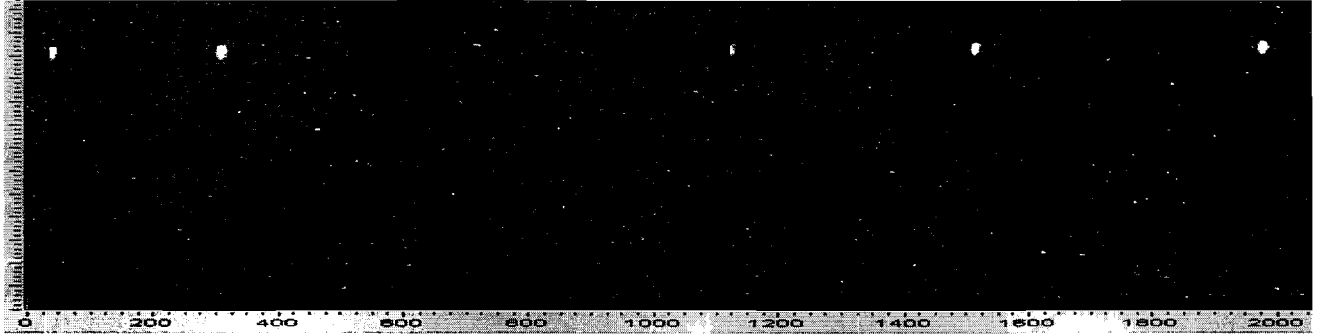


Figure 1.4 CCD Image, 2048 pixels wide (1 pixel = 13.5 μm)

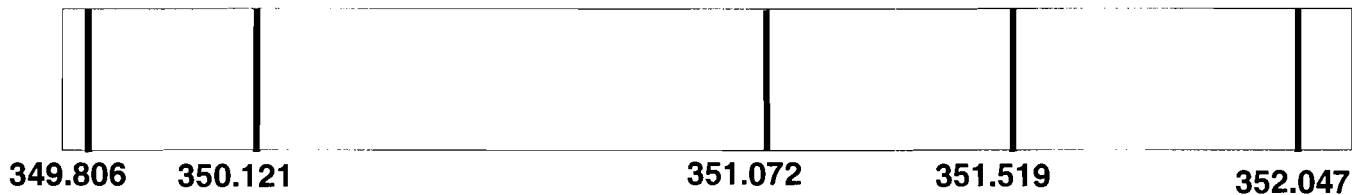


Figure 1.5 Neon I spectral lines from MIT wavelength table (nm)

Using a basic relational definition of resolution³,

$$R \sim \frac{\text{FWHM Image of Entrance Slit}}{\text{Spectral Dispersion}} \quad (3)$$

valid when the image size is much larger than the pixel size of the detector, the experimental resolution was calculated to be 3.5 pm.

To compare the experimental results to theory, OSLO, a ray-tracing program, was used to calculate expected values. OSLO predicted an approximately 11 $\mu\text{m}/\text{pm}$ spectral dispersion, a 35- μm wide image, and a resolution of 3.2 pm using a 40- μm slit. These results show the new spectrometer has a resolution that is almost two times better than that of the previous spectrometer (6 pm) and that the alignment of the optics in the spectrometer is nearly optimized.

Summary

With the spectrometer nearly optimized, installation on the OMEGA system can soon occur. The UV spectrometer will assist in monitoring frequency conversion crystal tuning, detecting pinhole clipping, detecting excessive B-integral in the amplifiers, and detecting noise entering the Pulse Generation Room. With a resolution approximately two times better than that of the UV spectrometer currently used on OMEGA, and the capability of analyzing all sixty beams of the OMEGA system simultaneously, the UV spectrometer will provide new insight into the workings of the OMEGA system.

References

1. R.L. McCrory et al., *OMEGA System Operations Manual - Volume I -- System Description*, Laboratory for Laser Energetics, 2002.
2. J.M. Lerner and A. Thevenon, "Section 1: Diffraction Gratings Ruled & Holographic," *Spectrometer and Monochromator Discussion – A Tutorial*, Jobin Yvon Web Site. http://www.jobinyvon.com/jy/oos/oos_ch1.htm.
3. J.M. Lerner and A. Thevenon, "Section 2: Monochromators and Spectrographs," *Spectrometer and Monochromator Discussion – A Tutorial*, Jobin Yvon Web Site. http://www.jobinyvon.com/jy/oos/oos_ch2.htm.

Pulse-Shaping Effects in Optical Parametric Amplifications

George Dahl

Pulse Shaping Effects in Optical Parametric Amplifications

George E. Dahl

Allendale Columbia School

Rochester New York

Pulse Shaping Effects in Optical Parametric Amplifications

Abstract:

An optical parametric amplifier (OPA) can provide laser amplification over a much larger spectral bandwidth than current amplifiers used in the OMEGA laser system. The OMEGA laser system is located at the University of Rochester Laboratory for Laser Energetics (LLE) which is where the work for this project was performed. Wider spectral bandwidth is advantageous for laser pulse smoothing techniques such as smoothing by spectral dispersion (SSD)¹. An OPA could replace an OMEGA regenerative amplifier and possibly a Large Aperture Ring Amplifier (LARA), both of which are used in the “front end” of the OMEGA laser system, if its output pulse shape and stability were suitable for injection into the main OMEGA laser chain. In the optical parametric amplification process, a “pump” laser pulse transfers its energy to a “seed” laser pulse through a nonlinear interaction in a crystalline material. A numerical computer model was used to determine the input pulse shapes required to obtain a specific desired output pulse shape (the shape that after going through the main OMEGA laser chain would produce the “alpha308” shape). A two-crystal system that can create the desired output pulse shape is presented. To the best of my knowledge, this is the first time an OPA has been shown to be able to produce the highly shaped pulses necessary for Inertial Confinement Fusion lasers. A tradeoff between output pulse stability and input pulse contrast ratio is described.

I. Introduction

Inertial Confinement Fusion (ICF) could be a clean and essentially unlimited energy source. The fuel is made of deuterium and tritium, which are both readily available, and the main

byproduct of ICF is helium, an inert gas. Deuterium naturally occurs in water, and tritium can be produced from lithium in a reaction induced by the fusion process.² Inertial Confinement Fusion can be achieved by using a high intensity laser pulse to uniformly illuminate a spherical target composed of deuterium and tritium fuel. The illumination causes ablation of the spherical target shell, which in turn produces an equal and opposite reactive force that implodes the fuel at the center of the target.

An optical parametric amplifier is being considered as a possible replacement for the regenerative amplifier and the large aperture ring amplifier (LARA) in the front end of the OMEGA laser system at the University of Rochester Laboratory for Laser Energetics (LLE), one of the major laboratories studying inertial confinement fusion. The National Ignition Facility at Lawrence Livermore National Laboratory might also directly benefit from greater understanding of the pulse shaping capabilities of an OPA.

The primary advantage of the replacement would be that an OPA can provide broadband amplification, whereas the current system only amplifies a narrow spectral bandwidth. Greater bandwidth would allow the bulk phase modulators currently in use to be replaced with integrated phase modulators. Integrated phase modulators simplify and add flexibility to smoothing by spectral dispersion (SSD)¹ bandwidth generation. Another key advantage of integrated phase modulators is that they can be commercially purchased and do not need to be specially built at LLE or another research facility. Using an OPA would also result in a reduction in the number of optical surfaces used, thus reducing the complexity and improving the reliability of the SSD system.

In order to replace the regenerative amplifier and large aperture ring amplifier with an OPA, the OPA must be able to produce the pulse shape required by the main OMEGA laser

chain. The main OMEGA laser chain requires a specific input pulse shape that, after emerging from the chain, will be what is known as the alpha308 shape. The pulse shape required as input to the OMEGA laser chain in order to produce the alpha308 pulse shape will hereafter be referred to as the pre-compensated alpha308 pulse shape (the pre-compensated alpha308 pulse shape is shown as the dashed line in Fig. 6). A computer simulation was used to determine the input pulse shapes to an OPA that are necessary to produce the pre-compensated alpha308 pulse shape at the output of the OPA. The computer model used a two-crystal OPA design³ that is currently implemented as a prototype laser system at LLE.

Using an OPA for front end amplification in OMEGA also requires that the output pulse of the OPA remains stable against input pulse intensity fluctuations. After the input shapes required to produce the pre-compensated alpha308 pulse shape were determined, the output stability was calculated and examined. When possible, changes were made to the input pulse shapes to improve output stability while still producing the pre-compensated alpha308 pulse shape. The methodology used to determine the input pulse shapes and to improve output intensity stability is quite general, and can be used for any OPA output pulse shape.

II. Introduction to OPA

The optical parametric amplifier used in all simulations consisted of two lithium triborate (LBO) crystals. The dimensions of the crystals were 5 mm x 5 mm x 29.75 mm with the largest dimension equal to the length of the crystal in the propagation direction of the laser beam. A seed beam was amplified by a pump beam through a nonlinear interaction in the crystalline material. In the OPA process, a third beam, called the idler, is generated as a result of the nonlinear mixing of the pump and seed waves. A type 1 process was simulated, where the pump

was an extraordinary wave (e-wave) and the signal (i.e. amplified seed) and idler were both ordinary waves (o-waves). The model³ simulated the propagation of the input pump and seed beams through the two crystals and produced a depleted pump beam, an amplified signal beam, and an idler beam that was ignored. Spatially, the pump was a 10th-order super Gaussian with a full width at half maximum (FWHM) of 3.5 mm and the seed was a Gaussian with a FWHM of 3.18 mm.

III. Methodology

For each temporal point in an input pulse there is a corresponding local intensity value. Each combination of a pump and a seed local intensity produces a single local output intensity. Output intensity is a function of input seed intensity and input pump intensity. A look-up table of pump and seed input intensity combinations and corresponding output intensities was constructed. To find the input needed for an arbitrary temporal shape, the following steps were performed:

1. The look-up table was filled with input and output intensity data that was calculated using a computer simulation³ of the two-crystal OPA in section II. Flat-topped seed pulses of different total energies and a single linearly-ramped pump were used as input in order to systematically calculate many possible combinations of input intensities.
2. Output stability was calculated at each temporal point in the output pulse shape and added to the look-up table.
3. The look-up table was used to specify the input pulse shapes required to obtain the pre-compensated alpha308 pulse shape. The computer simulation was used to verify

that the predicted input shapes actually produced the required output and to further optimize the pulse shape design and stability.

1. Simulation of an OPA with linearly-ramped pump and flat-top seed pulses

The simulation program was run many times with the same input pump and with seeds of different total energies. As shown in Fig. 1, the pump was a simple linear ramp. As shown in Fig. 2, the seeds were all flat. The only difference between successive runs in this stage of the simulation process was the energy of the seed. The local output intensities for all of the runs were recorded in the look-up table. Each run filled up one row of the table. Figure 3 shows typical corresponding output.

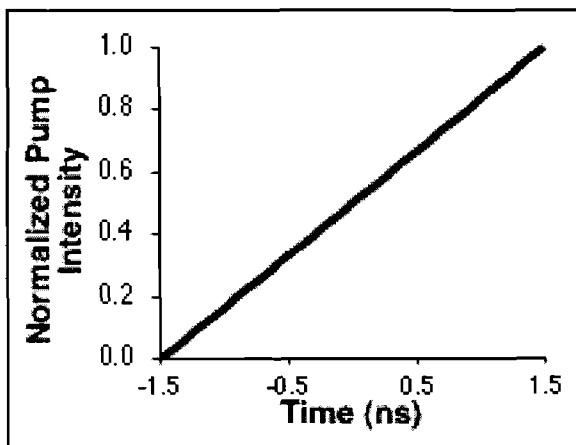


Figure 1: Plot of the normalized temporal pump shape used to gather output data. This pump shape was used in all the flat-top seed runs.

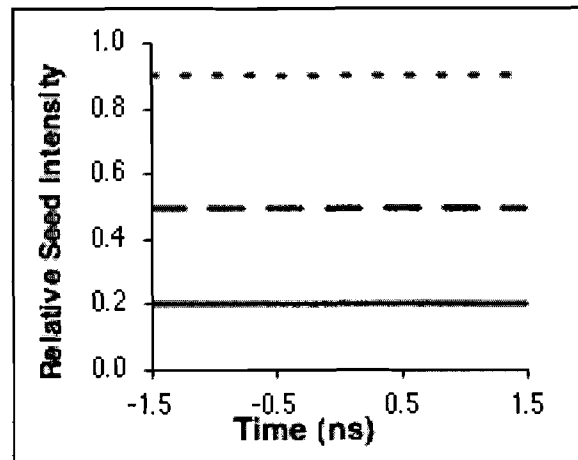


Figure 2: Plot of temporally flat seed pulses of different relative energies used with the ramped pulse of Fig. 1

At the foot of the output pulse in Fig. 3, the signal experienced exponential gain. At the

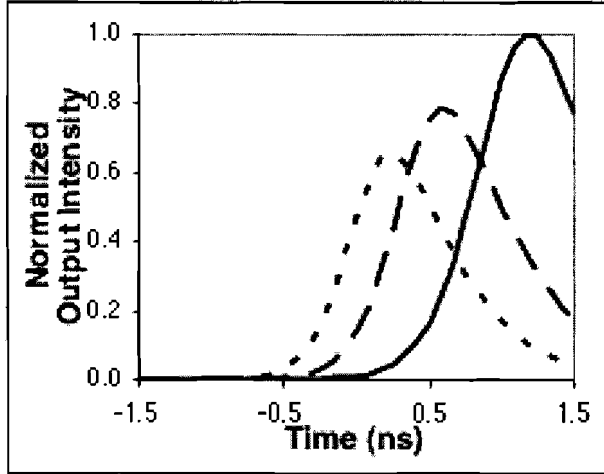


Figure 3: The output temporal pulse shape produced by the three sample seeds in Fig. 2 when combined with the pump shape shown in Fig. 1. The plot shows that as the seed energy is increased, peak saturation occurs at earlier times and at lower relative intensity values. Relative seed energies: 0.2 – solid, 0.5 – dashed, 0.9 – dotted.

peak of the output pulse (i.e., the peak saturation point), the pump beam was depleted and had no more energy to transfer to the signal. The peak saturation point marks the beginning of the reconversion regime where the signal begins to amplify the pump. The effect of increasing the seed energy is to change the point where reconversion begins. Increasing the seed energy moves the saturation point

backward temporally and decreases the intensity of the peak of the output.

2. Calculation of output intensity stability

Relative stability is defined as:

$$\left(\frac{\Delta I_{\text{signal}}}{I_{\text{signal}}} \right) / \left(\frac{\Delta I_{\text{pump}}}{I_{\text{pump}}} \right) \quad (1)$$

Where $(\Delta I_{\text{signal}} / I_{\text{signal}})$ is the relative change in output intensity and $(\Delta I_{\text{pump}} / I_{\text{pump}})$ is the relative change in input pump intensity. The relative stability factor is a measure of the effect input pump intensity fluctuations have on output intensity. The closer the relative stability factor is to zero, the less the output intensity is affected by fluctuations in pump intensity. To find the relative stability factor for all the temporal points in a given run, the simulation was repeated with a +1% and a -1% total pump energy variation. At each temporal point, the difference in

output signal intensity between the +1% pump energy run and the - 1% pump energy run was divided by the output intensity of the original run. That quantity was then divided by the relative change in pump energy (2%) to obtain the relative stability value. The relative stability factor was calculated for each temporal point in each run of the simulation and recorded with the corresponding output intensity in the look-up table. Sample relative stability curves appear in Fig. 4. Note from Figs. 3 and 4 that relative stability is best at the peak of the pulse and reduced at the foot of the pulse. The most stable region of the pulse is where the signal is saturated and reconversion begins.^{3,4} For a temporally flat seed, and a linearly ramped pump, there is a unique pump local intensity value that produces the most stable output, and this point corresponds to the start of reconversion. The zeros of the stability curves in Fig. 4 are the points of maximum stability and they correspond to the peaks of the output curves in Fig. 3.

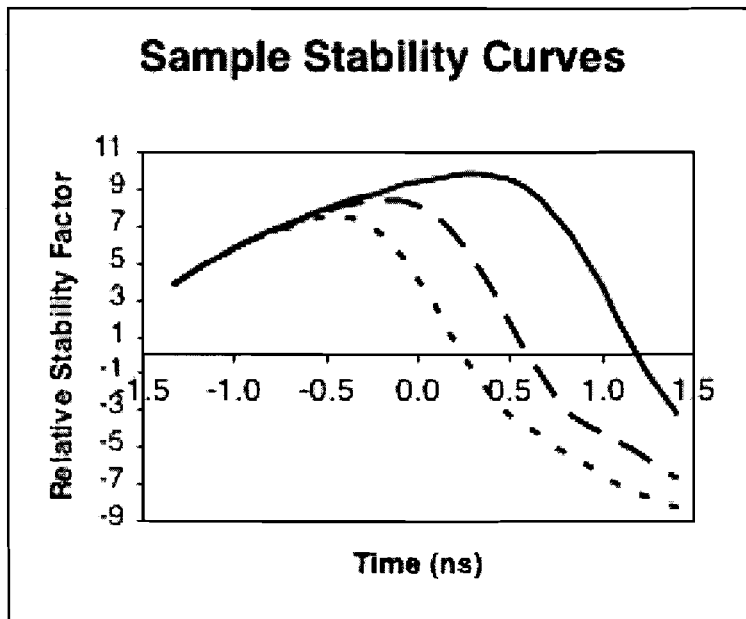


Figure 4: Plot of Eq. (1) vs. time. Since peak output intensity moves backward temporally as seed energy increases, the point of best stability (relative stability factor=0) does also. Relative seed energies: 0.2 – solid, 0.5 – dashed, 0.9 – dotted.

3. Design of input pulse shapes

The input and output intensity and relative stability data were collected into a look-up table so that input intensity values could be chosen to make the pre-compensated alpha308 pulse shape. Looking up a desired output intensity in the table gives input pump and seed intensities that will produce the desired value. Each combination of input pump and seed intensities also gives an estimate of what the relative stability will be. Although there is only one output value and relative stability for any given combination of input pump and seed values, there are many combinations of input pump and seed values that produce a given output value. This fact provides flexibility in choosing input intensity values to make an arbitrary output pulse shape. Since there are many combinations of input pump and seed values that will produce the same local output intensity value, additional criteria for either input or output pulses can be imposed. Points can be chosen to produce input pulse shapes that are smoother or have lower contrast ratios. Contrast ratio (CR) is defined as the ratio of the largest local intensity value in the pulse to the smallest local intensity value in the pulse. Avoiding discontinuities in the input shapes was a high priority in choosing points. Points were chosen to make relatively smooth curves while curves with many relative maxima or minima were avoided. Flexibility in choosing points for the input shapes makes it possible to create the pre-compensated alpha308 pulse shape with better relative stability than if such flexibility were not present.

IV. Results

The first successful attempt to specify input shapes that produced an output shape close to the pre-compensated alpha308 pulse shape was performed with a flat seed and the pump shape shown in Fig. 5 (below). The total energy of the flat seed pulse was 100 pJ. The total energy of

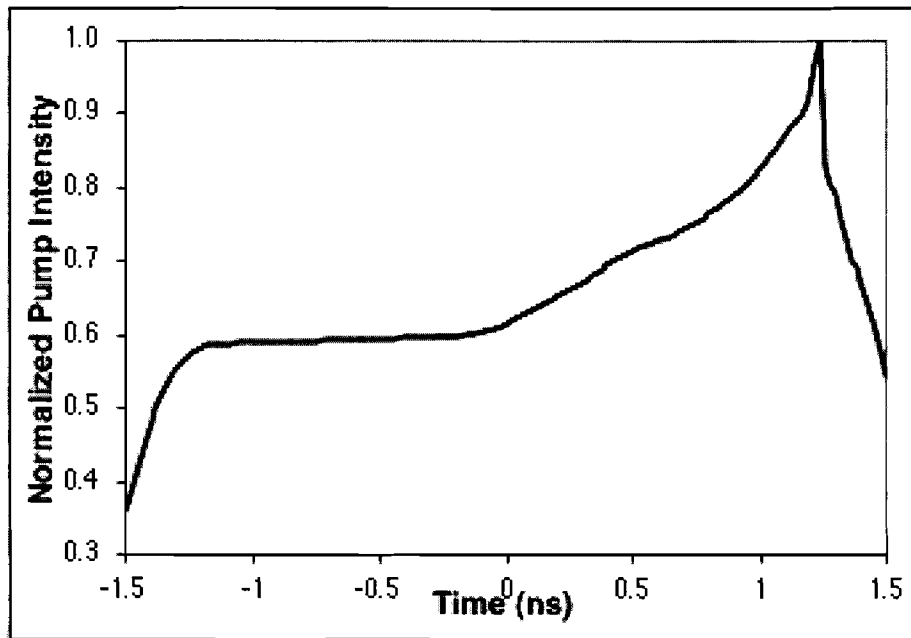


Figure 5: Plot of the normalized temporal pump shape that, when combined with a 100 pJ flat-top seed produced the pre-compensated alpha308 pulse shape.

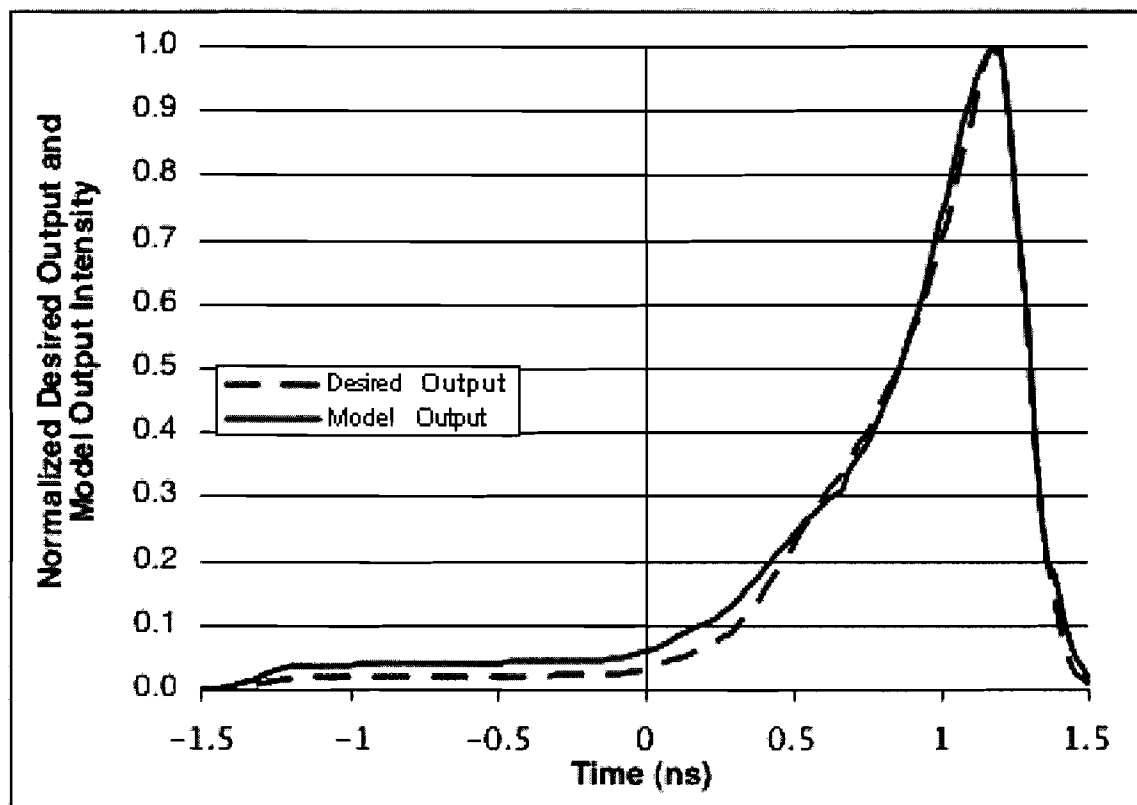


Figure 6: Plot of normalized temporal shapes for the desired output and the output produced by Fig. 5 and a 100 pJ flat-top seed.

the pump pulse was 0.250 J. The output shape produced by the input pump shape in Fig. 5 and a 100 pJ flat-top seed closely matched the pre-compensated alpha308 shape. Figure 6 shows the model output and desired output. The area of the pulse where the most noticeable discrepancy between the desired output and the model output shape occurs is at the foot of the pulse close to 1.5 ns into the pulse. A better fit of model output to desired output could have been achieved, but was not deemed worthwhile because of poor relative stability. The output stability at the foot of the pulse in this case was about 10 times that of the pump stability. Although it is useful to know that the output shape can be produced using a flat seed, the stability of such a shape is very poor at the foot of the pulse due to little saturation in this region.

Using a more extensively shaped seed offers an improvement in stability over using a flat seed. Highly shaped seed and pump temporal profiles that produced the pre-compensated alpha308 pulse shape are shown in Figures 7 and 8. The output produced by these input shapes is a better fit to the desired output than the output of the flat seed attempt because more time was spent making small adjustments to the input shapes. The output is shown as the grayed line in

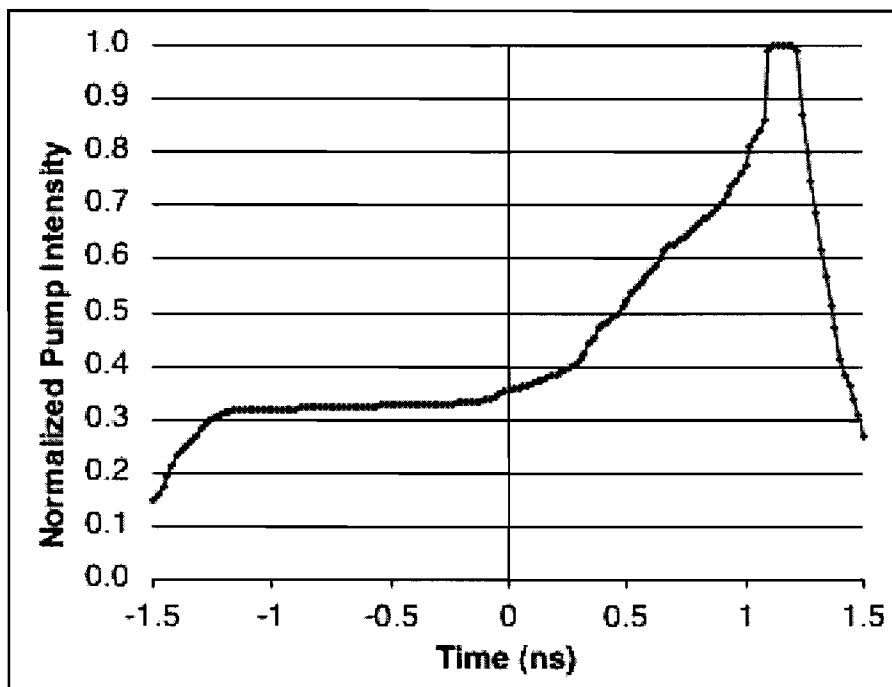


Fig. 9.

Figure 7: Plot of the normalized temporal pump shape that, when combined with the seed in Fig. 8, produced the pre-compensated alpha308 pulse shape.

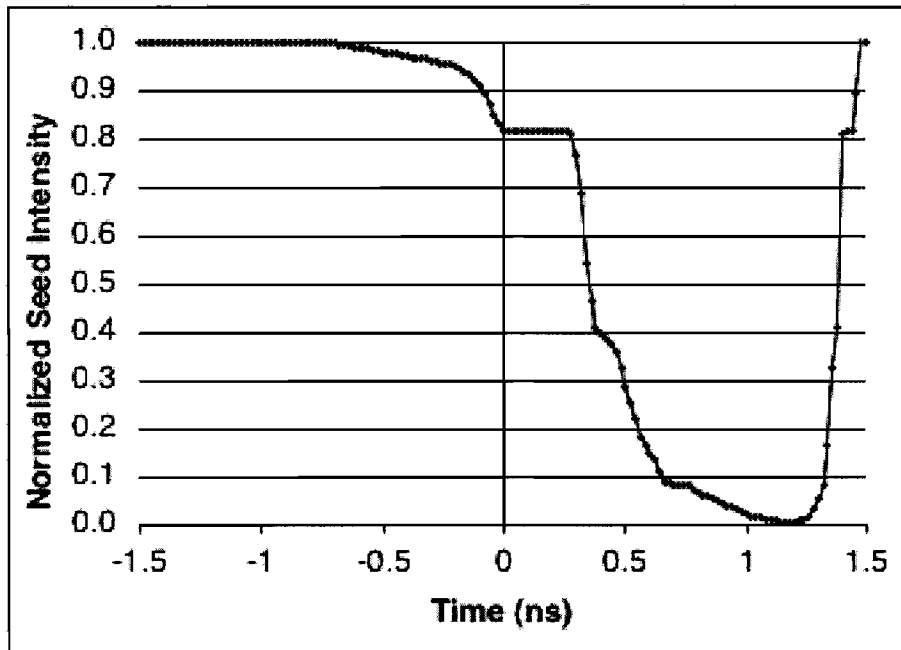


Figure 8: Plot of the normalized temporal seed shape that, when amplified by the pump in Fig. 7, produced the pre-compensated alpha308 pulse shape.

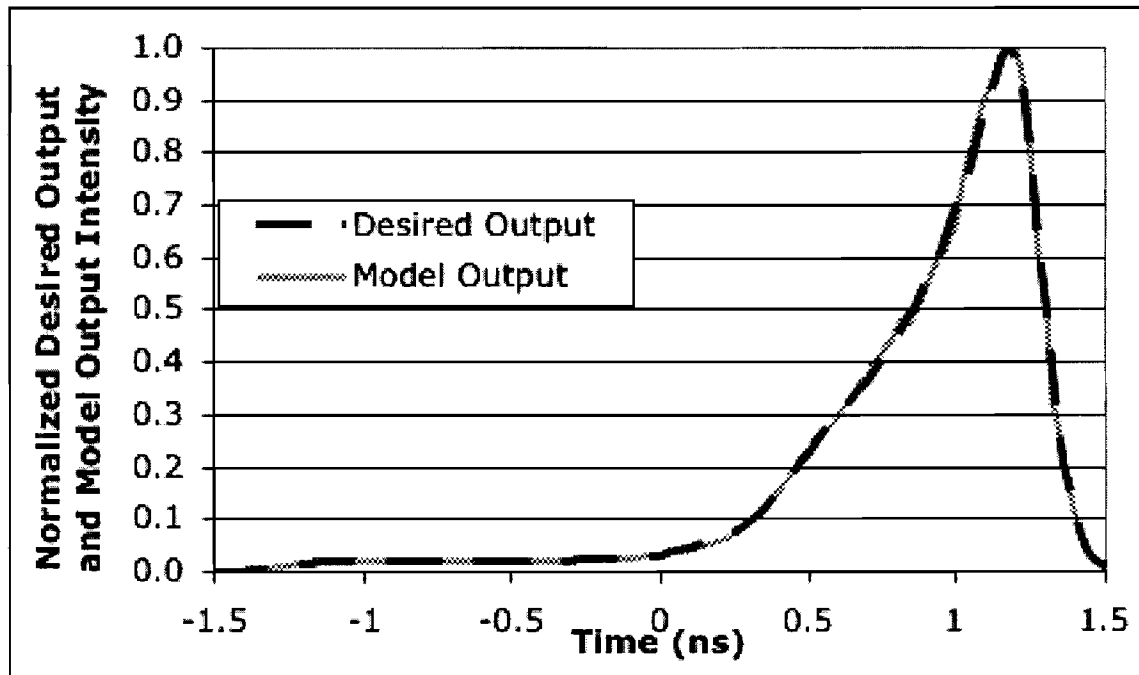


Figure 9: Plot of the temporal pulse shapes of the model output and the desired output. The model output was produced by the non-flat seed in Fig. 8 and the shaped pump in Fig. 7.

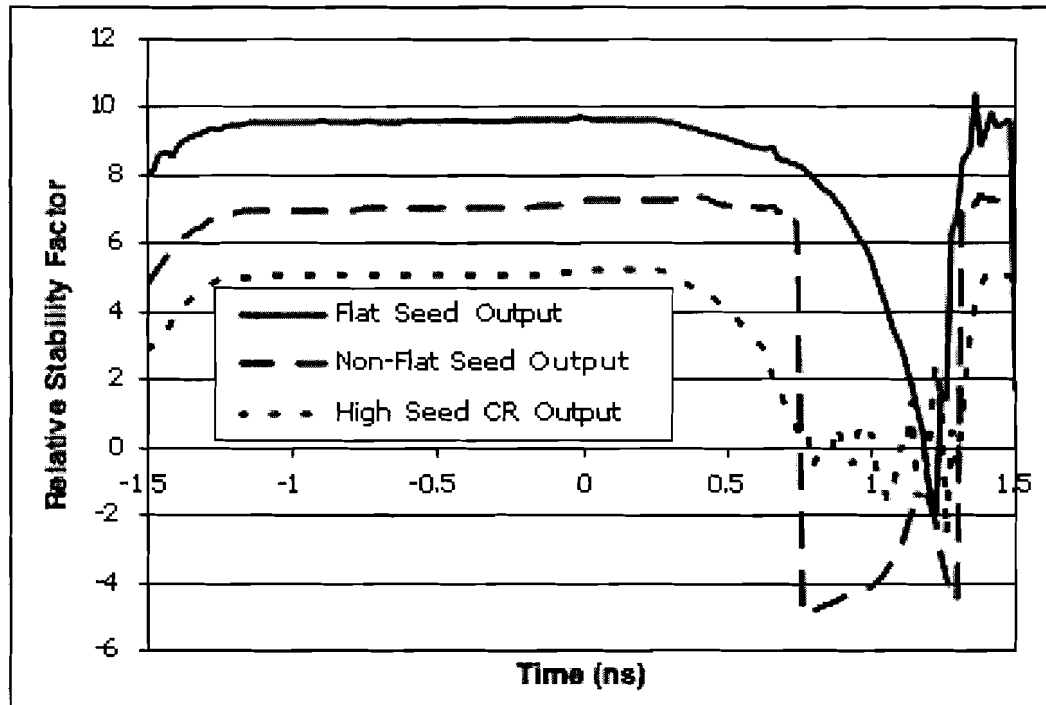


Figure 10: Relative stability factor vs. time for three different pulse shape combinations. The solid line is a plot of the relative stability factor of the output produced by a 100 pJ flat-top seed and the pump shape shown in Fig. 5. The dashed line is a plot of the relative stability factor of the output produced by the seed in Fig. 8 and the pump in Fig. 7. The fine dashed line is a plot of the relative stability factor of the output produced by the high contrast ratio pump in Fig. 11 and the high contrast ratio seed in Fig. 12.

The relative stability of the output produced by the pump shape in Fig. 7 and the non-flat seed shape in Fig. 8 was better than the relative stability of the output produced by a 100 pJ flat-top seed and the pump from Fig. 5. The relative stability factors for both attempts are plotted in Fig. 10. The stability near the peak of the output pulse (1.2 ns) is very good in both output pulses. There is a significant improvement in stability at the foot of the output pulse between the output produced by the 100 pJ flat-top seed and the non-flat seed. In order to get maximally stable output at the foot of the pulse (i.e. stability like that at the peak), only local input intensity values that produce a local output intensity value very close to saturation can be used. As previously discussed, increasing the seed local intensity means that a smaller pump local intensity is required for saturation and reversion to occur and that the signal intensity at the point of greatest stability is reduced. Although it is possible to use only highly stable points

(points near saturation) to make the input shapes that produce the pre-compensated alpha308 shape, an extremely large range of local seed intensities would be required to obtain a sufficiently large range of output intensities.

A large range of seed local intensities requires that the input seed pulse have a large contrast ratio. Input pulses with high contrast ratios are more difficult to produce than input pulses with lower contrast ratios. The pre-compensated alpha308 shape has a contrast ratio of about 50:1. The pump that together with a flat 100 pJ seed was able to produce the pre-compensated alpha308 shape had a contrast ratio of 2.8:1. The more highly shaped pump and seed pulses of Figs. 7 and 8 had higher contrast ratios of 7:1 and 146:1, respectively.

Additional runs were performed in order to improve the output stability beyond that shown in Fig. 10 by further increasing the contrast ratios of the input pulses. It was necessary to do additional runs of flat-top seeds and a linearly ramped pump in order to generate more data for the look-up table. The flat-top seeds had significantly higher total energies than when the same procedure was performed earlier (see Methodology: Section 1). The seed and pump input shapes that produced a highly stable pre-compensated alpha308 pulse shape in this case had significantly higher contrast ratios of 5760:1 and 17:1 respectively. The higher contrast ratio pump shape is shown in Fig. 11 juxtaposed with the pump used previously (Fig. 7). Figure 12 shows the higher contrast ratio seed shape along with the seed from Fig. 8.

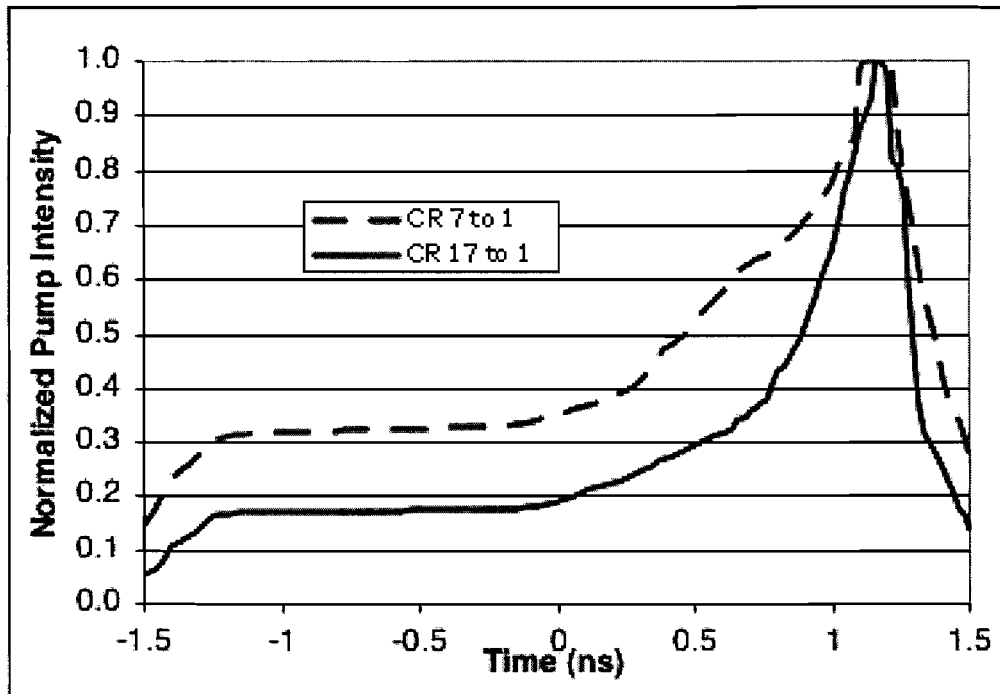


Figure 11: Plot of the higher contrast ratio pump shape and the pump shape from Fig. 7.

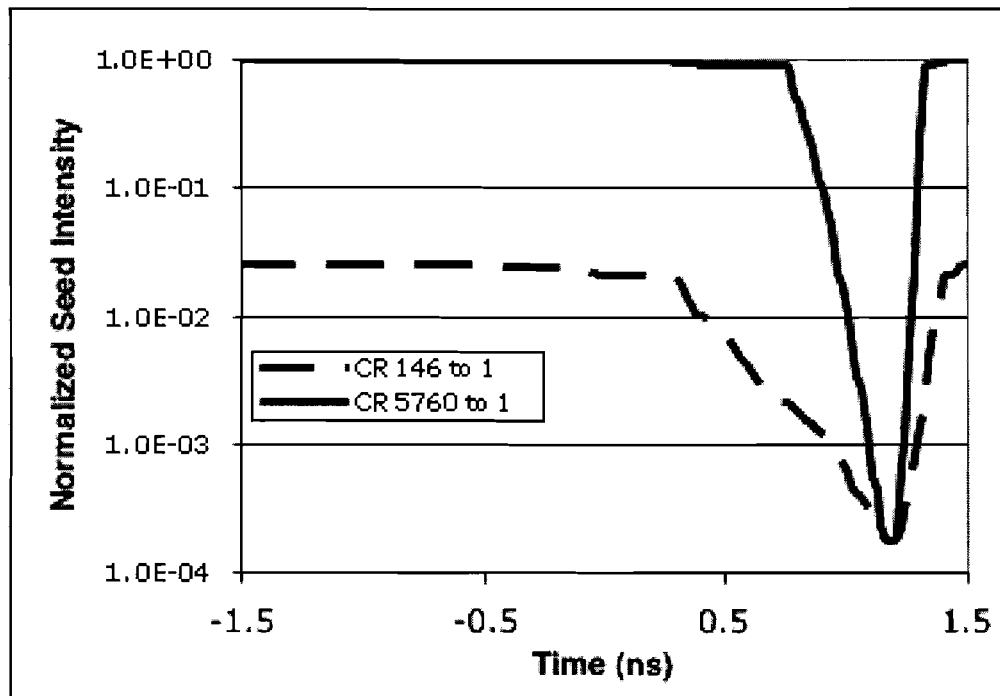


Figure 12: Plot of the higher contrast ratio seed shape (solid line) that corresponds to the higher contrast ratio pump shape of Fig. 11. The seed shape from Fig. 8 is also shown.

The high contrast pump and seed shapes produced a pre-compensated alpha308 pulse shape with better relative intensity stability than in any previous attempts. The relative stability was approximately a factor of 5 at the foot of the pulse (see Fig. 10, fine dashed line). A relative stability of a factor of 2 or better was predicted based on the relative stabilities of the points used to make the shape. The reason for the difference between the predicted stability and the actual stability is that there was a difference between the predicted output intensities and the actual output intensities. Although visually, the model output pulse shape and the desired output pulse shape look practically identical, there is as much as a 20% error at points at the foot of the output pulse. The percentage error is largest at the foot of the pulse because the local intensity values in this region are small. Percentage error is very low (less than 5%) at the peak of the output pulse. Since input values were specified by matching the peak local intensity of output produced by a flat-top seed and a linearly ramped pump with a desired local output intensity, a 20% error could mean that the local intensity actually produced is not the peak local intensity and not at the beginning of the reconversion regime. A closer match between predicted local intensities and actual intensities can be achieved by increasing the resolution of the pulse shapes used to determine the input shapes needed. Making numerous small adjustments to individual points at the foot of the output pulse would also be necessary. Time constraints on this project precluded attempts to increase the resolution or adjust the points.

V. Directions for Future Research

A third crystal may provide the flexibility needed to improve stability in the foot of the output pulse with lower contrast ratio input pulses. Adding a third crystal will also allow scaling to higher output energies since it can be configured as a separate amplification stage using a

pump beam with higher input energy than used with the first stage of amplification. The output energy obtained from the two-crystal system is intermediate between the energy obtained from the OMEGA regenerative amplifier and that obtained from the LARA. Thus the two-crystal system could replace the current regenerative amplifier. However, the third crystal would be necessary if the LARA replacement were also desired. In addition, since a different pump beam can be used with the third crystal, greater flexibility is allowed in defining input pulse shape requirements than with a single stage alone.

VI. Conclusion

A numerical computer model has been used to determine the input pulse shapes required to obtain the pre-compensated alpha308 pulse shape. A general methodology for determining input shapes applicable to any desired output pulse shape, not just the specific shape required by OMEGA, was described. Three sets of input shapes that produce the pre-compensated alpha308 pulse shape were presented. The first set contained a flat seed and a shaped pump, the second set contained a highly shaped seed as well as a shaped pump, and the third set contained very high contrast ratio seed and pump shapes. To my knowledge, this was the first time an OPA has been shown to be able to produce the highly shaped pulses necessary for Inertial Confinement Fusion lasers. A tradeoff between output pulse intensity stability and input pulse contrast ratio was discussed. The broadband amplification at the front end of OMEGA provided by an OPA can improve pulse smoothing techniques and therefore improve the uniformity of the target implosion. Improved target implosion uniformity will help improve the efficiency of ICF and potentially make fusion a viable energy source.

References

- (1) – Skupsky S, Craxton RS, “Irradiation uniformity for high-compression laser-fusion experiments,” *Physics Of Plasmas* **6** (5): 2157-2163 Part 2 May 1999
- (2) – Michael H. Key, “Fast Track to Fusion Energy,” *Nature* **412**, 775-776 (2001)
- (3) – M. J. Guardalben, J. Keegan, L. J. Waxer, V. Bagnoud, I. A. Begishev, J. Puth, and J. D. Zuegel, “Design of a highly stable, high-conversion-efficiency, optical parametric chirped-pulse amplification system with good beam quality,” *Opt. Express* **11**, 2511-2524 (2003), <http://www.opticsexpress.org/abstract.cfm?URI=OPEX-11-20-2511>
- (4) – J. D. Zuegel, et. al., “Prototype Front End for the OMEGA EP Laser System Using Optical Parametric Chirped-Pulse Amplification”, presentation given at Conference on Lasers and Electro-Optics (CLEO) in Baltimore, MD, June 1-6, 2003.

Automated Laser-Beam Steering

Margot Epstein

Automated Laser Beam Steering

Margot Epstein

Sodus High School

University of Rochester, Laboratory for Laser Energetics

Advisors: Wade Bittle, Jean Depatie

Abstract

To accomplish automated laser beam steering, a beam positioning algorithm has been derived to calculate the appropriate movement of two motors on a beam positioning mirror mount. This mirror is fixed on a stage that can rotate the mirror to any angle in order to simulate non-collinear positioning axes. The algorithm is implemented in a computer program capable of steering a laser beam to a specific position on a target image camera. The program accounts for non-collinear axis orientation between the mirror movement and the camera, scaling between mirror movement and camera beam position, beam centroid fluctuation, and the precision with which the user requires the beam to be from the specified target position. The program is then capable of moving the motorized mirror in order to steer the beam to any specified position on the target image camera.

Background

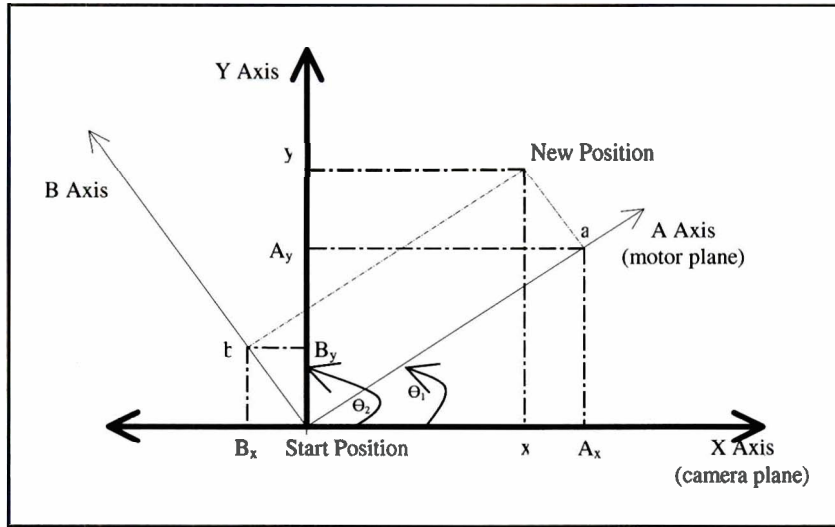
Currently, the University of Rochester's Laboratory for Laser Energetics (LLE) OMEGA laser system requires human interaction to steer the laser beams in a manual fashion. This process can be quite time consuming and is subject to human error. Researchers have proposed a solution to this problem: an automated beam steering system. An effective system or program had not been developed at LLE. An important

piece of an automated beam steering program is a way to find the centroid of the beam. This is very difficult to implement in the LLE OMEGA laser system because each beam is constantly contorting and changing shape resulting from beam turbulence.

There are two factors that affect the alignment of a beam, centering and pointing. Centering, which was the focus of this project, is steering the beam to be inside the circular reticule of a target, or in essence steering a beam to a specific position. Pointing is changing the angle of incidence to the target. A system that is to accommodate pointing, as well as centering, needs to have two positioning mirrors. Moving one mirror requires a compensating move in the other mirror. If the beam is not perfectly pointed or centered there is no way to tell which mirror is misaligned without the proper optical equipment. In order to be able to both point and center a beam, additional optical equipment is needed and is considered out of the scope of this project.

The goal of this project was to derive an algorithm to calculate the appropriate amount of movement of two orthogonal motors on a mirror in order to steer a beam to a specific position on a target image camera. The restricting factors were the rotation of the mirror and the beam noise. The mirror was mounted on a rotating stage in order to be able to arbitrarily change the angular orientation between the mirror axis and the camera axis. With a difference in axis orientation, the beam movement resulting from mirror repositioning is not parallel to the camera axis. Therefore, the algorithm must account for the need to move the mirror's positioning motors interactively. The geometry used to support the derivation of the algorithms is shown in Figure 1.

Figure 1. Motor and Camera Plane Geometry



$$x = A_x + B_x \quad (1)$$

$$y = A_y + B_y \quad (2)$$

The (X, Y) axes are in the camera plane and the (A, B) axes are in the motor plane. One of the mirror motors moves along the A axis, and the other moves along the B axis (motors A and B respectively). The motors, along with the (A, B) axes, can be rotated a complete 360° with respect to the camera or (X,Y) axes. x and y are the distances that the beam moves along the camera axes. a and b are the distances that the beam moves along the motor axes. Ax, Ay, Bx, and By are the distances that the beam moves on the camera plane as an effect of a move on the motor plane. Ax is equal to the distance the beam moved on the X axis as a result of an A axis move, Bx is the distance the beam moved on the X axis as a result of a B axis move, Ay is the distance the beam moved on the Y axis as a result of an A axis move, and By is the distance that the beam moved on the Y axis as a result of a B axis move. Using known incremental test moves

along the A and B axes the four scaling constants can be determined. The relationships between mirror motor (a, b) movements and the movement of the beam on the camera (X, Y) axes are:

$$A_x = a \cos \theta_1 = n_a \alpha_{ax} \quad (3)$$

$$A_y = a \sin \theta_1 = n_a \alpha_{ay} \quad (4)$$

$$B_x = b \cos \theta_2 = n_b \alpha_{bx} \quad (5)$$

$$B_y = b \sin \theta_2 = n_b \alpha_{by} \quad (6)$$

In Equation (3) through (6), a and b are the beam position moves scaled to the camera axes. Factors, n_a and n_b , are the actual number of mirror motor move iterations to produce A_x , A_y , B_x and B_y . The test moves provide the 4 scaling constants: α_{ax} , α_{ay} , α_{bx} , α_{by} . Through substitution into Equations (1) and (2) it can be concluded that:

$$x = n_a \alpha_{ax} + n_b \alpha_{bx} \quad (7)$$

$$y = n_a \alpha_{ay} + n_b \alpha_{by} \quad (8)$$

By applying the results from the program's test moves and the scaling constants, it can be concluded that the number of motor count iterations in a (n_a) and b (n_b) to move a distance x,y on the camera plane are given by Equations (9) and (10). These two equations are derived by simultaneously solving Equations (7) and (8) for n_a and n_b .

$$n_b = \frac{y \alpha_{ax} - x \alpha_{ay}}{\alpha_{ax} \alpha_{by} - \alpha_{ay} \alpha_{bx}} \quad (9)$$

$$n_a = \frac{x \alpha_{by} - y \alpha_{bx}}{\alpha_{ax} \alpha_{by} - \alpha_{ay} \alpha_{bx}} \quad (10)$$

Experimental Setup

The experimental setup for this program is shown in Figure 2.

Figure 2. Experimental Setup

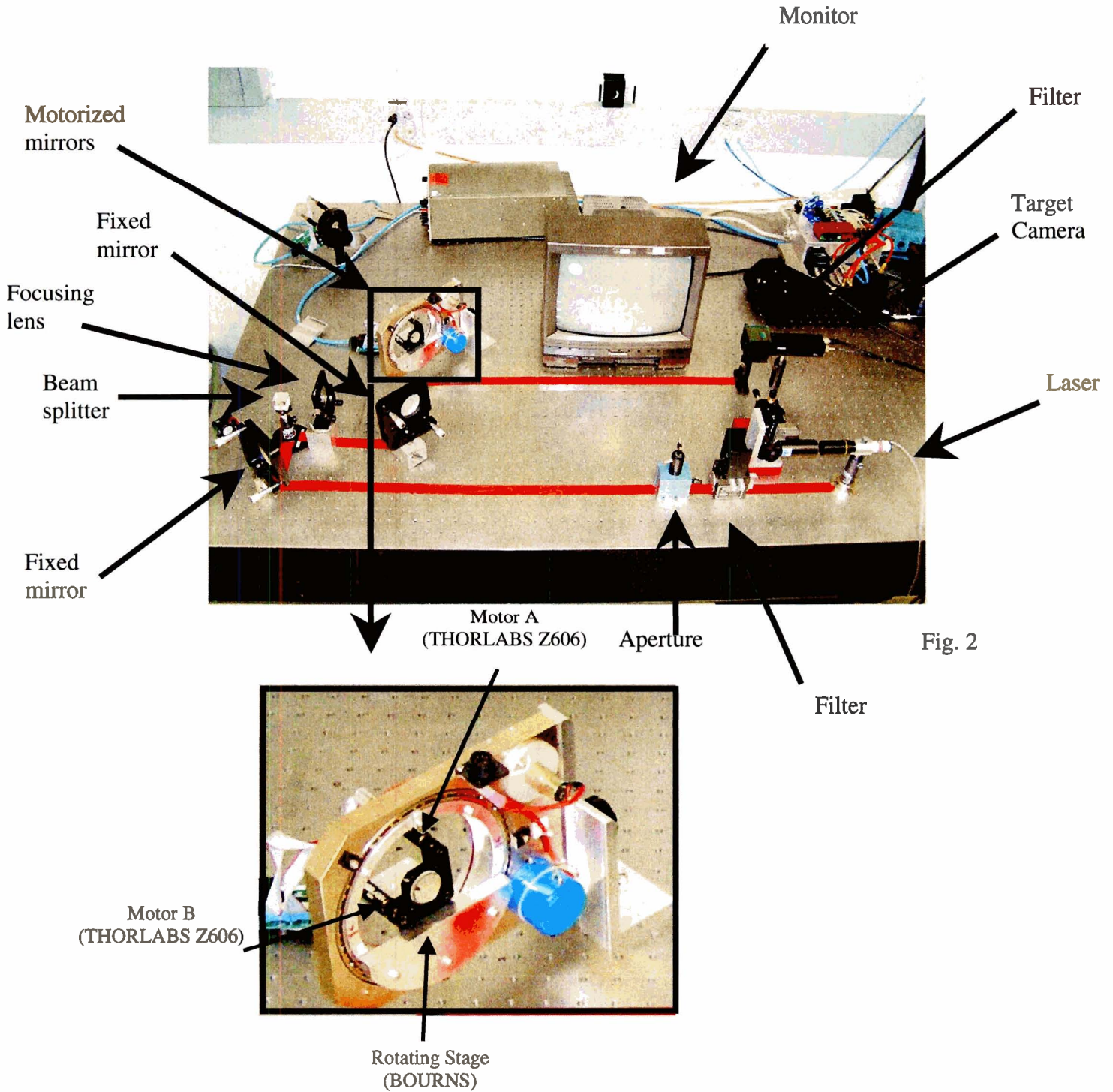
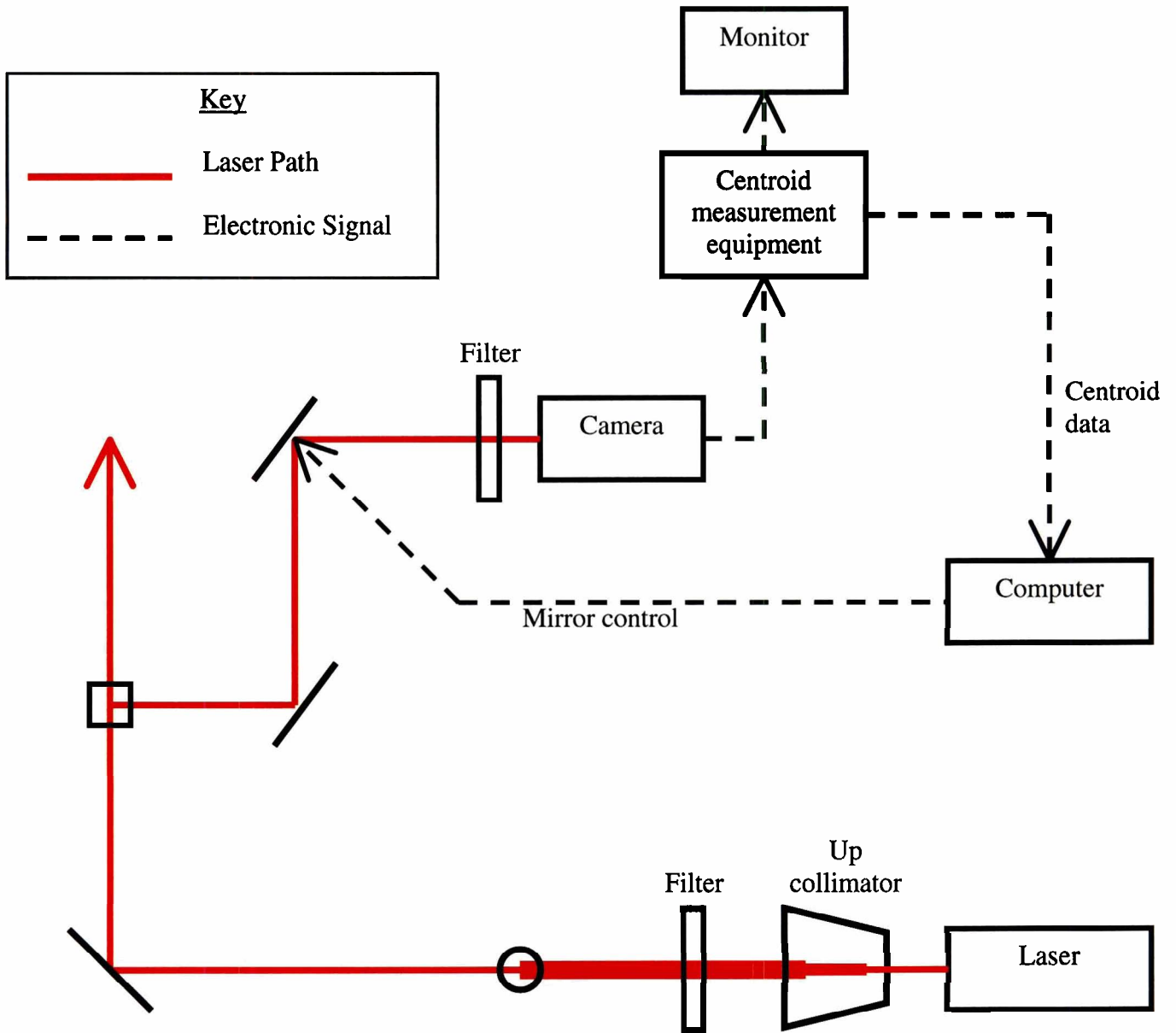


Figure 3. Schematic Layout of Experimental Setup



Schematic Layout

The schematic layout of this experiment is shown in Figure 3. The beam is produced by a low power visible class III A laser (Lasermex Inc. S/N – 711802). It is

then spread by an up-collimator (CVI model: BXUV 40-5x-355 S/N: 980428-13) and is filtered to reduce its intensity. An aperture to decrease the diameter of the beam follows the filter. The beam then bounces off a fixed mirror at 45° (this mirror has a fan attached in order to simulate beam turbulence) and goes through a beam splitter that is in place in order to accommodate another experiment on the same optical bench. The beam is then focused by a focusing lens (not shown), and makes a 90° turn at another fixed mirror. The beam then hits the motorized mirror that is controlled by the automated beam steering program. This mirror has two motors (THORLABS Z606) that control it and it is mounted on a rotating stage (BOURNS). After the motorized mirror, the beam is filtered again and enters the target image camera (PULNiX TM-745).

Program Procedure

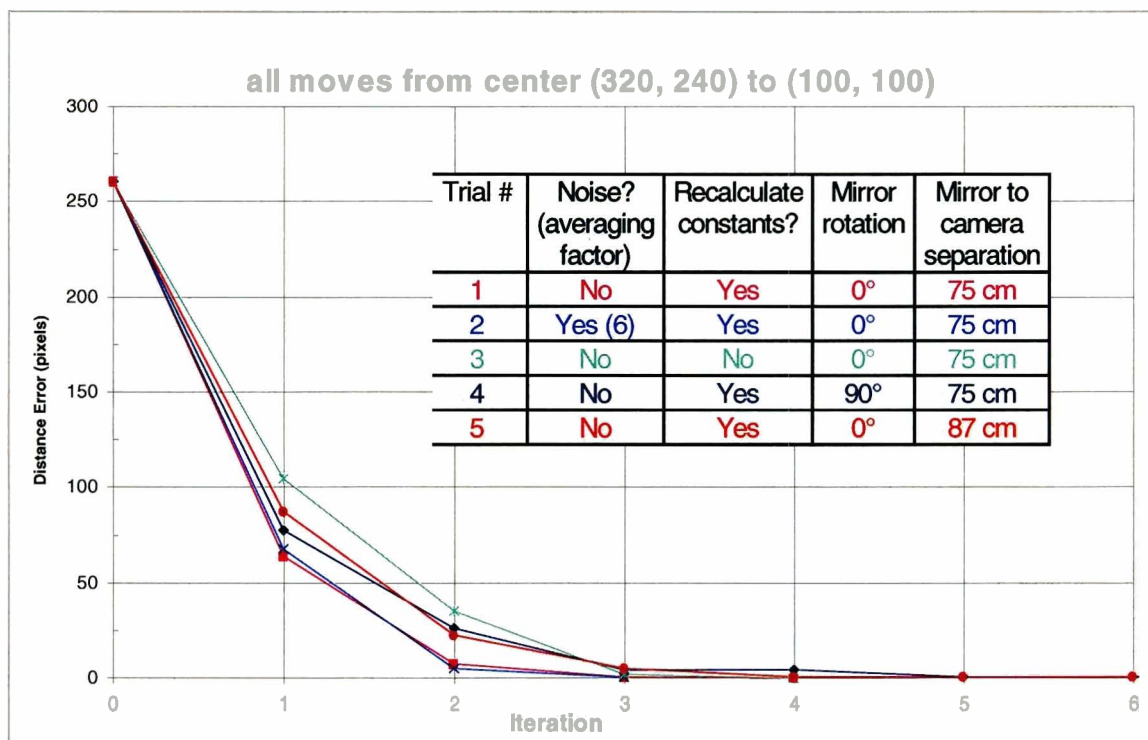
The program not only accounts for the axis difference between the mirror and the camera, but also accounts for beam turbulence, or noise. The program reads the position of the beam the number of times supplied by the user-determined averaging factor to find the average position of the beam with turbulence. The program uses the averaging factor to overcome the beam centroid noise. There are other variables that can be changed by the user. The user can choose to calculate the move constants every iteration by doing small test moves at each new position to find the relationship between mirror motor counts and beam movement on the camera. The user can also supply the program with an arbitrary goal position or can tell it to steer the beam to the center of the screen.

Program Results

After several tests, it was concluded that the program accomplishes the goal.

However, the completion of beam steering sometimes took more than one iteration. See Fig. 4 for a graph of results.

Figure 4. Experimental Results



The first trial was the control trial. There was no noise, the constants were recalculated every iteration, the mirror was not rotated, and the mirror to camera separation was 75 cm. For each trial, one variable was changed. The beam reached the goal position every trial within 6 iterations.

Future Developments

Currently, the automated beam steering program is only capable of centering the beam. In order to make the program able to point the beam, additional optical equipment is needed. In addition to adding a pointing capability, the motor control needs to be more accurate in order to steer a multi-beam laser system. This could be accomplished by compensating for backlash in the mirror motors. There may also be nonlinearities in the camera and positioning motors producing positioning errors that need to be determined and compensated for. However, regardless of the known and unknown error-producing factors, the program still works; it steers a laser beam very accurately.

Acknowledgements

This project could not have been as successful without the important roles of a few people. First, I would like to thank Wade Bittle and Jean-Francois Depatie. They were both excellent advisors, guiding me, but also letting me figure out things for myself. Also thanks to Dave Hasset and Rick Kidder for fixing my computer numerous times. To Dr. Craxton, you are great! This summer program is so wonderful and its existence is thanks to you!

Non-LTE Effects on the Speed of Sound in Plasmas

Wen-fai Fong

Non-LTE Effects on the Speed of Sound in Plasmas

Wen-fai Fong

Advisor: Reuben Epstein

Summer High School Research Program 2003

Laboratory for Laser Energetics

University of Rochester

Abstract

Local thermodynamic equilibrium (LTE) has been the standard assumption for thermodynamic calculations of plasma properties. Assuming non-LTE requires a modification of the first law of thermodynamics to account for radiation loss from the plasma. A corresponding correction to the entropy balance is added to complete a thermodynamic model that is consistent with a modification of LTE ionization. Under non-LTE, I consider a simplified collisional radiative equilibrium (CRE) model that accounts for radiative recombination as well as for collisional ionization and collisional recombination in determining the ionization state of a plasma. A sound wave creates perturbed regions of compression and decompression throughout the medium, in which the photon emission rate due to radiative recombination varies, relative to a uniform energy supply used to maintain the unperturbed plasma at a steady state. Using an adiabatic exponent accounting for the ionization energy of the plasma, an expression for the speed of sound is obtained in terms of various thermodynamic quantities. One-tenth solid density aluminum is used as an illustrative example. The speed of sound is plotted versus temperature for both LTE and CRE to show where there is a significant difference between these two assumptions.

I. Introduction

The propagation of a sound wave through a radiating plasma is both an irreversible and adiabatic process. A sound wave creates areas of compression throughout its medium, thereby causing the pressure of the medium to vary. Due to the rapidity of these pressure variations, we may assume that a negligible amount of thermal energy is exchanged between the compressed regions and their surroundings. Such a process is referred to as an *adiabatic* process.¹ An *irreversible* process is one in which the entropy of the universe permanently increases. Entropy (S) is a state function $S(T, V)$ and is expressed in LTE as:

$$dS = \frac{1}{T}dU + \frac{P}{T}dV \quad (1)$$

where U is the internal energy, V is the volume and T is the temperature. At constant entropy, when the medium is compressed, energy radiates due to radiative recombination.²

Local thermodynamic equilibrium (LTE) is the standard assumption for thermodynamic calculations. In assuming LTE, we assume time-reversibility of all processes. Non-local thermodynamic equilibrium (non-LTE) introduces irreversibility. Collisional-radiative equilibrium (CRE) is a case of non-LTE which includes the effects of both radiative and collisional recombination. Radiative recombination is a two-body interaction that occurs when an electron passes nearby a positive ion. The ion's electrostatic forces accelerate the electron, thus causing it to radiate and emit a photon. With the emission of the photon, the electron's velocity decreases, and it becomes bound to the ion. When the photons escape from the plasma, radiative recombination causes a loss of energy. On the other hand, collisional recombination is a three-body interaction, occurring when two free electrons collide near an ion. One electron remains free, while the other becomes bound to a nearby positive ion. Unlike radiative recombination, collisional recombination does not entail energy loss from the plasma.

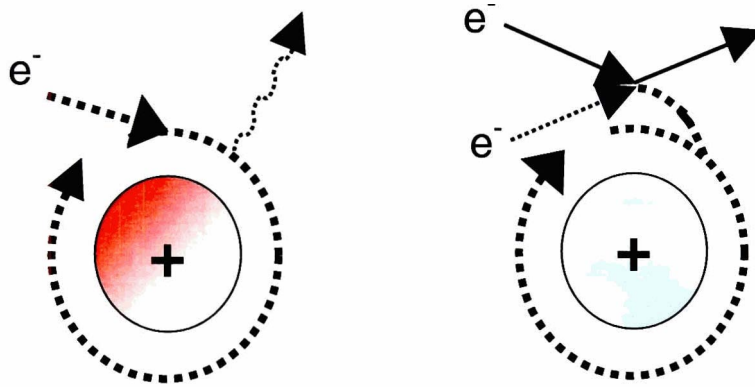


Fig. 1. Radiative recombination (left), and collisional recombination are displayed.

Collisional-radiative equilibrium accounts for radiative recombination as well as collisional ionization and recombination. However, it does not account for photoionization, the time-reversed process of radiative recombination. Therefore, the energy lost in radiative recombination is not recovered by the plasma itself.

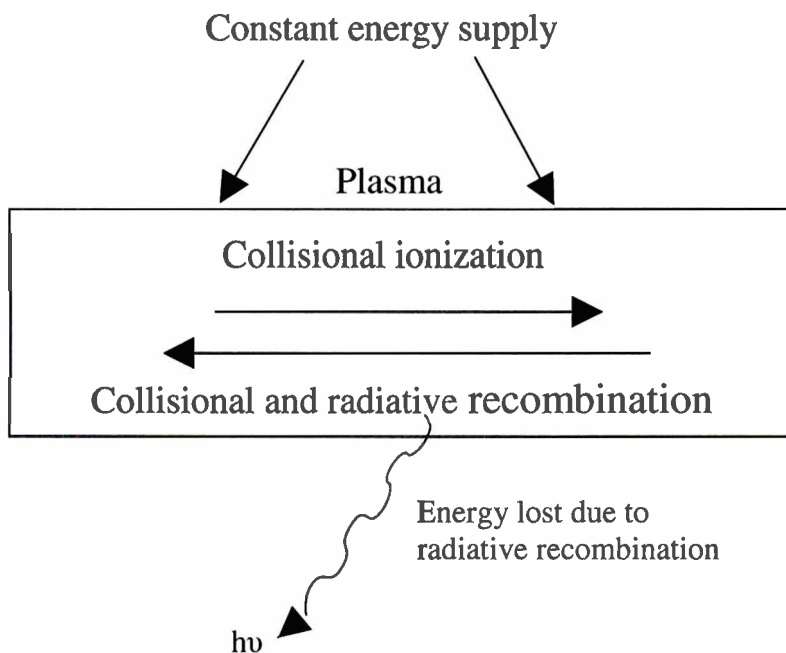


Fig. 2. A conceptual picture of the energy balance in the plasma to maintain a steady state.

As a sound wave propagates through the plasma, it creates regions of compression

and decompression throughout the medium. In regions of compression, there is an increased number of collisions as particles are pushed closer together. The radiative recombination rate increases with compression, along with energy loss. In regions of decompression, there is a decreased number of collisions as particles are pushed farther apart, resulting in a decrease in the rate of radiative recombination and less energy loss. A constant, uniform energy supply is provided to the plasma to compensate for the average rate of energy loss due to radiation and thus maintains the overall steady state of the unperturbed plasma. Collisional radiative equilibrium, under non-LTE, accounts for both collisional and radiative recombination, assuming that no photoionization occurs.³

II. Calculations

The exchange of heat $d_e Q$ into the plasma from the environment is given by:

$$d_e Q = dU + pdV \quad (2)$$

where Q is the heat of the plasma, U is the internal energy of the plasma, and p and V are the pressure and volume of the plasma, respectively. Prigogine and Kondepudi³ account for the interior and exterior energy and entropy balances of the plasma by the first and second laws of thermodynamics. The irreversible radiated energy loss in excess of the energy added by the total constant, uniform heat source is denoted as $d_i Q$. The total change in the heat of the plasma is

$$dQ = d_e Q + d_i Q. \quad (3)$$

Assuming CRE, the energy balance is accounted for by

$$dQ = dU + pdV + \mu_{CR} dN^+, \quad (4)$$

where $d_i Q = \mu_{CR} dN^+$ accounts for the loss of energy due to radiative recombination. Dr. Epstein⁴ expresses μ_{CR} as the ionization energy $\chi(N^+)$ multiplied by the probability that recombinations occur radiatively, as opposed to collisionally. In LTE, μ_{CR} is equal to zero, so $dQ = dU + pdV$.

A corresponding correction is made to the entropy balance:

$$dS = \frac{1}{T} dU + \frac{P}{T} dV + \frac{\mu_{CR}}{T} dN^+ \quad (5)$$

U is a function of temperature and particle numbers and can be defined by

$$U = \frac{3}{2} NkT + \int^{N^+} \chi(N^{+'}) dN^{+'} \quad (6)$$

$$dU = \frac{3}{2} NkdT + \left(\frac{3}{2} + \chi \right) dN^+ \quad (7)$$

where N^+ is the number of ions in the plasma in a given ionization state and k is Boltzmann's constant. $\chi(N^+)$ is the ionization energy for a particular ionization stage and is a slowly varying function of N^+ . Notice that $3/2 NkT$ is the expression for energy of ideal monatomic gases. The equation of state is

$$PV = NkT, \quad (8)$$

where N is the number of particles in the plasma. Using Eq. 4, the specific heats at constant volume and at constant pressure follow, respectively:

$$c_v = \left(\frac{\partial Q}{\partial T} \right)_v = \left(\frac{\partial U}{\partial T} \right)_v + \mu_{CR} \left(\frac{\partial N}{\partial T} \right)_v \quad (9)$$

$$c_p = \left(\frac{\partial Q}{\partial T} \right)_p = \left(\frac{\partial U}{\partial T} \right)_p + P \left(\frac{\partial V}{\partial T} \right)_p + \mu_{CR} \left(\frac{\partial N}{\partial T} \right)_p \quad (10)$$

To simplify these expressions, we introduce the parameters $\eta_v \equiv \frac{V}{N} \left(\frac{\partial N}{\partial T} \right)_v$ and $\eta_T \equiv \frac{T}{N} \left(\frac{\partial N}{\partial V} \right)_T$,

where the change in the number of ions N^+ equals the change in the number of free particles N ($dN = dN^+$). The specific heats are expressed as:

$$c_v = \frac{3}{2} Nk + Nk\eta_T \left(\frac{3}{2} kT + \frac{\chi + \mu_{CR}}{kT} \right) \quad (11)$$

$$c_p = \frac{5}{2} Nk + \left[\frac{(\eta_T + \eta_V) \left(\frac{5}{2} + \frac{\chi + \mu_{CR}}{kT} \right) (Nk)}{1 - \eta_V} \right]. \quad (12)$$

In Clayton,⁵ a dimensionless quantity γ_1 is the first adiabatic exponent out of three. It is defined as

$$\frac{dp}{p} + \gamma_1 \frac{dV}{V}. \quad (13)$$

Clayton⁵ also derives an expression for γ_1 in terms of the specific heats at constant volume and pressure, respectively:

$$\gamma_1 = -\frac{c_p}{c_v} \left(\frac{\partial p}{\partial V} \right)_T \frac{V}{p} \quad (14)$$

$$\left(\frac{\partial p}{\partial V} \right)_T = \frac{NkT(\eta_V - 1)}{V^2} \quad (15)$$

This is purely a result of the first law of thermodynamics and the equation of state. If Eq. 11 and Eq. 12 are substituted into Eq. 14, γ_1 is now expressed in terms of ionization:

$$\gamma_1 = \frac{\frac{5}{2}(1 + \eta_T) + (\eta_T + \eta_V) \left(\frac{\chi + \mu_{CR}}{kT} \right)}{\frac{3}{2}(1 + \eta_T) + \eta_T \left(\frac{\chi + \mu_{CR}}{kT} \right)}. \quad (16)$$

The parameters used are now more specifically defined in terms of ionization:

$$\eta_T = \frac{T}{1 + Z} \left(\frac{\partial Z}{\partial T} \right)_V \quad (17)$$

$$\eta_v = -\frac{\rho}{1+Z} \left(\frac{\partial Z}{\partial \rho} \right)_T. \quad (18)$$

Entropy S (Eq. 1) is an analytic function and therefore displays reciprocity:

$$\frac{\partial}{\partial T} \left[\left(\frac{\partial S}{\partial V} \right)_T \right]_V = \frac{\partial}{\partial V} \left[\left(\frac{\partial S}{\partial T} \right)_V \right]_T. \quad (19)$$

This characteristic indicates that the value of entropy does not depend on its history, but rather, on its present state. S can now be expressed in terms of the parameters just defined:

$$\eta_v \left(\frac{3}{2} kT + \chi + \mu_{CR} \right) = \eta_T kT. \quad (20)$$

Eq. 20 can be used to simplify Eq. 16.

$$\gamma_1 = \frac{\frac{5}{2} \eta_v (1 + \eta_T) + (\eta_T + \eta_v) \left(\eta_T - \frac{3}{2} \eta_v \right)}{\frac{3}{2} \eta_v (1 + \eta_v) + \eta_T \left(\eta_T - \frac{3}{2} \eta_v \right)}. \quad (21)$$

Assuming that this propagation is an adiabatic change with radiation energy loss and both the energy and entropy balances accounted for,

$$c_s^2 = \frac{\gamma_1 P}{\rho}. \quad (22)$$

Eq. 16 and Eq. 22 give

$$c_s^2 = \frac{\frac{5}{2} (1 + \eta_T) + (\eta_T + \eta_v) \left(\frac{\chi + \mu_{CR}}{kT} \right)}{\frac{3}{2} (1 + \eta_T) + \eta_T \left(\frac{\chi + \mu_{CR}}{kT} \right)} \frac{NkT}{V\rho}, \quad (23)$$

where ρ is the mass density. Plugging Eq. 20 into Eq. 23,

$$c_s^2 = \frac{\frac{5}{2}\eta_v(1+\eta_T) + (\eta_v + \eta_T)\left(\eta_T - \frac{3}{2}\eta_v\right) NkT}{\frac{3}{2}\eta_v(1+\eta_T) + \eta_T\left(\eta_T - \frac{3}{2}\eta_v\right) V\rho} \quad (24)$$

is obtained.

This expression for the speed of sound applies to both LTE and CRE. The Saha equation for LTE is stated

$$\frac{N^{n+1}N_e}{N^n} = AT^{\frac{3}{2}}e^{-\frac{\chi}{kT}} \quad (25)$$

where A is a constant. For a partially ionized gas, N^n is the number of n -times ionized ions in a given ionization state and N_e is the number of electrons.⁶ Assuming CRE, the Saha equation can be modified in order to be consistent with the thermodynamic consistency condition Eq. 20,

$$\frac{N^{n+1}N_e}{N^n} = AT^{\frac{3}{2}}e^{-\frac{\chi+\mu_{CR}}{kT}} \quad (26)$$

Eq. 21 can now be evaluated in a thermodynamically consistent manner in terms of Eq. 26.

III. Results

For evaluating Eq. 24, tables of χ , $\frac{T}{Z}\left(\frac{\partial Z}{\partial T}\right)_v$, $\frac{\rho}{Z}\left(\frac{\partial Z}{\partial \rho}\right)_T$, and average Z for

aluminum plasma at one-tenth solid density were provided. For CRE, all ionization effects of spontaneous emission were removed. These were obtained from collisional-radiative calculations provided by Dr. R. Epstein.⁴

The average Z is plotted in Fig. 3 against temperature. The CRE curve displays a similar pattern to the LTE curve, but requires a higher temperature to reach a given ionization state. This is due to the lack of photoionization occurring in a non-LTE plasma, where energy is lost due to radiative recombination. A “jump” occurs at eleven detached electrons ($z=11$)

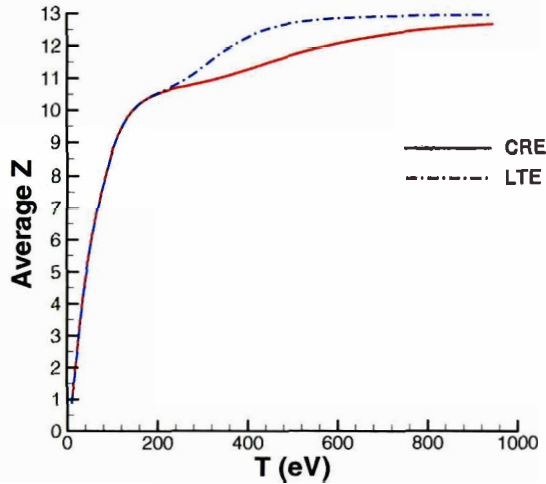


Fig. 3. The average charge per ion for aluminum at one-tenth solid density is plotted as a function of temperature.

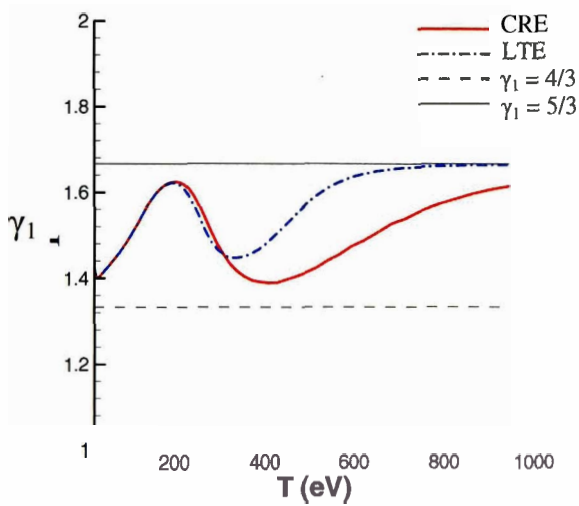


Fig. 4. γ_1 for aluminum at one-tenth solid density is plotted as a function of temperature.

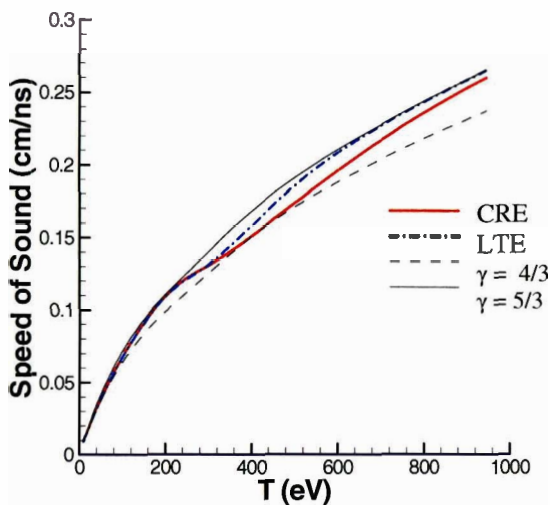


Fig. 5. The speed of sound for aluminum at one-tenth solid density plotted as a function of temperature.

because only the innermost complete shell is left, and a significant increase in the ionization energy occurs at that point.

A Fortran program⁷ is used to evaluate the values of γ_1 and the speed of sound for CRE and LTE through Eq. 21 and 24. These values are then plotted against temperature (Fig. 4). Like Fig. 2, the CRE curve displays a similar pattern to the LTE curve but with a similar temperature shift. In this case, $\gamma_1 = 5/3$ corresponds to a neutral gas in which no ionization occurs, or a fully ionized plasma or a plasma with constant ionization.

Since γ_1 is an important part of the speed of sound equation, the same pattern can be seen in Fig. 5, where the speed of sound is plotted. Once again, the CRE curve displays a similar pattern to the LTE curve.

IV. Significance

The assumption of non-LTE thermodynamics is significant in that the behavior of sound waves propagating through a plasma is similar to that of shock waves, which often propagate within the target chamber. Studying the apparent difference between the speed of sound under both LTE and non-LTE conditions can further laser-induced nuclear fusion studies. These differences can be attributed to ionization effects. These non-LTE effects should be studied in other low-density substances, in order to find other cases of interest. For instance, carbon at one-thousandth solid density is another interesting case where there is a significant difference in average Z between LTE and CRE. There also may be other ways to perform the non-LTE calculations, taking factors other than ionization, energy and entropy into account.

V. Conclusions

In order to perform thermodynamically consistent calculations of the speed of sound of an aluminum plasma at one-tenth solid density, the energy and entropy balance must be accounted for in the first and second laws of thermodynamics. This effect of radiative recombination can be accounted for by the μ_{CR} term in the energy balance. This allows thermodynamic consistency in the calculation for the γ_1 and the speed of sound. As shown by the case of aluminum at one-tenth solid density, the effects of non-LTE and CRE can be significant at low densities. Given a high-density substance, collisional ionization and recombination are favored over radiative recombination and photoionization. For low-density substances such as gases and plasmas, the effects of non-LTE and CRE can be seen because the radiative processes are more important, and the energy lost due to radiation is accounted for. It

can be reasonably conjectured that significant differences in LTE and non-LTE are likely to be seen where these effects are seen in ionization.

VI. Acknowledgments

I would like to take this opportunity to thank Dr. Epstein, my advisor, for being patient and teaching me these past eight weeks. I would also like to acknowledge Dr. Craxton for coordinating and putting this program together. Thank you to the people at the Laboratory for Laser Energetics, who were kind enough to sponsor this intensive research program.

VII. References

1. Katz, J. I., *High Energy Astrophysics*, 1987, Menlo Park: Addison-Wesley.
2. Huang, K., *Statistical Mechanics*, 1987, New York: John Wiley and Sons, Ltd.
3. Kondepudi, D. and Prigogine, I., *Modern Thermodynamics*, 1998, New York: John Wiley and Sons, Ltd.
4. Dr. R. Epstein – private communication
5. Clayton, D. D., *Principles of Stellar Evolution and Nucleosynthesis*, 1968, New York: McGraw-Hill.
6. Pomraning, G. C. *The Equations of Radiation Hydrodynamics*, 1973, New York: Pergamon Press Ltd.
7. Gehrke, W., *Fortran 90 Language Guide*, 1995, New York: Springer-Verlag London Limited.

**Energy and Angular Distributions of Secondary Electrons Under High
Electric Field**

Christopher Forbes

Energy and Angular Distributions of Secondary Electrons under High Electric Field

Christopher Forbes

Eastridge Senior High School

LLE Advisor: Paul Jaanimagi

X-ray bombardment of a photocathode produces high-energy primary photoelectrons, which in turn produce a multitude of low-energy secondary electrons. We use a 60° cylindrical analyzer to disperse the secondary electrons onto a phosphor screen, according to their transverse velocity and axial energy. The phosphorescence is recorded with a scientific-grade CCD camera. Changing the electron dispersion allows for full analysis of the energy distribution, particularly the axial component. Under a high-voltage accelerating field, we expect the electron angular and energy distributions to vary from results obtained under a low electric field. The angular distribution ought to become more forward directed than Lambertian, with the energy distribution increasing in the axial direction. We have verified that the transverse energy distribution is not modified by a large axial accelerating field.

I: Introduction

We investigated how a large axial electric field modifies the energy and angular distribution of the secondary electron emission from an x-ray sensitive photocathode. While interest in this topic has existed for over 30 years, no one has ever experimentally measured it. Many scientists have speculated that the angular distribution of the electrons

would not be Lambertian, as it is under low electric field, but that the angular distribution will become more forward directed.¹ Energy is expected to increase in the axial direction, with the transverse energy remaining the same as under low field. Despite all this speculation, no one has ever conducted such an experiment, so these expectations have not been corroborated.

Past experiments have had some similarities to our current research. However, either the electric field was significantly weaker or the distributions were not measured. In an experiment measuring the angular distribution of photoelectrons, it was found to be roughly Lambertian. However, this occurred in a low electric field, which would have minimal impact on the electron distribution.² Henke et al.³ in 1979 published his work on the total energy distribution curves of x-ray induced secondary electron emissions. This experiment did not measure the axial and transverse energy distributions, but only the total energy distribution. Assuming a Lambertian angular distribution, the axial and transverse energy distributions can be calculated using Henke's data (see Figure 1). In a Lambertian angular distribution, the radial energy component is equivalent to the axial energy component. A further past experiment looked at the effect of high electric fields on photocathodes. This found that stronger electric fields resulted in greater electron emissions from photocathodes.⁴ While the experiment was under high field, neither energy nor angular distributions were measured. Despite sharing some similarities, all of these experiments are notably different than our current research.

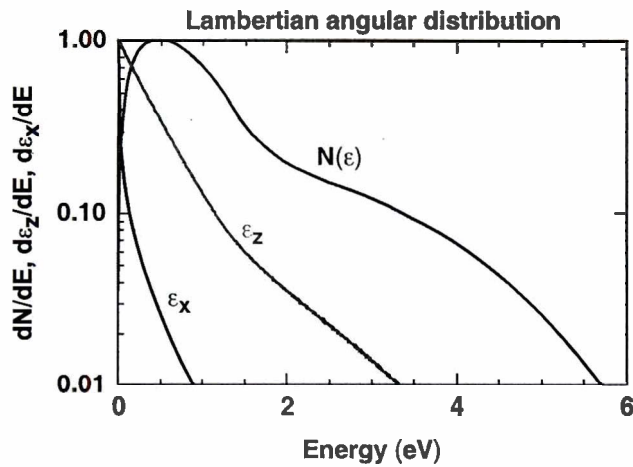


Figure 1: Henke's³ energy distribution curves for a KBr photocathode, assuming a Lambertian distribution. $N(\epsilon)$ is the total energy, ϵ_z is the axial energy, and ϵ_x is a transverse energy component.

Our experiment is designed to measure the axial and transverse energy distributions under a high axial electric field. By measuring the energy distributions, the angular distribution can then be derived. The accelerating electric field reached as high as 12 kV over 4 mm, or 3 kV/mm. A cylindrical analyzer disperses the electrons with either high or low electron dispersion. The dual dispersion modes allow us to determine the axial and transverse energy components. In particular, the axial energy would be difficult to determine if the distribution were non-Lambertian. Even with both high and low dispersion, the axial energy is still challenging to determine. In fact, this experiment has not been conducted previously due to difficulties in measuring the distributions properly. However, through utilization of the cylindrical analyzer, measuring the distributions has become theoretically possible.

This research is significant for a number of reasons. For streak cameras, the time resolution is given by $\Delta t \propto \epsilon_z^{1/2} / E_z$, where ϵ_z is the axial energy and E_z is the axial electric field. By increasing the axial accelerating electric field, time resolution

improves. However, this could also increase the axial energy, worsening the time resolution. Therefore, knowing the effects on the axial energy are essential for improving time-of-flight dispersion for photocathode-based electron sources. Large accelerating fields also allow for increasing the space-charge limited current density, given by $J \propto E_z^{3/2}/d^{1/2}$, where d is the field distance. This means that a stronger field results in a stronger current and consequently, a stronger signal. Our research seeks to experimentally measure the secondary electron distributions under a high accelerating field, as well as to confirm Henke's data taken under a low electric field. This will end speculation and allow for practical use of this knowledge.

In section II, we discuss the background information relevant to understanding our experiment. In section III, the setup used will be presented in detail. Section IV will discuss our experimental results using the cylindrical analyzer.

II: Background

The angular distribution of photoelectrons under low electric field has been previously found to be Lambertian.² Lambert's Law states that the emission in a direction θ is given by $I_\theta = (I_0/\pi)\Delta A \cos \theta$, where ΔA equals the area emitting radiation, and I_0 is the rate of emission per unit area integrated over all angles. A Lambertian distribution is azimuthally symmetric. The radiation emitted in a zone having apex angle θ is $i_\theta = \int_0^\theta di_\theta = I_0\Delta A \sin^2 \theta$.

A photocathode is a material that emits electrons when bombarded with photons of sufficient energy. The energy must be higher than the work function of the material. Any energy the photons have beyond the work function can be transferred to electrons in the form of kinetic energy. A single photon can also produce multiple electrons, or the absorption of multiple photons can release one electron, providing energy levels are appropriate. Most of these emitted electrons are pulled back to the cathode due to electrostatic attraction. However, by using an accelerating electrical field, most of the electrons will escape the attraction of the photocathode.

With x-ray photocathodes, secondary electrons are the principal emission rather than primary photoelectrons (see Figure 2). The primary photoelectrons are high energy and collide with multiple other electrons, giving these secondary electrons the necessary energy for ionization and subsequent release from the photocathode. The secondary

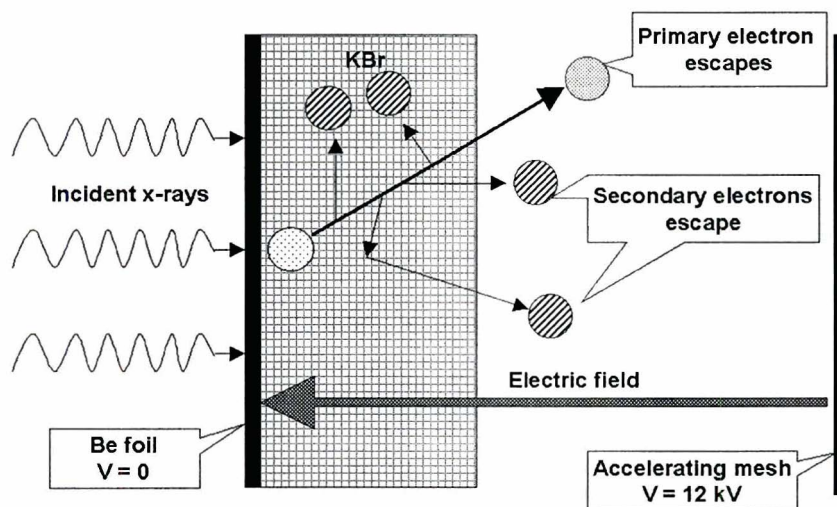


Figure 2: Illustrated is the escape of a high-energy primary electron from a dielectric photocathode. In the escape process, numerous low-energy secondary electrons are produced. A high electric field increases the electron yield from the photocathode.

electrons produced in this manner may outnumber the primaries by a factor of 10 or even 100. While primary electrons are still emitted, for our experiment they amount only to noise. They have too much energy to be directed easily, which is why secondary electrons are used in their stead.

III: Apparatus

The cylindrical analyzer is constructed of aluminum with macor (machinable ceramic) for insulation between metal parts of differing potential. The x rays are produced by a large area x-ray source. This means that illumination is fairly uniform along the photocathode. The entire apparatus is contained within a Ten-Inch Manipulator (TIM), a vacuum chamber with pressures as low as 10^{-8} torr. In practice, the experiment was conducted on the 10^{-7} to 10^{-6} torr range. As such, all of the screws are vented to prevent the gradual leak of air trapped below the screws and in their threads. Furthermore, all the parts are extremely clean to prevent oils from evaporating in the low pressure, as this would increase the pressure within the vacuum chamber. The o-rings must be particularly clean also, as even specks of dust could interfere with establishing a truly airtight seal.

The x rays arriving at the cylindrical analyzer are absorbed in a KBr photocathode. The KBr is coated on a thin layer of beryllium, which supports the coating and carries the photocathode voltage. Half of the beryllium is blocked and has no coating, allowing us to differentiate the signal from the noise. The secondary electron

emissions from this photocathode first travel to the accelerating mesh screen. The photocathode is set at -12 kV and the accelerating mesh can be set at approximately -11.9 kV, -11.59 kV, -8.38 kV, -5.3 kV, and 0 V. This results in an accelerating electrical field at 100 V, 410 V, 3.62 kV, 6.7 kV, and 12 kV over 4 mm, respectively. The mesh screens are made of extremely fine copper and allow for independent variation of electrical fields. Electrons are able to pass through, but electric fields are prevented from spreading to undesired locations.

Next the electrons travel between the accelerating mesh screen and the initial center potential mesh screen. Upon passing through this second screen, the electrons enter the cylindrical analyzer. In the analyzer, electrons travel between concentric cylinders through a 60° arc before encountering another mesh screen. Inside the arc, the

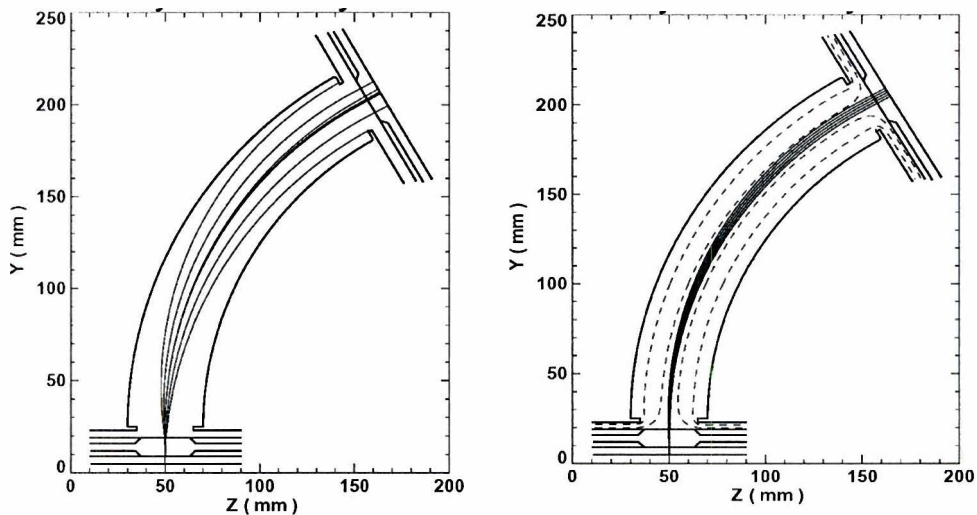


Figure 3: To the left is the electron ray trace of the cylindrical analyzer under high dispersion, and to the right is the ray trace under low dispersion. The dashed lines in the low dispersion image are equipotential lines on 1 kV intervals. The transverse energy of the electrons is dispersed far from the center under high dispersion, with the axial energy dispersed closely around the center. The electron beams originate at the photocathode and terminate at the phosphor screen.

electric field can be adjusted to high or low voltage to control dispersion of the electrons (see Figure 3). The higher voltages, around +2 kV inner and -2 kV outer with center at ground, result in low electron dispersion. High dispersion of the electron distribution is obtained with low voltage on the analyzer (-11.59 kV center).

After passing through the third mesh screen (also center potential), the electrons collide with an aluminized phosphor screen, lighting up wherever they hit. The more electrons that hit a spot, the brighter the phosphor glows. The aluminum coating provides a ground plane, prevents light from entering through the analyzer, and ensures that all light emitted from the phosphor is received by the CCD camera. This collected image can later be analyzed to determine the desired energy and angular distributions.

A Spectral Instruments 800 series CCD camera records the image of the phosphor screen. The CCD is operated at -40° Celsius, chilled by a thermoelectric cooler. This ensures that dark current is kept to a minimum. The camera has a resolution of 2,048 by 2,048, with 13.5 micron pixel size. Exposures were taken for ten second intervals to achieve a large signal to noise ratio. Background was also subtracted from the images for cleaner results.

A 60° arc is used for the cylindrical analyzer due to the source demagnification at that point. This allows us to use a larger electron source, thereby getting a stronger signal. Under low dispersion, the source magnification was 0.1, and under high dispersion it was only 0.03. At 60° the electrons are also well dispersed, with the

analyzer fitting nicely within the vacuum chamber. A larger arc could be difficult to employ for use within the limited space of the vacuum chamber, especially because we need an x-ray source facing the photocathode.

IV: Experimental Results

The most significant finding is the transverse energy distribution. The transverse energy under high electric fields agreed with Henke's data for the total energy distribution and a Lambertian angular distribution (see Figure 4). At low electron energies, the correlation was very strong. However, on reaching higher energy levels, a slight discrepancy developed. While seemingly erroneous, this divergence was consistent with the signal-induced noise we encountered.

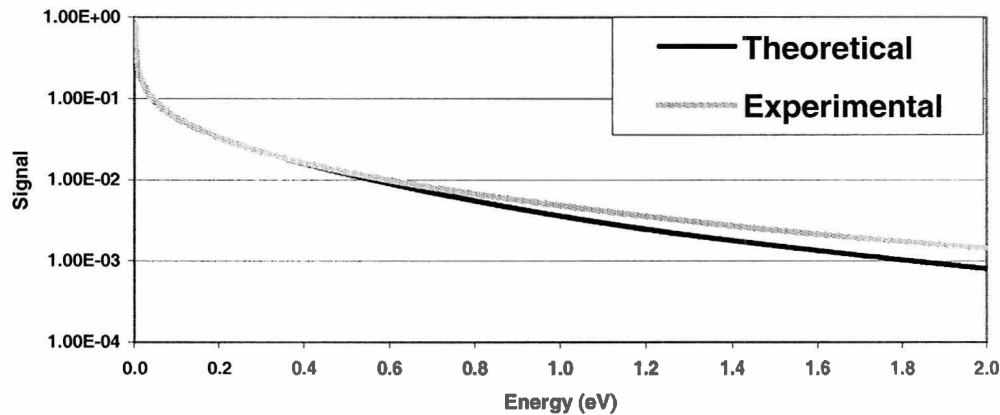


Figure 4: Graph of transverse energy distribution based on Henke's data (Theoretical) versus the transverse energy distribution we measured (Experimental). Note the close correlation at low energy levels, where there was a strong signal. Our data was taken under a 6.7 kV/4 mm electric field in low dispersion mode.

We encountered a significant amount of signal-induced noise. We believe this to be caused by electrons intercepted by the two foremost meshes. We have determined that the noise is from electrons originating by the photocathode end, as the noise shifts with the signal. Electrons produced at the phosphor screen end of the analyzer would not shift when we adjust voltages on the cylinders. The large amounts of signal-induced noise led to distributions leveling off prematurely, giving us increased readings at higher electron energy levels. We also encountered some unexpected asymmetries in some of our images. However, upon analysis there was strong enough signal that the transverse distribution could be derived.

The condition of the photocathode used may have introduced small amounts of error into our data. The photocathode coating was old, and it was visibly apparent that it was not in the best of shape. It had limited exposure to atmospheric conditions, meaning that some moisture was absorbed. This is known to lower the quantum efficiency of photocathodes. However, it is not known whether moisture absorbed by a photocathode modifies the electron angular and energy distributions.

Our data was optimal under a 1.675 kV/mm electric field (see Figure 5). At our highest field (3 kV/mm), the signal-to-noise ratio was worse, resulting in less clean results. The 1.675 kV/mm case had a strong signal, being second highest in voltage, but lacked the level of noise in the 3 kV/mm images. Despite significant noise, we were still able to obtain data at all five voltages under low dispersion. In high dispersion mode, large amounts of signal-induced noise contaminated the broader signal peaks and prevented us from deriving the axial energy distribution.

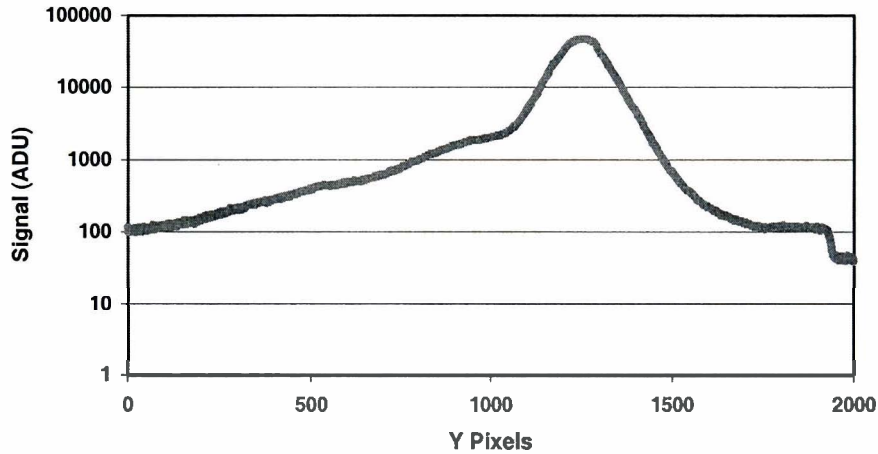


Figure 5: Lineout of image taken in low dispersion mode under a 6.7 kV/4 mm electric field. The transverse velocity is dispersed over space. Visible is the strong signal peak, as well as the signal-induced noise to either side of it.

Obtaining the axial energy distribution relies upon our ability to take clean data under both high and low dispersion. Low dispersion mode isolates the transverse velocity distribution by keeping the axial dispersion under 1 pixel/eV, with the transverse dispersion at $98.5 \text{ pixels}/\sqrt{eV}$. The dispersions are measured from the peak of the signal. Under high dispersion, the transverse dispersion is $558.5 \text{ pixels}/\sqrt{eV}$, while the axial is 20 pixels/eV. By subtracting the transverse energy distribution acquired under low dispersion from the total energy distribution, the axial energy distribution can be found. With both the axial and transverse energy distribution curves, the angular distribution can then be derived.

V: Conclusion

We have verified the transverse energy distribution curves based on Henke's data for the total energy distribution and a Lambertian angular distribution. We also

confirmed that the transverse energy distribution does not change under a high axial accelerating field. Notable levels of signal-induced noise generated by electrons intercepted by the meshes prevented us from extracting the axial energy distribution. Accordingly, the angular distribution under high electric field has not yet been verified.

Future versions of the cylindrical analyzer will be based upon a pulsed system. This should allow for higher accelerating fields, as well as reducing the signal-induced noise. If successful, the axial energy distribution can then be determined. Also, a further look into the copper meshes and any possible substitutes should be taken in an effort to reduce the noise we experienced.

Acknowledgements

First and foremost I would like to recognize my advisor at LLE, Dr. Paul A. Jaanimagi, whose hard work made this project a reality. I would also like to thank Mr. Bob Boni for his assistance in the construction of the setup, and Dr. Stephen Craxton for heading the Summer High School Research Program. Lastly, I would like to express my gratitude for all of the others at LLE who assisted throughout the course of the project. I am truly appreciative of the effort that was put into my project and the summer program as a whole.

References

-
1. J. Cazaux, "A new analytical approach for the transport and the emission yield of secondary electrons from insulators," *Nucl. Instr. and Meth. In Phys. Res. B* **192**, 381-392 (2002).
 2. H.E. Ives, A.R. Olpin, and A.L. Johnsrud, "The distribution in direction of photoelectrons from alkali metal surfaces," *Phys. Rev.* **32**, 57-81 (1928).
 3. B.L. Henke, J. Liesegang, and S.D. Smith, "Soft -x-ray-induced secondary-electron emission from semiconductors and insulators: Models and measurements," *Phys. Rev B, Codens. Matter* **19**(6), 3004-3021 (1979).
 4. J.A. Cochrane and R.F. Thumwood, "The effects of high electric fields on photocathodes," *Advances in Electronics and Electron Physics* **40A**, 441-449 (1976).

Analyzing an Array of Diamond Photodetector Detectors

Nathaniel Gindele

Analyzing an Array of Diamond Photoconductor Devices

Nathaniel C. Gindele

Advisor: James P. Knauer

Laboratory for Laser Energetics
University of Rochester

Summer High School Research Program
2003

Abstract:

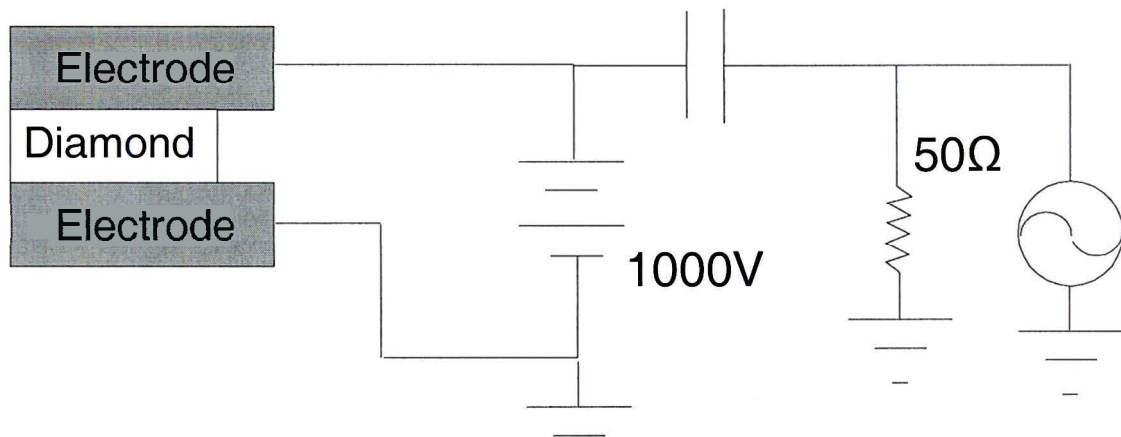
Diamond photoconductor device (PCD) detectors are used to measure X rays emitted by the implosion of a target within the target chamber. The temporal profile of the X-ray emission is encoded in the voltage signal from a PCD by the response function of this detector. Recovering the time dependence of the x rays requires deconvolving the diagnostic response from the measured signal using mathematical transforms. Before this process can occur, the noise from the signals must be reduced. Two methods of function approximation have provided the best results. One method uses the Hermite series of orthogonal polynomials, and the other method uses a Gaussian function that has been convolved with two separate exponential functions. In addition to the deconvolution problem, other tasks involving the PCD detectors were carried out. A backup array holder had to be fashioned with slight modifications added, and the apertures inside the PCD detector were all verified to be in their proper position. With those measurements, calculations were made to find the field of view of the photo array.

Introduction to Inertial Confinement Fusion:

Inertial confinement fusion is a study that hopes to efficiently carry out fusion reactions using extreme forces. By compressing a small target of deuterium and tritium with many laser beams, the pellet will reach the high pressures and temperatures required for fusion. The outer portion of the target expands outward, while the core of the target pushes inward. Both of these processes emit X rays outward from the pellet. Various X-ray detectors mounted on the target chamber receive the signal from the shot. The X rays then are used to analyze the dynamics of the shot.

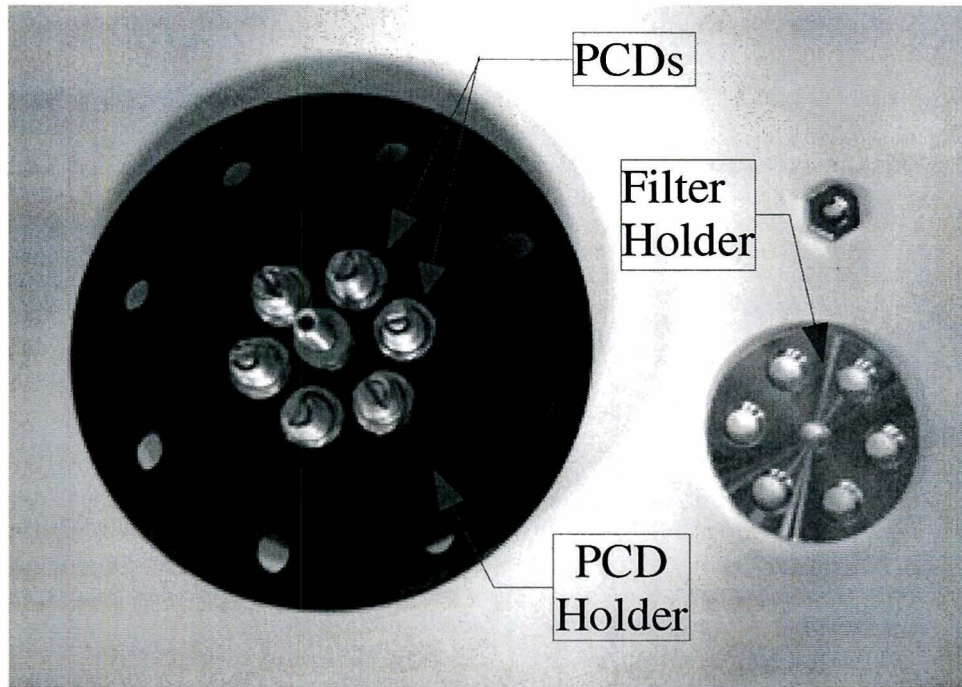
Introduction to Diamond Photoconductor Devices:

Diamond Photoconductor Devices (also referred to as Diamond PCDs) are used to measure the intensity of X rays. Diamond has a unique photoelectric property that it responds to X rays but not the ultraviolet rays used by the Omega laser. This characteristic works to eliminate a lot of the interference that other X-ray detectors have. The diamond, that receives the radiation, is located between two electrodes. This makes the PCD behave like a capacitor. Below is a diagram of the Diamond PCDs in circuit.



A photocalorimeter on the Omega laser uses six PCDs to record information about the emission of X rays from the target. This instrument uses a series of apertures to block the stray X rays and focus on the X rays that were emitted by the target.

Building a PCD holder:



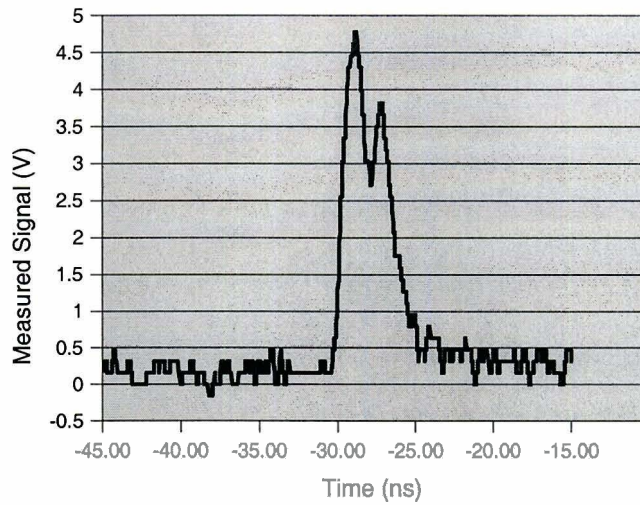
New PCDs are going to be used on the photocalorimeter. These new detectors are significantly smaller than their predecessors. To adapt to this change, a new PCD holder and PCD filter holder needed to be fashioned. With the PCD holder and filter holder closer together than before, a way of mounting one onto the other had to be developed. To solve this problem a small screw tapped post was placed at the center of the holder. The filter holder was modified as well. The old radius to the center of the holes was half of an inch and was enlarged to a full inch.

Calculating a Field of View:

The photocalorimeter's set of four apertures (including the filter holder) is uniquely designed for the current PCD arrangement. However, new PCDs and other possible modifications could cause the apertures to block out some of the X-ray signal, thus decreasing the accuracy of the instrument. Solving this problem requires precise measurements of the position of the apertures as well as verification of the aperture sizes. Using the measurements, it has been calculated that the current arrangement allows for an infinitesimally small object to be seen 20.3cm behind and 54.6cm in front of the actual target position. It was also found that the new, smaller PCD would be able to view the entire target and still have ample leeway for future modifications.

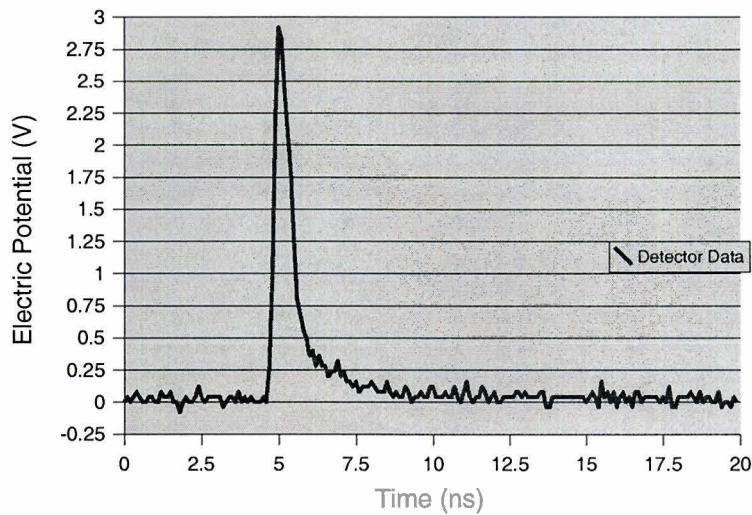
Analyzing Data from a PCD:

PCDs do not measure the X-ray signals perfectly. The devices behave similar to a capacitor in its circuit, and have two separated metal diodes. Theoretically, a capacitor will discharge its voltage in an exponential fashion. When looking at a graph of the response from a diamond PCD, there should be two separate pulses (the first pulse from the outer shell emission and the second pulse from the implosion of the core of the target), one convolved pulse is produced, as in the graph below from PCD 2 on shot 21578.

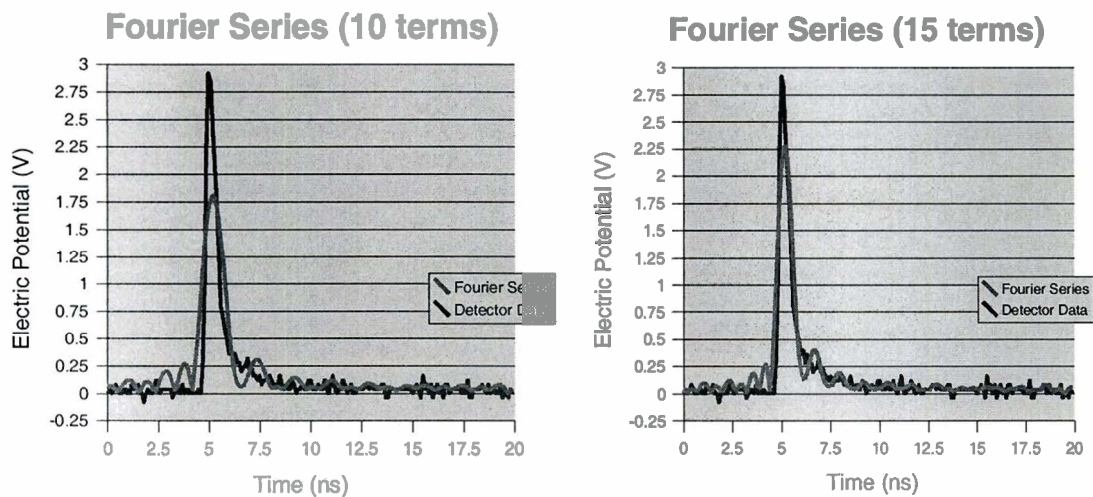


Shots 27260 and 27261 were used to measure the response function of the diamond PCDs. This response function will enable us to deconvolve the signals received from the detectors. These shots used a 100 ps pulse directed at a solid gold sphere, where there was no implosion. The readings from these shots show how an X-ray signal, similar to a delta function, is distorted. Below is the raw data from PCD 2 on shot 27261.

Unfiltered Detector Data



The first step in returning the PCD data back to the actual X-ray signal is to eliminate the noise in the response function, which would be amplified in the deconvolution process. To do this, a model of the response function was needed. The first method to accomplish this was using a Fourier series. A Fourier transform was taken on the data for the response function, and only the lower frequencies were kept. Those frequencies were then inverse Fourier transformed into a smoothed response function. This process yielded very poor results.

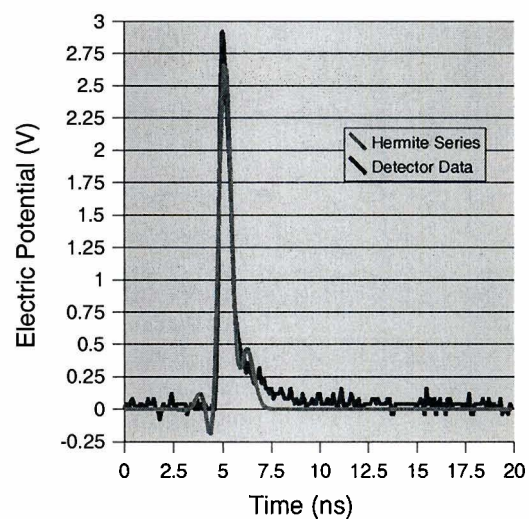
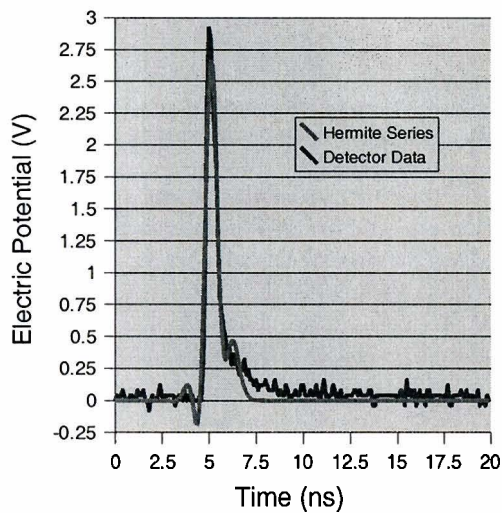


As the number of terms in the Fourier series increases the peaks are more closely approximated. However, the peaks of the data set were not closely modeled at any of the different term levels. The modeled functions also oscillated heavily at either side of the pulses.

The second model for the function was derived using the Hermite series of orthogonal polynomials. This series was chosen for this process because it had the weighting function of a Gaussian (in this case $e^{-(x^2)/2}$). The noise of the function in

relation to the functional value of true response is lowest at the peak of the data and highest at the ends. Because the Hermite series has a built in weighting function, the values at the peak will be closely followed and the noise at the base will be ignored. The Fourier series is lacking a weighting function of this kind. The results from this decomposition were vastly better than those of the Fourier series.

Hermite Polynomial Series (5 terms) Hermite Polynomial Series (15 terms)

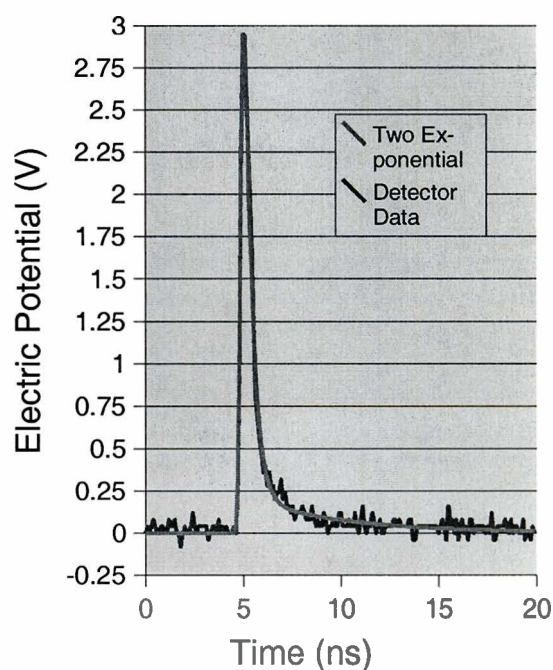
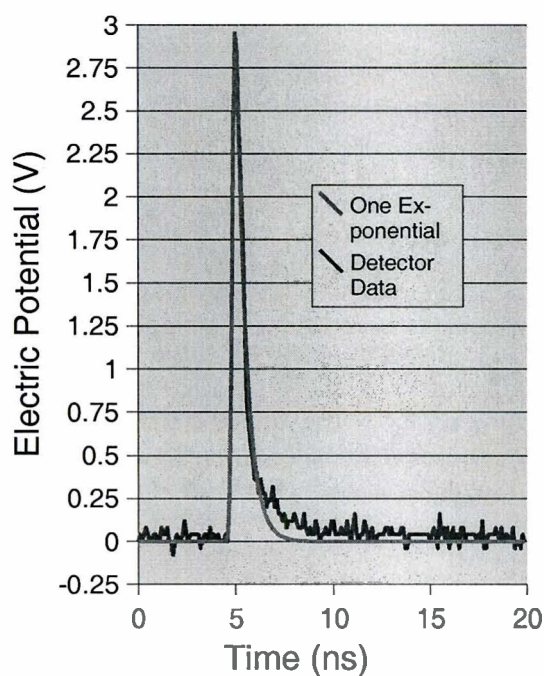


These graphs show that as the term number increases the precision of the approximation on the pulse increases. With too many terms, the area of the curve to the right of the pulse does not follow the nature of the curve.

The best representation of the data was created by using a model for the detector that fits an exponential function convolved with a Gaussian function. The PCDs work like capacitors in circuits, which discharge energy in an exponential fashion. The convolution integral was solved for the Gaussian and the exponential, and fitted to the data using the nonlinear least squares (NLINLSQ) function in PV Wave. The NLINLSQ

function evaluates a number of permutations of the function with slight changes made to the different input variable. The function returns the model that creates the smallest value for the sum of the squared differences between the representation and the data. For further accuracy, instead of using a single exponential in the function, a double exponential was used. This provided the best results of any model.

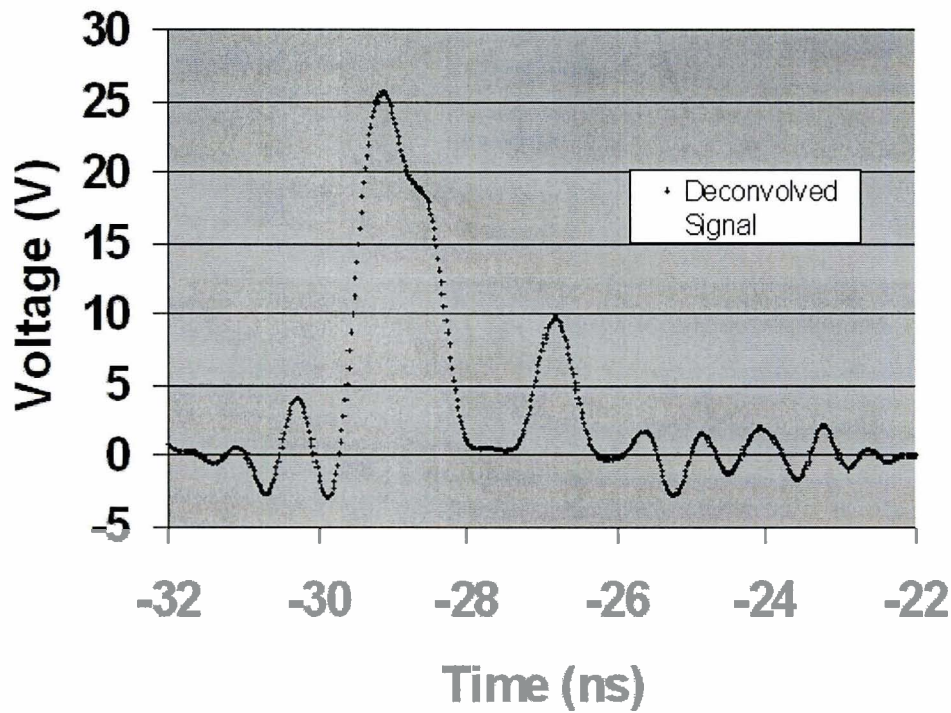
One Exponential-Gaussian Convolution Two Exponential-Gaussian Convolution



Both of these graphs approximate the peaks of the data with good precision. The single exponential does not follow the tail of the data, while the double exponential is a close approximation at almost every point.

Deconvolution:

The response function has been modeled to a high degree of accuracy and can now be used to determine the X-ray signal from a PCD. First, the quotient of the Fourier transform of the data from the detector and the Fourier transform of the response function is found. If the response function had not been modeled, the noise from that data would have been amplified by the Fourier transforms, leaving little useful data. Even so, the new data's noise will cause the high frequencies of the Fourier transform to distort the result. To deal with this problem a Weiner filter is used to eliminate the high frequencies. After the filter is employed the product is inverse Fourier transformed into the final signal seen below.



The result differs from the input data because it contains two distinct pulses, which is what really happens in the target chamber. Oscillations are seen at either side of these pulses. The oscillations are caused by the filter used in the process, which eliminates all of the high frequencies of the Fourier transform.

Conclusion:

The x-ray emission of the target explosion and implosion is hidden in the response function of the PCD device. To lower the noise in the response function, different processes of function approximation were tested. In the end, a double exponential convolved with a Gaussian yielded the best results. With this function the x-ray emission can be lifted from the voltages recorded from the detector. The photocalorimeter has a new PCD holder and filter holder to adapt itself to the new style PCD.

Acknowledgments:

I would first like to thank Dr. James Knauer for all of the time and effort he has devoted towards this project. I would also like to thank Dr. R. Stephen Craxton and the Laboratory for Laser Energetics for allowing me to participate in this unique and exciting program. The summer research program has been an invaluable learning experience that I would recommend to any student interested in the sciences.

Tuning Multiple Triplers Using a UV Spectrometer

Rohan Kekre

Tuning Multiple Triplers Using a UV Spectrometer

Rohan Kekre

McQuaid Jesuit High School
Rochester, NY

Advisor: Dr. R. S. Craxton
Senior Scientist

Laboratory for Laser Energetics
University of Rochester
Rochester, NY

Tuning Multiple Triplers Using a UV Spectrometer

Rohan Kekre
McQuaid Jesuit High School

Advisor: Dr. R. S. Craxton

To achieve nuclear fusion using glass laser systems, broadband infrared laser beams must be converted to the ultraviolet using a series of crystals. The tuning angles of these crystals, especially the “triplers”, are of paramount importance to their conversion efficiency. Given the measured UV spectrum of a laser beam, I developed a systematic method to determine how to adjust each of the tripler angles to obtain optimal conversion efficiency. This method will be implemented on the two-tripler OMEGA system in Rochester, NY. It also removes a major obstacle to an extension of OMEGA to a four-tripler system.

Tuning Multiple Triplers Using a UV Spectrometer

1. Background

1.1. Inertial Confinement Fusion

One among many research institutions worldwide investigating laser-induced inertial confinement fusion (ICF) is the University of Rochester Laboratory for Laser Energetics (LLE) [1]. In its OMEGA laser system, LLE researchers use a spherical target. This target is a plastic shell one millimeter in diameter containing a frozen layer of deuterium and tritium that is 0.1 mm thick. The 60 beams in the system transfer extremely high amounts of energy to this target, ionizing the atoms of the shell and thus creating a dense plasma layer around the fuel. As the plasma is heated, it expands outwards at approximately 1,000 kilometers per second, freeing itself from the rest of the pellet. In accordance with Newton's Third Law – every reaction has an equal and opposite reaction – the pellet implodes to a radius 20-30 times as small as that of the original pellet [1]. The imploded pellet is now under conditions of extremely high temperature and pressure; the combination of the two causes the deuterium and tritium to fuse, releasing high-energy neutrons. The ultimate hope of LLE researchers as well as many others in the scientific community is that laser-induced ICF will produce more energy from fusion than is input through laser energy; in doing so, a tremendous new energy source would be available.

The neodymium-doped glass amplifiers present in OMEGA and other laser systems produce beams with an infrared frequency (wavelength of 1.053 μm). Upon directing these infrared beams on the pellet, however, researchers in the late 1970s noticed that less than half of the energy emitted by the lasers was absorbed by the pellet. Moreover, a significant portion of the energy absorbed by the pellet was carried away by suprathermal electrons, which pass freely

through the pellet and heat the fuel before it can be compressed [1]. In doing so, they prevent the pellet from reaching the densities needed for fusion. However, researchers noticed that this problem was significantly reduced when the pellet was heated by higher-frequency laser beams. Thus, it became necessary to convert the beams from infrared to ultraviolet to achieve maximum target performance.

1.2. Frequency Conversion

Scientists at LLE currently use a series of KDP (potassium dihydrogen phosphate) crystals to convert the infrared pump to ultraviolet (see Fig. 1). Three crystals are in use in this process, termed “frequency conversion”. The “doubler” serves to double the frequency of the input wave, and two subsequent “triplers” act together to triple the original frequency. Thus, the frequency conversion currently in use on OMEGA can triple the frequency of an incoming beam when its crystals are properly oriented. Proper orientation of the crystals is very difficult to achieve and maintain; my work proposes an improved way of doing this.

The crystals operate by splitting the laser pulses into two components, one aligned with the e (extraordinary) axis of the doubler and the other aligned with the o (ordinary) axis of the

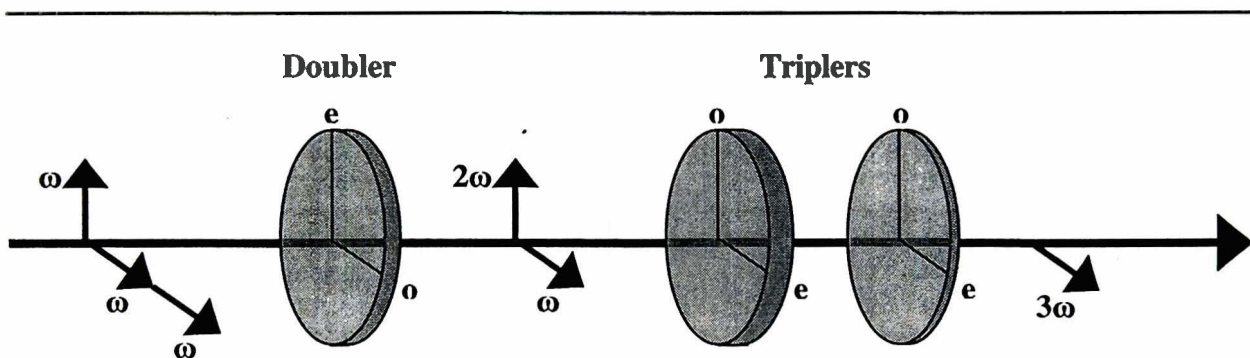


Figure 1 Frequency conversion process for a two-tripler system: an IR photon (ω) polarized in the e direction combines with two IR photons polarized in the o direction in the doubler to produce one green photon (2ω) and one o -polarized IR photon. These two combine in the triplers to produce one UV photon (3ω).

doubler [2]. When a laser pulse polarized at 35° to the doubler's o axis enters the doubler, two photons aligned with the o axis and one photon aligned with the e axis, all of which are at the original frequency (ω), are combined to produce an e -polarized photon at twice the original frequency (2ω) and an o -polarized photon at the original frequency. The 2ω photon is said to be at the second harmonic frequency and is green (wavelength of 527 nm).

Next, the laser pulse encounters the triplers, where the o and e axes are switched in orientation. The first tripler combines the second-harmonic o -polarized photon (relative to the triplers) with the first-harmonic e -polarized photon to produce one e -polarized ultraviolet photon, said to be at the third-harmonic frequency (3ω) [2]. The second tripler works on residual second-harmonic and first-harmonic photons, combining them through the process discussed above into more of the third-harmonic ultraviolet photons.

1.3. Two-Tripler vs. Four-Tripler System on OMEGA

A highly effective method introduced to improve target performance was smoothing by spectral dispersion (SSD) [3,4]. By creating smooth, focused laser beams, SSD results in a more evenly distributed, and thus more effective, contact between the beams and the target. However, to implement SSD, it is important to have the greatest range of wavelengths converted to the ultraviolet. Scientists refer to this range of wavelengths converted as “bandwidth”. Wavelengths outside this range do not convert to the ultraviolet because they are not phase-matched – that is, the component waves travel at different speeds in the crystal, causing them to move out of phase [5].

Oskoui recommended the two-tripler system to replace the previous single-tripler system on OMEGA after concluding that the conversion bandwidth would increase from 4 Å to 14 Å

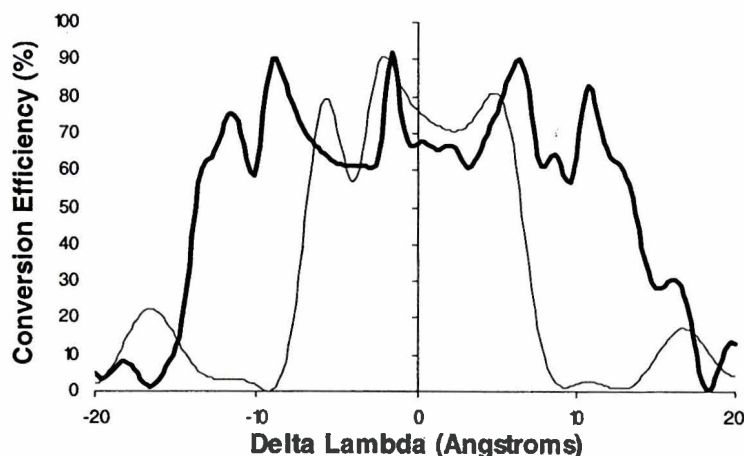


Figure 2 Comparison of conversion efficiency on two- and four-tripler systems as a function of wavelength deviations from the central IR wavelength: OMEGA's current two-tripler conversion efficiency (thin line) and the proposed four-tripler system conversion efficiency (thick solid line). The conversion bandwidth of the two-tripler system is 14 Å, as compared to the 30 Å conversion bandwidth of a four-tripler system.

[5]. A tripler was added to each of the 60 OMEGA beams following his research, resulting in the two-tripler system that exists today. Rounds concluded that an addition of two extra triplers, making four in all, would significantly broaden the conversion bandwidth to 30 Å (see Fig. 2)

[6]. Expansion to the four-tripler system would therefore improve SSD, and, in turn, target performance.

1.4. Project Goal

Critical to frequency conversion are the angles at which the crystals, especially the triplers, are tuned. External influences sometimes tilt the triplers away from their optimal angles, drastically lowering the conversion efficiency of the system. As a result, less of the beam is converted to the ultraviolet frequency, and target performance ultimately suffers.

On a two-tripler system, the tuning of the triplers is straightforward. A fairly efficient

method is currently in use on the OMEGA system to readjust detuned systems with a few shots of the laser. However, the possibility of a four-tripler system makes this tuning method unfeasible. Thus, a major obstacle to the establishment of a four-tripler system on OMEGA and similar laser systems worldwide is the lack of a means by which engineers can quickly tune the triplers to restore optimal conversion efficiency to a detuned system. This problem would be encountered as soon as the initial setup of the four-tripler system, and would surely be faced regularly thereafter.

Consequently, the goal of my project was to develop a method by which engineers could tune the proposed four-tripler system given the UV spectrum produced by the detuned system and restore the conversion efficiency to within 1% of the optimum. The successful accomplishment of this goal brings the establishment of a four-tripler system on OMEGA one step closer to realization. The method I propose also has immediate use on the current two-tripler system, as it can tune the triplers after just one shot of the laser after the new UV spectrometer is installed that will provide spectra of all 60 beams [7].

2. Methodology

2.1. Calculating the UV Spectrum

Essential to my tuning algorithm is the calculation of the UV spectrum. This three-step process is summarized in Figure 3. First, the IR spectrum is calculated. Second, the conversion efficiency is calculated. Third, the spectral power at each wavelength of the IR spectrum is multiplied by the conversion efficiency at that wavelength to obtain the spectral power of the UV spectrum. A detailed explanation of each step follows.

The first step is to calculate the IR spectrum produced by the laser. The SSD system

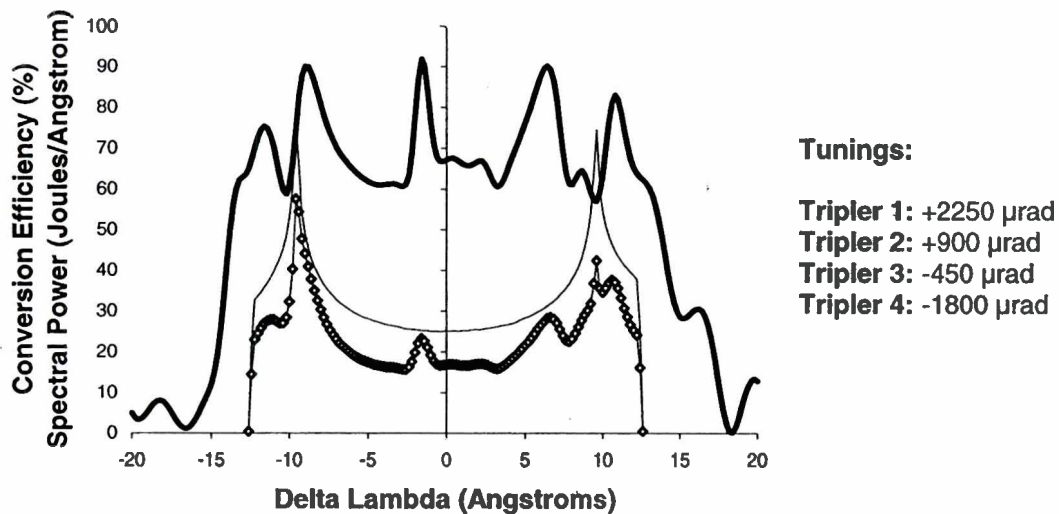


Figure 3 The proposed four-tripler system conversion efficiency (thick line), the OMEGA IR spectrum (thin line), and the optimal UV spectrum (open diamonds). At each wavelength, the UV spectral power is equal to the IR spectral power times the conversion efficiency. This spectrum is produced with the given optimal tunings.

produces a wavelength deviation ($\Delta\lambda$) across the beam [4] that varies as a function of x , y , and t , where x and y are spatial variations in the two axes of any cross-section of the beam and t is the time:

$$\Delta\lambda(x,y,t) = \Delta\lambda_1 \cos(\omega_{M1}t - \alpha_1 x + \phi_1) + \Delta\lambda_2 \cos(\omega_{M2}t - \alpha_2 y + \phi_2). \quad (1)$$

$\Delta\lambda$ is the deviation from the central IR wavelength (1.053 nm). ω_{M1} is a constant equal to $2\pi f_{M1}$, where f_{M1} is the frequency of the wave produced by the first of two electro-optic phase modulators and is equal to 3.3 GHz in OMEGA. Similarly, ω_{M2} is a constant equal to $2\pi f_{M2}$, where f_{M2} is the frequency of the wave produced by the second phase modulator and is equal to 10 GHz in OMEGA. α_1 and α_2 are constants that arise from diffraction gratings used on OMEGA to impose a sinusoidal variation of wavelength across the beam (approximately one cycle in each direction), and they are equal to 23.3 m^{-1} and 19.3 m^{-1} , respectively. ϕ_1 and ϕ_2 represent the phases of the two modulators. Since they are unknown, I set both to zero. Note that other values of ϕ_1 and ϕ_2 produce virtually the same spectra as is produced when both are set

to zero. $\Delta\lambda_1$ and $\Delta\lambda_2$ are the bandwidths imposed by the phase modulators used. For the two-tripler system, they are equal to 5.5 Å and 0.72 Å, respectively. For the four-tripler system, each value is doubled. The sum $\Delta\lambda_1 + \Delta\lambda_2$ is equal to the laser bandwidth.

The spectrum is formed by splitting the beam into 100^2 spatial cells (N_x and $N_y = 100$) at each of 150 time slices ($N_t = 150$). This produces a total of $N_x N_y N_t$ contributions to the spectrum. I also split the wavelength axis of the spectrum into 200 equal intervals.

At each cell that was within the bounds of the laser beam (within the 13.5-cm radius), I calculated the quantity:

$$\Delta\text{energy} = I\Delta x\Delta y\Delta t. \quad (2)$$

“I” corresponds to the intensity of the laser beam ($1.5 * 10^{13} \text{ W}\cdot\text{m}^{-2}\cdot\text{s}^{-1}$); Δx , Δy , and Δt are equal to the intervals for x , y , and t , respectively. After calculating $\Delta\lambda$ from Equation 1, I used a technique of linear interpolation to split up Δenergy between the two nearest bandwidth intervals according to how far the $\Delta\lambda$ value for that particular Δenergy was from each interval midpoint. By doing so, I obtained a histogram of the spectral power ($\text{J}/\text{Å}$) vs. $\Delta\lambda$. The IR spectrum was plotted using the midpoints of the bars of the histogram.

The second step in creating a UV spectrum is to determine the conversion efficiency as a function of wavelength. The conversion efficiency code of Rounds [6] (an extended version of Oskoui’s code [5]) was used. This code is based on the frequency conversion equations [2, 8]:

$$\frac{dE_1}{dz} = -1/2\gamma_1 E_1 - iK_1 E_3 E_2 \exp(-i\Delta k \cdot z), \quad (3)$$

$$\frac{dE_2}{dz} = -1/2\gamma_2 E_2 - iK_2 E_3 E_1 \exp(-i\Delta k \cdot z), \quad (4)$$

$$\frac{dE_3}{dz} = -1/2\gamma_3 E_3 - iK_3 E_1 E_2 \exp(i\Delta k \cdot z). \quad (5)$$

E_n represents the electric field of a photon at the n^{th} -harmonic frequency. The γ_n terms refer to the absorption coefficient of the waves as they pass through the crystals, but are of little significance for this experiment because only a few percent of the laser energy is absorbed. The K_n terms are nonlinear constants reflective of the material properties of the KDP crystals used. Δk , known as the wave-vector mismatch, is described below. Finally, z is the direction in which the wave travels through the crystals.

Since E_3 is the electric field of the wave at the 3rd-harmonic frequency, the growth of E_3 (described in Equation 5) is critical because it represents the creation of UV photons, the essence of frequency tripling. dE_3/dz is the rate of change in the UV electric field as the wave travels through the crystals. The product $-iK_3E_1E_2$, which is at the heart of the equation, describes the growth of the electric field; that is, the conversion of E_1 and E_2 to E_3 . Note that Equations 3 and 4 give reductions in E_1 and E_2 which produce the matching increase of energy in E_3 described here. Finally, the phase terms, as represented by $i\Delta k \cdot z$, track the difference in phases between the different waves when the crystals are detuned. Tuning angles ($\Delta\theta$) are central to Δk because of the following equation:

$$\Delta k = \frac{d\Delta k}{d\theta} \Delta\theta + \frac{d\Delta k}{d\lambda} \Delta\lambda, \quad (6)$$

where $d\Delta k/d\theta$ and $d\Delta k/d\lambda$ are properties of the KDP crystals used [8]. When Δk is zero, conversion occurs optimally as E_3 continues to grow with z . When Δk does not equal zero, conversion is reduced, and when $\Delta k \cdot z$ is π , the growth term switches signs, leading to reconversion. In Rounds' design, each crystal is tilted to a specific $\Delta\theta$ to make Δk equal to zero for a specific $\Delta\lambda$. The precise setting of $\Delta\theta$ for each tripler is the goal of this project.

The third step in creating a UV spectrum is the multiplication of the conversion efficiency at each of the wavelengths and the IR energy at these wavelengths. Thus, by inputting

the optimal tripler tunings into the Rounds-Oskoui code, I obtained the optimal UV spectrum for both two and four triplers. By comparing experimental spectra taken from detuned systems to these optimal spectra, it should be possible to diagnose how to adjust the tripler angles to restore optimal efficiency. Proposed algorithms to accomplish this are discussed in the following sections.

2.2. Bin Search for a Two-Tripler System

A detailed description of my tuning algorithm will be given for a two-tripler system, but this algorithm is easily extended to a four-tripler system as well. The first step is the “Bin Search,” illustrated in Figure 4(a). In this search, I created a grid of possibilities of detunings for the triplers. Since nearly all of the tuning errors in the OMEGA system occur well within ± 500 μrad , I chose these as the bounds of error for both triplers 1 and 2 in my Bin Search. In addition, I used an increment of 100 μrad error for both triplers. Next, I calculated the UV spectrum for each of the possible 121 combinations of error in triplers 1 and 2 (using the method described in

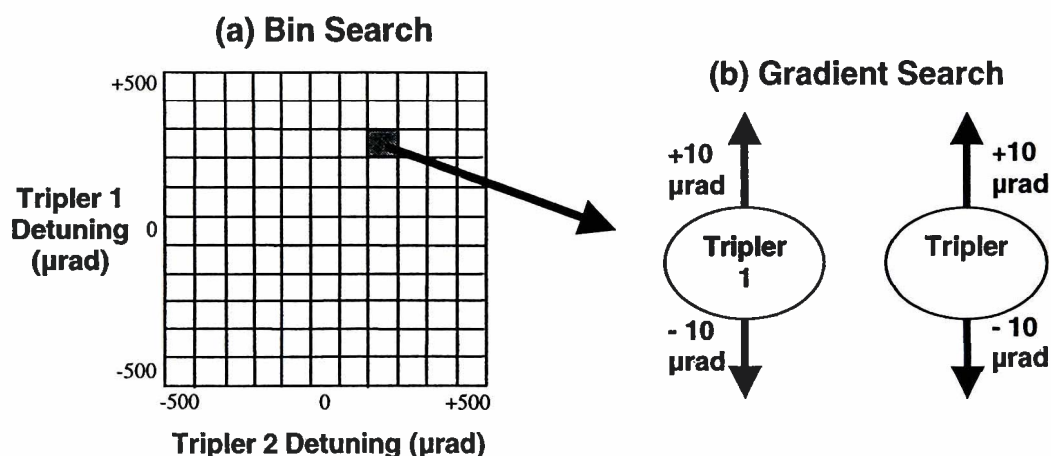


Figure 4 The tuning algorithm for two triplers: both the Bin Search and the subsequent Gradient Search try to minimize the RMS error with respect to the optimal UV spectrum. The Bin Search checks the combinations of detunings in a grid, while the Gradient Search proceeds by increasing and decreasing each tripler’s angle and evaluates the resulting RMS error.

Sec. 2.1). I compared each of these 121 UV spectra with the optimal UV spectrum by calculating the root-mean-square (RMS) difference between the two spectra. This resulted in a series of 121 RMS values corresponding to the 121 combinations of tripler error. Selecting the combination of detunings which produced the minimum RMS error, I used these detunings as the starting point of a “Gradient Search”.

2.3. Gradient Search for a Two-Tripler System

In the “Gradient Search”, the second step in my tuning algorithm and illustrated in Figure 4(b), I created four temporary scenarios by increasing and decreasing each of the two tripler detunings by $10\ \mu\text{rad}$. I then calculated the UV spectrum for each of the four scenarios, and the corresponding RMS error values with respect to the optimal spectrum. Choosing the step which produced the lowest RMS error value, I modified the calculated detunings of the system and iteratively ran the Gradient Search. I continued this process until none of the four scenarios would lower the RMS error value; at this point, the Gradient Search was complete. The detunings of the two triplers were honed to $\pm 10\ \mu\text{rad}$ at this stage, more than enough accuracy. However, I chose to further improve the accuracy to $\pm 5\ \mu\text{rad}$ by submitting the detunings I had found to a secondary Bin Search that searched through a grid with bounds of $\pm 10\ \mu\text{rad}$ and increments of $5\ \mu\text{rad}$. At the conclusion of the algorithm, detunings were found which were far more accurate than necessary to restore conversion efficiency to within 1%.

2.4. Extension to the Four-Tripler System

The algorithm for the four-tripler system is very similar. The Bin Search present in the two-tripler algorithm searched through 11^2 possible detunings; in the four-tripler algorithm, 11^4

would be prohibitive. As a result, I used two successive Bin Searches in the four-tripler algorithm. The first searches through bounds $\pm 500 \mu\text{rad}$ for all four triplers with an increment of $250 \mu\text{rad}$ for each. The second searches through bounds $\pm 200 \mu\text{rad}$ about the chosen detunings from the first Bin Search, with an increment of $100 \mu\text{rad}$. The Gradient Search is run with 8 possible scenarios, increasing and decreasing each of the four triplers by $10 \mu\text{rad}$, and at its completion the detunings of the four triplers should be accurate to within $\pm 10 \mu\text{rad}$ of their actual values. The Bin Search that narrows the detunings down to $\pm 5 \mu\text{rad}$ in the two-tripler algorithm is skipped here in the four-tripler algorithm in the interest of runtime. At the completion of the four-tripler algorithm, the conversion efficiency has been restored to well within 1%.

2.5. Comments on the Tuning Algorithm

Two comments must be made regarding the tuning algorithm. First, the bounds and increments which are chosen in the Bin Search(es) and Gradient Search for the two- and four-tripler systems are both important and deliberate. The range of $\pm 500 \mu\text{rad}$ for the primary Bin Search in the algorithm for both systems is representative of the actual tuning errors that happen in the OMEGA system. Choices of range and increments for further searches in the algorithm were chosen based on a balance of accuracy and runtime. Second, the order of the searches is critical to the algorithm. A series of Bin Searches without a Gradient Search would be impractical as runtime would be far too high. A Gradient Search without a Bin Search introduces the possibility of narrowing down to a combination of detunings that produces an RMS error with respect to the optimal spectrum that is a false or local minimum. The Bin Search must come before the Gradient Search so that a general location of the correct detuning is

established before it is narrowed further.

3. Results

3.1. Two-Tripler Trials on Computer-Generated Experiments

Ten computer-generated trials were conducted on the algorithm designed to tune a two-tripler system. They were “computer-generated” because the detuned spectrum was produced with user-entered detunings of the two triplers. The tuning algorithm was then run on the detuned UV spectrum. Detunings were in the range of $-600 \mu\text{rad}$ to $+600 \mu\text{rad}$ for each of the two triplers. These detunings were chosen outside the $\pm 500\text{-}\mu\text{rad}$ bounds of the Bin Search to test the capability of the Gradient Search to extend beyond these bounds. An example of one trial is given in Figure 5. The virtual overlap of the actual detuned spectrum and algorithm-calculated detuned spectrum is representative of all ten trials. In fact, the difference between the algorithm-derived detuning and the actual detuning was less than or equal to $6 \mu\text{rad}$ in each trial

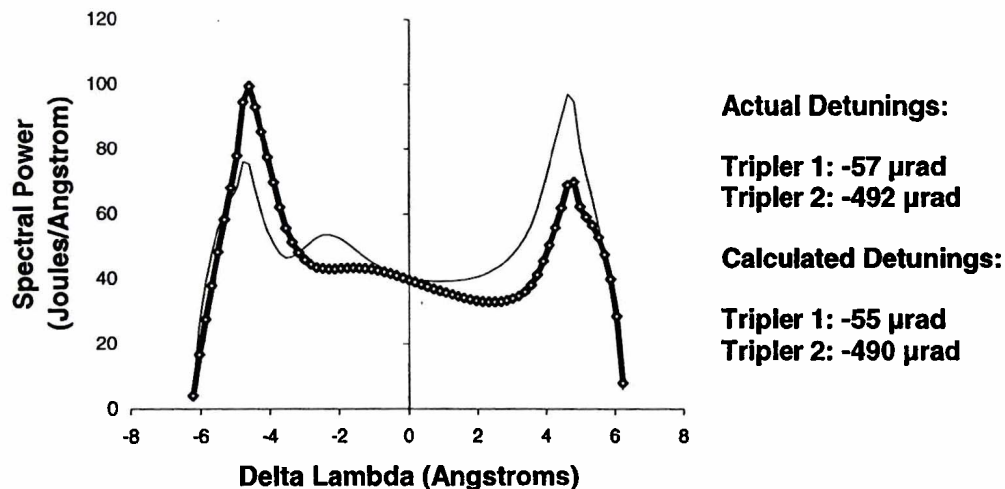


Figure 5 Trial 1 of computer-generated detunings of two triplers: the optimal UV spectrum (thin line), the actual detuned spectrum (thick line), and the detuned spectrum calculated by the algorithm (open diamonds). The accuracy of the algorithm is evident by the virtual overlap of the thick line and the diamonds.

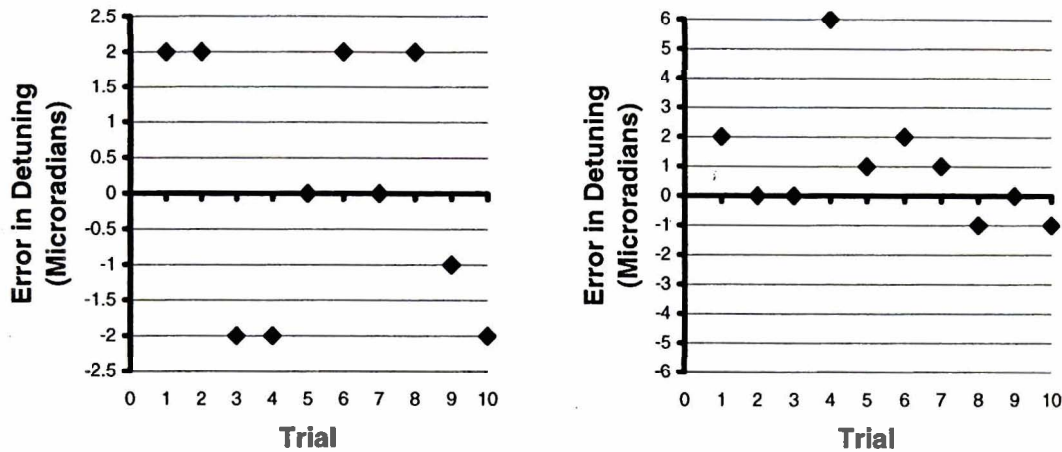


Figure 6 Algorithm errors in the detuning of triplers 1 (left) and 2 (right) for ten trials: the error for triplers 1 and 2 never exceeds $6 \mu\text{rad}$ for any of the trials. This is well within the desired restoration of conversion efficiency to within 1%.

for each tripler, as can be seen in Figure 6. Correspondingly, conversion efficiency was restored to well within the desired 1% in each trial.

3.2. Four-Tripler Trials on Computer-Generated Experiments

Ten computer-generated trials were also carried out on the four-tripler algorithm. Detunings were in the range $-650 \mu\text{rad}$ to $+650 \mu\text{rad}$ for each of the four triplers. The bounds of the Bin Search remained at $\pm 500 \mu\text{rad}$. The spectra of one trial, seen in Figure 7, show a virtual overlap of the actual detuned spectrum and the algorithm-calculated detuned spectrum. The difference between the algorithm-derived detuning and the actual detuning was less than $8 \mu\text{rad}$ in each trial for each tripler (see Fig. 8). Again, the conversion efficiency was restored to within 1% for each of the ten trials. Note that in all my tests, not only on four triplers but also on two triplers, I never encountered two different combinations of detunings that gave the same spectrum. The uniqueness of the structures (peaks and valleys) present in the spectra is the likely cause for this.

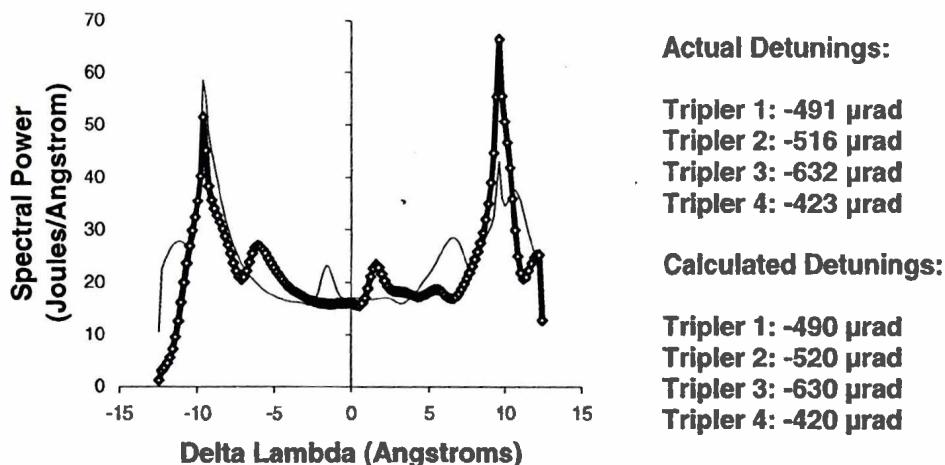


Figure 7 Trial 1 of computer-generated detunings of four triplers: the optimal UV spectrum (thin line), the actual detuned spectrum (thick line), and the detuned spectrum calculated by the algorithm (open diamonds).

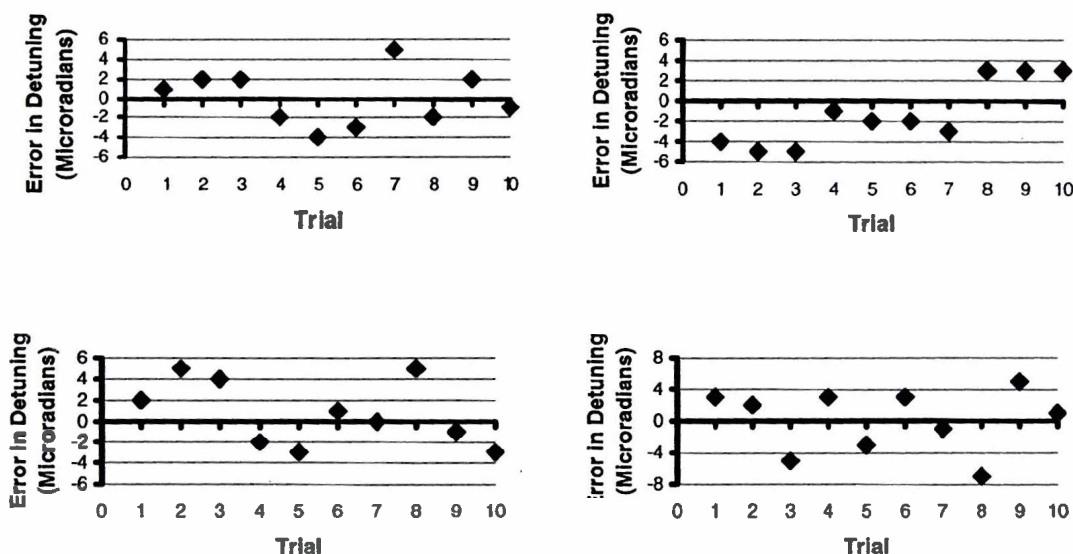


Figure 8 Algorithm errors in detunings of four triplers (triplers 1-4 arranged clockwise) for ten trials: the error for each tripler never exceeds 8 μrad for any of the trials. This is well within the desired restoration of conversion efficiency to within 1%.

3.3. Shot 28152, Beams 35 and 54

The tuning algorithm was also blind-tested on real OMEGA experimental data (for two triplers). Given the UV spectra of beams 35 and 54 on shot 28152, I used my two-tripler algorithm to calculate the detunings of the triplers in each beam. The only information I was

given beforehand was that the detuning would be no larger than 2000 μrad for either tripler (though it was later discovered that the second tripler was detuned by a much larger amount). Correspondingly, I adjusted the bounds of the Bin Search to $\pm 2000 \mu\text{rad}$. I also changed the increment of the Bin Search to 200 μrad so that the runtime would not increase drastically. The algorithm produced a calculated UV spectrum that matched the experimental UV spectrum very well, as seen in Figure 9. The algorithm error for the detuning of tripler 1 was -120 μrad in Beam 35 (Fig. 9) and -10 μrad in Beam 54. Since a 1% conversion efficiency loss corresponds to 100 μrad of detuning error, readjustment of beam 35 by the calculated amount would have restored the conversion efficiency to approximately 1% of its ideal value. Furthermore, the “actual” detunings quoted may only be accurate to 100 μrad anyway.

The detuning of tripler 2 was approximately 10 mrad, a magnitude so great that the tripler had no significant effect on the conversion efficiency and the UV spectrum. Thus, the algorithm could only find the detuning of tripler 1. Note that the detunings of both triplers were deliberately very large for testing purposes in an unrelated area. The close match for tripler 1 gives confidence that the algorithm would work very well for the smaller detuning errors that

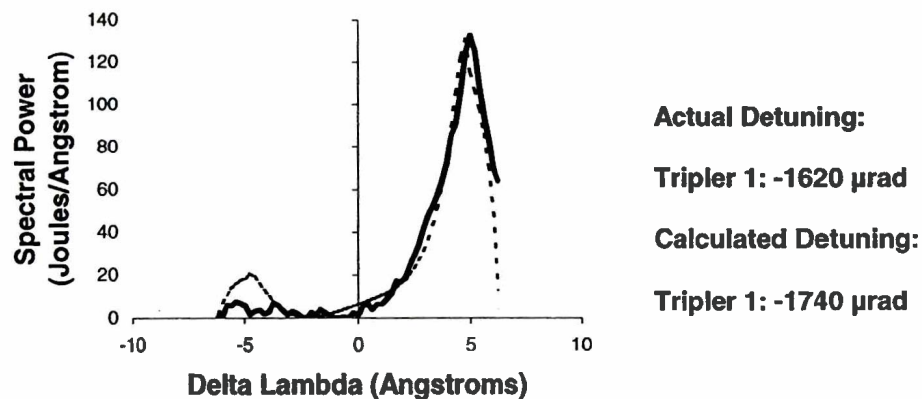


Figure 9 UV Spectra of shot 28152, beam 35: the experimental spectrum (thick solid line) and the detuned spectrum calculated by the algorithm (dashed line). Tripler 2 was detuned to such a degree that it had virtually no effect on the UV spectrum.

would normally be encountered.

3.4. Shot 30390, Beam 54

Blind experimental tests were also conducted on beam 54 of shot 30390. Again I was told that the detuning would be no larger than $2000 \mu\text{rad}$ for either tripler. Consequently, I used the same bounds and increments as I used for the trials on Shot 28152. The calculated spectrum again agreed very closely with the experimental spectrum (see Fig. 10). The algorithm-calculated detuning of tripler 1 had an error of $-45 \mu\text{rad}$, within the $100\text{-}\mu\text{rad}$ accuracy.

The error of the algorithm in tuning tripler 2 was $-320 \mu\text{rad}$. As seen in Figure 10, the spectrum produced by the “actual” tuning error – the thin line – is obviously a poor fit to the experimentally measured detuned spectrum. The excellent fit of the calculated detunings suggests that the experimental detunings were not known well. This illustrates the potential of using the spectrum as a better way of determining how the crystals are tuned than the method in use currently.

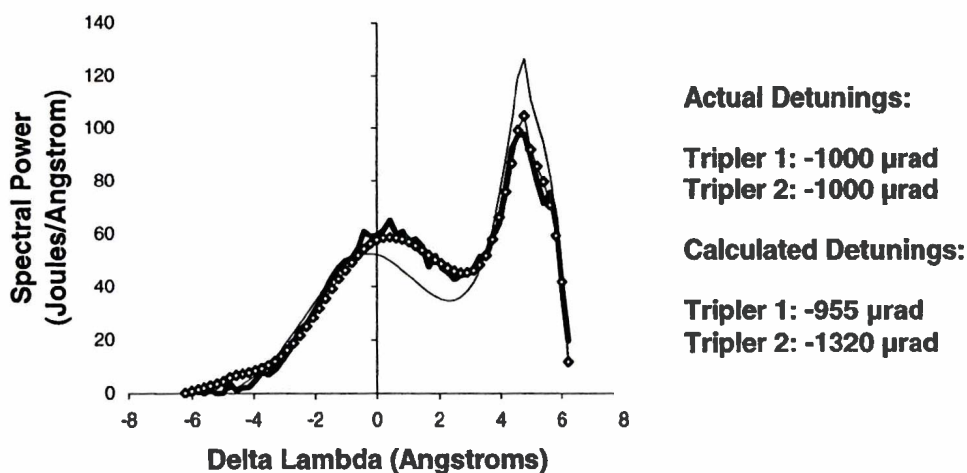


Figure 10 Tuning of shot 30390, beam 54: the experimental spectrum (thick line), the detuned spectrum calculated by the algorithm (open diamonds), and the spectrum of the given “actual” detunings (thin line).

4. Conclusions

I developed a systematic method to tune multiple triplers using the spectra produced by a UV spectrometer. Tests using computer-generated spectra proved that the algorithm works extremely well for both two- and four-tripler systems. Testing of the algorithm on experimental spectra produced spectra that matched the experimental spectra very well. Based on these results, it is planned to implement this algorithm on OMEGA when a new UV spectrometer is added that will measure the spectra of all 60 beams.

Furthermore, the outlook for tuning multiple triplers is promising. As a result, the establishment of a four-tripler system that can double the existing bandwidth is one step closer to reality at LLE as well as at other research facilities worldwide.

5. Acknowledgements

I would like to thank Dr. R. S. Craxton for allowing me to participate in the summer research program at LLE. I would also like to thank him for the invaluable guidance he has given and continues to give me with my project. I am also indebted to Dr. William Donaldson, who was and still is instrumental in my experimental testing. Finally, I would like to thank my fellow high school researchers who made the program an enjoyable, fun, and memorable experience.

6. References

1. R. S. Craxton, R. L. McCrory, J. M. Soures, "Progress in Laser Fusion," *Scientific American*, vol. 255, p. 5, Aug. 1986.
2. R. S. Craxton, "High Efficiency Frequency Tripling Schemes for High-Power Nd:Glass

- Lasers,” *IEEE Journal of Quantum Electronics*, vol. QE-17, no. 9, p. 1780, Sept. 1981.
3. S. Skupsky, R. W. Short, T. Kessler, R. S. Craxton, S. Letzring, J. M. Soures, “Improved Laser-Beam Uniformity Using the Angular Dispersion of Frequency-Modulated Light,” *Journal of Applied Physics*, vol. 66, 1989.
 4. S. Skupsky and R. S. Craxton, “Irradiation Uniformity for High-Compression Laser-Fusion Experiments,” *Physics of Plasmas*, vol. 6, no. 5, May 1999.
 5. S. Oskoui, “Broad-Bandwidth Frequency Conversion,” *1996 Summer Research Program for High School Juniors at the University of Rochester’s Laboratory for Laser Energetics*, Laboratory for Laser Energetics Report No. 277, NTIS document No. DOE/SF/19460-173 (1996).
 6. P. Rounds, “Multiple-Tripler Broad-Bandwidth Frequency Conversion for Laser Fusion,” *2002 Summer Research Program for High School Juniors at the University of Rochester’s Laboratory for Laser Energetics*, Laboratory for Laser Energetics Report No. 329, NTIS document No. DOE/SF/19460-479 (2003).
 7. W. Donaldson, R. S. Craxton, D. Jacob-Perkins, and M. Millechia, “Spectroscopy of Broadband Harmonic Generation,” *Lasers and Electro-Optical Society Annual Meeting*, Tucson, AZ, Oct. 2003.
 8. R. S. Craxton, S. D. Jacobs, J. E. Rizzo, R. Boni, “Basic Properties of KDP Related to the Frequency Conversion of 1 μm Laser Radiation,” *IEEE Journal of Quantum Electronics*, vol. QE-17, no. 9, Sept. 1981.

**Analysis of Silicon Emission in Rayleigh–Taylor Unstable Imploded
Layered Targets**

Kathryn Knowles

Analysis of Silicon Emission in Rayleigh-Taylor Unstable Imploded Layered Targets

**Kathryn Knowles
Churchville-Chili High School
Advisor: Jacques Delettrez**

**University of Rochester
Laboratory for Laser Energetics
Summer High School Research Program 2003**

1. Abstract

The Rayleigh-Taylor instability occurs at the interface between two fluids, where one fluid is significantly denser than the other and the lighter fluid is being accelerated into the heavier one. The presence of this instability affects the various processes that occur in the target during laser implosion. This instability occurs at the surface at which material is ablated by the laser in targets imploded with the OMEGA laser, and has been analyzed using post-processing files from the 2-D simulation code DRACO and various Fortran programs. The time history of the emission of radiation from a silicon-doped plastic layer placed beneath a non-doped outer plastic layer has been calculated and found to agree qualitatively with experimental results.

2. Introduction to the Rayleigh-Taylor Instability

The Rayleigh-Taylor instability is a fluid instability which can break-up the shell of an imploding inertial confinement target. It occurs when a light fluid is being accelerated into a heavy fluid. An everyday example of this instability is a container that has water and oil in it. The oil, being less dense than the water, will naturally settle in a distinct layer on top of the water. Yet when the layers are reversed, that is, when the water is placed on top of the oil, the Rayleigh-Taylor instability occurs at the interface between the two layers as they attempt to resume their

natural positions. It should be noted that if the interface between the two layers were perfectly uniform, the instability would not occur. In other words, the instability does not cause perturbations to form, but it amplifies any existing perturbations.

The same phenomenon that occurs between water and oil also occurs at the surface at which the material is ablated by the laser (the ablation surface) in targets used on OMEGA. The lighter ablated region outside the ablation surface is accelerated into the heavier solid shell by the laser (see Fig. 1). Non-uniformities in the laser beams cause tiny perturbations at the ablation surface². These perturbations grow exponentially as a result of the instability². The shapes formed by the instability are referred to as “bubbles and “spikes” (see Fig. 2). In the layered target of Fig. 1 the bubbles of CH are pushed through the CHSi layer, forcing the material to flow around them such that most of the mass is concentrated in the spikes (see Fig. 2). The CHSi then flows from the tip of the spike into the laser-heated heated plasma.

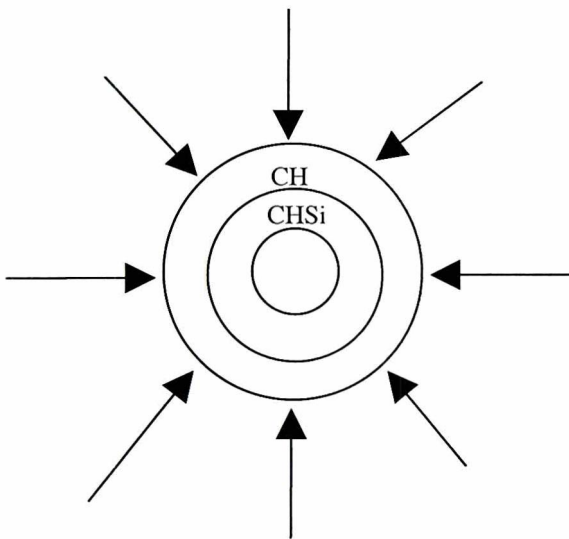


Figure 1. A schematic of the target is shown with a layer of Si-doped plastic (CHSi) surrounded by a layer of un-doped plastic (CH). The arrows indicate the directions the laser beams are coming from.

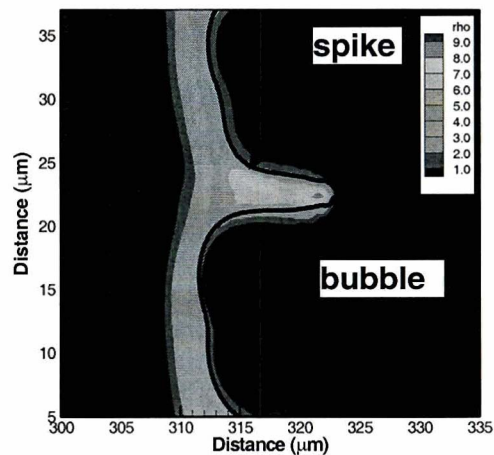


Figure 2. Density contours of part of the target shell is shown. The dark black lines indicate the shape of the CHSi layer in the target. The laser beams are incident from the right. This contour plot was generated using post-processing files from the 2-D code DRACO.

3. Introduction to Burn-through Experiments

This type of layered target is used in burn-through experiments, which are carried out to test improvements in the laser illumination uniformity. The signature layer, in this case, the CHSi layer, is used to indicate the extent of the penetration of the heat front generated by the ablation process². When the emission from the silicon ions is detected, burn-through has occurred. In other words, the outer CH layer has passed through the heat front and the CHSi layer has moved into it. The time at which burn-through occurs depends on a number of variables. The Rayleigh-Taylor instability causes the burn-through time to vary based on the uniformity of the target and the uniformity of the laser irradiation². The less uniform the irradiation, the greater the initial perturbations on the target and the faster the R-T instability will cause these perturbations to grow. Since the spikes caused by the instability are growing faster, the CHSi concentrated in these spikes will be pushed into the heat front earlier, causing an earlier burn-through time². Thus, burn-through experiments can be used to measure the uniformity of the laser².

4. Introduction to Silicon Emission

During implosion, the outside of the target is heated to extremely high temperatures. As the material is heated, it ionizes, i.e. it loses electrons. The ions of most importance in this project are the hydrogen-like silicon ions, which are silicon atoms that have lost all but one of their electrons. Emission occurs when this one remaining electron becomes excited, or when it jumps to an energy level higher than the ground state. When the electron returns to the ground state, a photon is emitted. The frequency of this photon is proportional to the energy difference of the ground state and the excited state as illustrated in the equation:

$$\Delta E = E_{excited} - E_{ground} = h\nu$$

where ν is the frequency of the photon and h is Planck's constant.

5. Calculations

The first step in calculating the silicon emission (i.e. the amount of energy released in the form of photon emission) was to determine the ion populations, particularly the population of the hydrogen-like species. This was done using the Saha equation¹:

$$\frac{N_{r+1}N_e}{N_r} = \frac{g_{r+1}g_e}{g_r} \frac{(2\pi m_e kT)^{3/2}}{h^3} e^{-x/kT}$$

where N_{r+1} , N_r , and N_e are the number densities of the $r+1$ times ionized species, the r times ionized species and the free electrons respectively, m_e is the mass of an electron, k is the Boltzmann constant, h is Planck's constant, and T is the temperature. The terms g_{r+1} , g_r , and g_e are statistical weights, or the number of possible states for the $r+1$ times ionized species, the r times ionized species, and an electron respectively. An electron can be in one of two possible states, which correspond to two different directions of spin, therefore its statistical weight is 2 or $g_e = 2$. The other two statistical terms, g_{r+1} and g_r are normally expressed as partition functions, which are infinite sums that take into account all the possible excited states for the ions. For the sake of simplicity, the excited states of the ions were ignored and only the ground states were taken into account when the statistical weights were calculated.

Solving the Saha equation for all the combinations of adjacent ion species of silicon yields a series of population ratios. If the total ion population is known, then the ratios can be used to determine the individual populations. The population of most interest is that of the hydrogen-like ion, the ion in which only one electron remains. Once this population has been determined, the

next step in calculating the emission is to determine the population of the excited state of this ion.

This is done using the equation:

$$\frac{N_{exc}}{N_{grnd}} = \frac{g_{exc}}{g_{grnd}} e^{-E_{21}/kT}$$

where N_{exc} is the number density of the excited state, N_{grnd} is the number density of the ground state, g_{exc} and g_{grnd} are the statistical weights of the excited and ground states respectively, E_{21} is the energy difference between the second principal energy level (excited state) and the first principal energy level (ground state), k is the Boltzmann constant, and T is the Kelvin temperature.

The population of the excited state can be used in the equation below to calculate the power in $\text{ergs/cm}^3\text{sec}$.

$$P_{21} = N_{exc} E_{21} A_{21}$$

E_{21} should be in ergs when used in this equation. A_{21} is the rate at which excited electrons in the second energy level return to the ground state (units are sec^{-1}). Summing all the powers (P_{21}) for a given area yields the total emission from the hydrogen-like silicon ions.

6. Results

A program was written in Fortran to perform the calculations described above. Input variables from DRACO post-processing files were used. These variables included total mass density, mass density of the CHSi, electron temperature, average ionization, and x-y variables corresponding to relative locations. These variables were used to calculate the total ion density, and the density of free electrons, values that were needed to perform the ion population calculations.

Three separate simulations were analyzed using this program. The first, shot 21133, shows that most of the emission occurs at the tips of the spikes. Figure 3 shows a contour plot of

the emission with line contours of temperatures superimposed. The 500eV isotherm goes through the areas of high emission, indicating that most of the emission occurs at this temperature. When this plot is compared to one of a uniform case taken at the same time (where the instability is nonexistent as shown in Figure 4) it is clear that no emission occurs in the uniform case because the CHSi does not become hot enough.

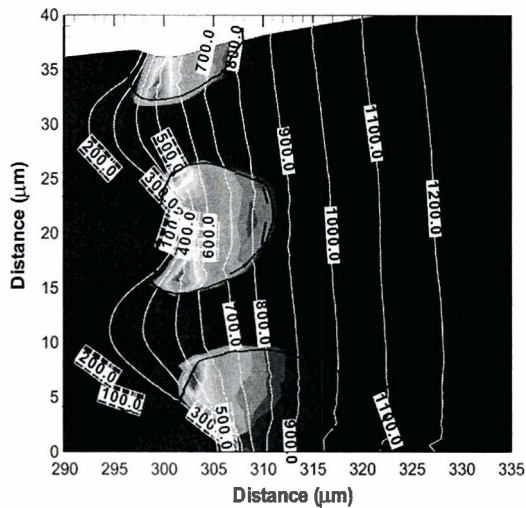


Figure 3. The shaded contours of shot 21133 show the level of emission from Si ions while the line contours superimposed over it shows the temperature in eV. The heavy black line indicates the border of the CHSi plastic layer. The laser beams are incident from the right.

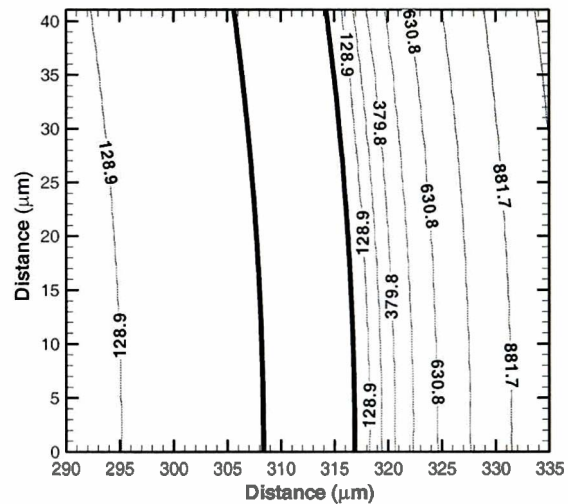


Figure 4. This temperature contour (in eV) of a uniform case illustrates that the CHSi layer (indicated by the region between the heavy black lines) does not reach the temperatures needed in order for emission to occur.

Two other simulations of actual target shots, both full quarter spheres (see Figure 6) as opposed to smaller portions of spheres, were analyzed. Shot 21144 was done without SSD, a technique of smoothing the laser beam to increase uniformity and shot 21146 was done with SSD. Figure 5 shows a graph of emission as a function of time for each of these two simulations. It is clear from the graph that emission occurs later with the more uniform illumination (dashed line). The early emission in the non-SSD case occurs because the less uniform laser beam creates larger initial perturbations in the surface of the target. These larger perturbations grow quickly due to

the R-T instability. As a result, the silicon-doped plastic is pushed into the heat front earlier than in the more uniform illumination case.

The time at which the CHSi layer burns through the CH layer can be roughly predicted using this graph as the time at which the total emission reaches one tenth of its maximum level. These two shots were part of an experiment conducted using OMEGA during which their actual burn-through times were recorded. Figure 5 shows that the predicted burn-through times qualitatively agree with the experimental burn-through times.

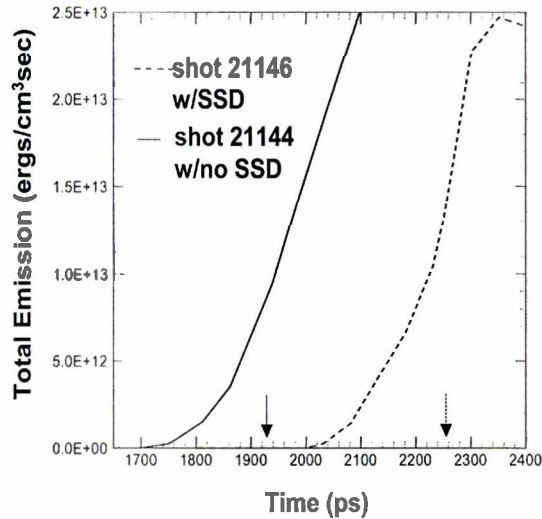


Figure 5. Total emission as a function of time is shown for a case with SSD (more uniform) and a case without SSD. The corresponding arrows indicate the times when burn-through of the CHSi layer occurred in the experimental shots.

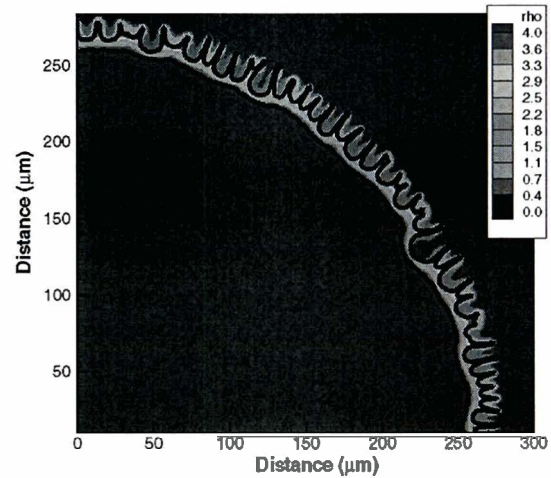


Figure 6. A density contour plot of shot 21146 with SSD.

7. Conclusion

The analysis of the DRACO post-processing files showed that the Rayleigh-Taylor instability causes the CHSi plastic layer to flow into spikes. By forcing the CHSi into the spikes, the R-T instability pushes the CHSi layer farther into the heat front of the ablation plasma causing

it to become hotter faster. As a result, most of the emission from hydrogen-like silicon ions occurs in the spikes. The analysis of data from simulations of two experimental shots (21144 and 21146) showed that more emission occurs under less uniform laser irradiation. This occurs because in less uniform targets, the instability grows faster and creates larger spikes, thus pushing more of the CHSi layer into the hot plasma and causing more emission. The results of this analysis qualitatively agreed with the actual experimental results.

8. Acknowledgements

First of all I would like to thank my supervisor, Dr. Jacques Delettrez, for guiding me through this project and teaching me almost everything I needed to know in order to complete it. I would also like to thank Dr. Reuben Epstein for taking the time to explain Saha's equation to me and showing me how to calculate the emission. His help was invaluable to the completion of this project. Finally, I thank Dr. Stephen Craxton and the Laboratory for Laser Energetics for allowing me the opportunity to work at the laser lab and to gain the experience of completing a real scientific investigation.

9. References

- ¹Clayton, Donald D. *Principles of Stellar Evolution and Nucleosynthesis*. New York: McGraw-Hill, 1968. pp 29-31.
- ²J. Delettrez, D. K. Bradley, and C. P. Verdon. *Phys. Plasmas*, Vol. 1, No. 7, 2349 (1994).
- ³Wiese, Wolfgang L., and Georgia A. Martin. "Atomic Spectroscopy." In *A Physicist's Desk Reference*. Ed. Herbert L. Anderson. National Institute of Standards and Technology, 1989.
- ⁴Pomraning, G. C. "The Interaction of the Radiation Field with Matter." In *The Equations of Radiation Hydrodynamics*. By G. C. Pomraning. New York: Pergamon Press, 1973.

⁵Craxton, R. Stephen, Robert L. McCrory and John M. Soures. "Progress in Laser Fusion."
Scientific American August 1986: 68.

Single Dye Molecule Fluorescence in Liquid Crystal Hosts

Nadine Lippa

Single Dye Molecule Fluorescence in Liquid Crystal Hosts

Nadine Lippa

BYRON-BERGEN HIGH SCHOOL
6717 West Bergen Rd.
Bergen, NY 14416

Advisors: Dr. Ansgar W. Schmid^{*)} and Dr. Svetlana G. Lukishova^{**)}

^{*)} LABORATORY FOR LASER ENERGETICS
University of Rochester
250 East River Road
Rochester, NY 14625-1299

^{**)} THE INSTITUTE OF OPTICS
University of Rochester
Rochester, NY 14627-0186

ABSTRACT

We have investigated single dye molecules embedded in liquid crystal hosts and created one prototype of an efficient room-temperature, deterministically polarized *single photon source* (SPS) *on demand* with nonclassical photon statistics (antibunching). SPS is a key hardware element in quantum information technology. Its use permits both secure communication systems based on the laws of quantum mechanics as well as extremely powerful quantum computers. We used planar-aligned *chiral* nematic (cholesteric) liquid crystal hosts for fluorescent dyes to take advantage of (1) deterministically polarized photons, and (2) excitation and fluorescence efficiency increases. We prepared 1-D photonic band gap cholesteric liquid crystal structures (both low molecular weight and Wacker oligomeric liquid crystals) doped with terrylene/rhodamine B dye molecules at exceedingly low concentration. We then performed a 532-nm, laser-induced confocal

fluorescence microscopy of the individual dye molecules in the liquid crystal hosts and measured fluorescence-photon statistics from liquid-crystal-embedded chromophores.

INTRODUCTION

The application of the project is an efficient, deterministically polarized single photon source on demand [1-3]. Single photon source (SPS) is a key hardware element for quantum information technology [4-7].

In order to produce single photons, it is necessary to excite a *single* emitter, for instance, a single dye molecule. That is why a laser beam should be tightly focused into a sample area containing a very low concentration of molecules, so that only one molecule becomes excited (Figure 1). It emits only one photon at a time: when this molecule is excited, it will remain in the excited state for a specific lifetime before emitting its own photon. Because of the lifetime, there will always be a pause between emissions of any two sequential photons. If one measures the number of second photons (coincidence events) that appear after each first photon at a definite time interval τ , the histogram should diminish to zero ordinate at $\tau = 0$ (see Figure 2). No two photons appear together at the same time. This is a manifestation of nonclassical photon statistics called *antibunching* [8-10].

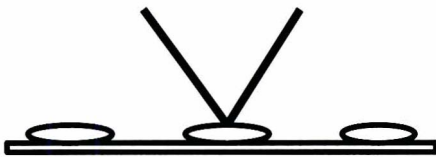


Figure 1. Excitation of one emitter by the laser beam.

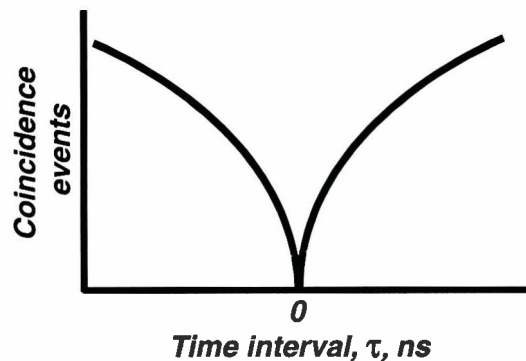


Figure 2. Explanation of antibunching.

The graph is *symmetric* relative to $\tau = 0$, because photons emitted are not labeled “first” or “second” in the emission process but become so only through the measurement. It does not matter whether a specific photon is “first” or “second”. What matters is the *delay in arrival times* (time interval) of any pair of photons .

In quantum information technology SPSs are used both for quantum cryptography (quantum communication) [4, 11-15] and for quantum computation [4-6]. In quantum communication, using SPS prevents an eavesdropper from being allowed to intercept, without the sender/receiver’s knowledge, a message with secret encryption key (Figure 3). Any e-mail message, telephone call, credit card information and other financial transaction will be safe. They will be protected by the Heisenberg uncertainty principle: if you try to measure the behavior of a quantum particle, you alter it in such a way that your measurement isn’t completely accurate. This means if you send the encryption key using *single photons*, no one can steal them without your knowledge.

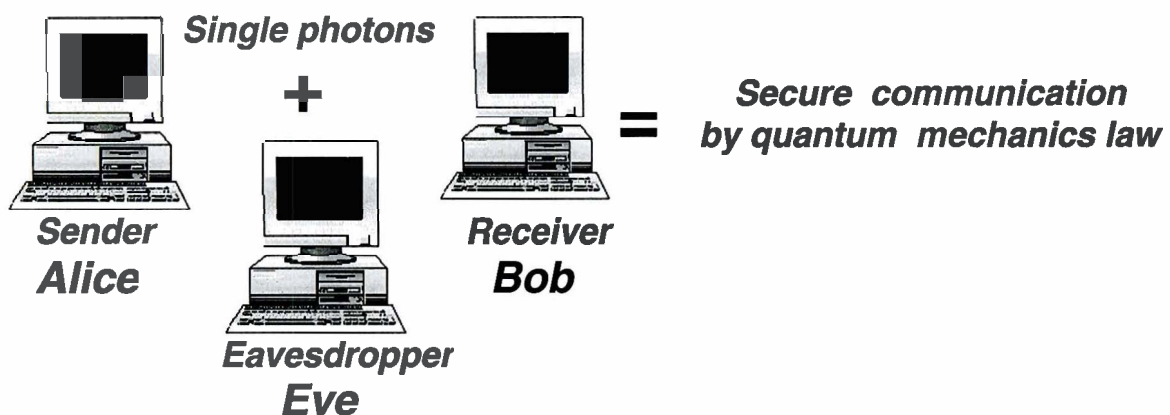


Figure 3. Quantum cryptography schematic.

Modern quantum cryptography systems are using laser pulses highly attenuated down to the single-photon level [13]. For instance, such a highly attenuated laser source is currently being applied to a cryptography system using a 67-km long, Swisscom telecommunication fiber link under Lake Geneva in Switzerland [13, 15]. However, the lack in efficiency is evident. Nine out of ten attempts to fire a photon fail with such weak laser pulses [13]. Efficient SPS realization that provides polarized single photons on demand with each pulse and with a high repetition rate is pivotal for practical quantum cryptography. In another implementation, SPS becomes the key hardware element for extremely powerful quantum computers with linear optical elements and photodetectors [16,17].

A range of solutions for SPSs is presented in the literature. SPSs have recently been demonstrated, using a variety of devices, including single molecules, single color centers in diamond, single trapped ions, and various semiconductor quantum dots, see reviews [18-20]. However, there remain significant disadvantages that hinder the establishment of a commercial product. Most SPSs, based on semiconductor heterostructures, operate at liquid helium temperature [21]. The SPS solutions that operate at room temperature, besides single dye molecule fluorescence, have emitters with long fluorescence lifetimes and they are not polarized deterministically. For instance, the single-nitrogen-vacancy (NV) center in diamond [22] has 11.6-ns lifetime in monocrystals and 23 ns in polycrystals. Dye molecules have much shorter fluorescence lifetimes, e.g., terrylene dye molecules provide a fluorescence lifetime of ~3.2-ns, preferred for high-data-rate transmission. It should be noted that single photons from most known SPSs are not polarized deterministically. It is very important for

quantum cryptography protocols and for quantum logic operations to have a deterministic polarization state of single photons.

The purpose of this study is to provide a way for an efficient, room temperature single photon source on demand with *deterministically polarized* photons. To reach this goal, liquid-crystal hosts' advantages are used to modify the properties of single-dye-molecule fluorescence. First of all, liquid-crystal technology permits one to align the nematic liquid crystal host and the embedded dye molecules in a direction preferable for maximum excitation efficiency of the dye dipole with the excitation-field electric field vector parallel to the molecular alignment axis. Deterministically aligned dye molecules will also provide deterministically polarized emission photons. In addition, 1-D photonic bandgap chiral nematic (cholesteric) liquid-crystal structures will provide up to one order of magnitude efficiency increase of the SPS [19] in comparison with other SPSs based on single-dye-molecule fluorescence [23].

This paper consists of two main parts:

- (1) material science and technology,
- (2) optical radiation science.

The material science and technology part describes planar-aligned liquid-crystal-sample preparation and doping with dye at extremely low concentration. In particular, the preparation and investigation of selective reflection properties of 1-D photonic bandgap structures in cholesteric liquid crystals will be discussed. The second, optical-radiation-science part comprises description of confocal fluorescence microscopy of single dye molecules in liquid crystal hosts and photon statistics measurements to look for antibunching.

1. MATERIAL SCIENCE PART:

PREPARATION OF 1-D PHOTONIC BANDGAP CHOLESTERIC LIQUID CRYSTAL STRUCTURES DOPED WITH SINGLE DYE MOLECULES

A photonic bandgap material is a periodic structure that totally reflects light of a certain wavelength range, prohibiting its propagation through the structure [24]. To create a photonic bandgap structure in cholesteric liquid crystal, planar alignment of cholesteric liquid crystal at the device boundaries, i.e., cell substrates, assists the self-assembly.

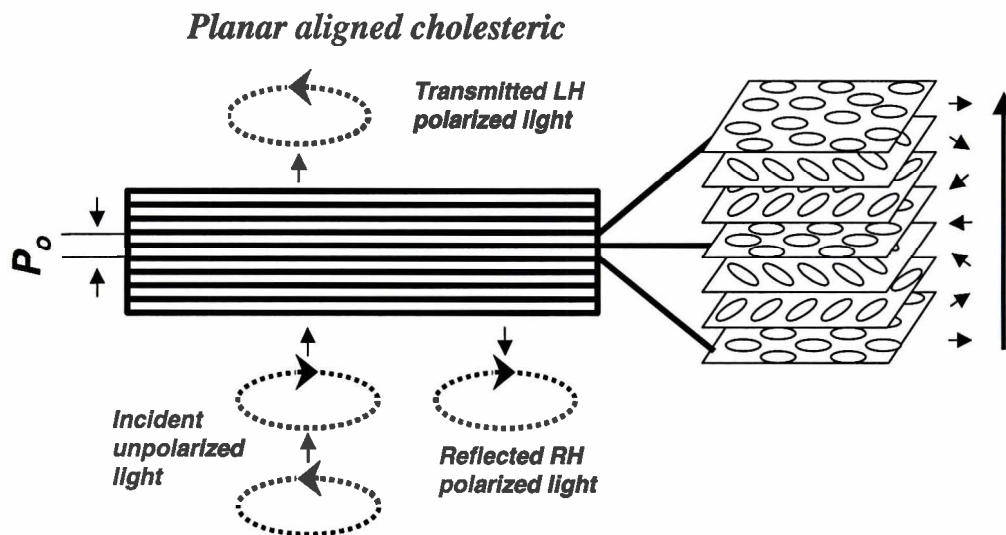


Figure 4. Cholesteric liquid crystal 1-D photonic bandgap structure schematics.

In *planar* aligned cholesterics, that for visualization purposes can be described as consisting of a periodically layered structure, the axes of the molecular director (rightmost set of arrows in Figure 4) rotate monotonically to form a periodic helical structure with pitch P_0 [25]. For such a liquid-crystal structure, the reflectance of normally incident, circularly polarized light with electric-field vector-rotation opposite to

the rotation of molecules in the helical structure (Bragg condition), approaches 100% within a band centered at

$$\lambda_0 = n_{av}P_0, \quad (1)$$

where $n_{av} = (n_e + n_o)/2$ is the average of the ordinary and extraordinary refractive indices of the medium. This is the so-called selective reflection of cholesteric liquid crystals. The bandwidth is

$$\Delta\lambda = \lambda_0\Delta n/n_{av}, \quad (2)$$

where $\Delta n = n_e - n_o$. Such a periodic structure can also be viewed as a 1-dimensional photonic crystal, with a bandgap within which propagation of light at λ_0 is forbidden. For emitters located within such a structure, the rate of spontaneous emission is suppressed within the spectral stop band and enhanced near the band edge [26]. It is this enhancement that helps the performance improvement in current SPSs.

1.1. Substrate and sample preparation for single molecule fluorescence microscopy and planar alignment of liquid crystals

Single-molecule fluorescence microscopy imposes two requirements on the samples: (1) no fluorescent *impurities* should be left on the substrates; (2) 180 and 300 μm -working distance of high N.A. objectives permits use only of samples with thickness not exceeding this value. For this reason, $\sim 170\text{-}\mu\text{m}$ -thickness glass microscopic cover slip substrates were used that both are fragile and need special care in handling. Liquid-crystal cells were fabricated in a class 1,000 liquid-crystal clean-room facility of the Optical Materials Laboratory at LLE. Ultrasonic cleaning for 60 minutes freed the 1" x 1" substrates from any dirt particles. Substrates were then rinsed in flowing, deionized

water, and dried in a stream of compressed nitrogen. After that, they were etched in piranha solution ($\text{H}_2\text{SO}_2 + \text{H}_2\text{O}_2$ in equal volume concentration) for about 20 minutes, rinsed in flowing, deionized water and dried in a stream of oil-free nitrogen (liquid-nitrogen tank boil-off).

To prepare the 1-D photonic bandgap structures, three different planar alignment procedures for liquid crystals were used: (i) substrate shearing, (ii) buffing, and (iii) photoalignment. For sheared samples, no additional substrate coatings were needed. For buffing, substrates were spin coated with either of two polymers: Nylon-6 or Polyimid. For buffing, we used a standard, velvet-surface buffing machine (see Figure 5, left). To prevent damage to the fragile substrates during the buffing procedure, cover slips were “blocked to” 1-mm-thick microscope slides with water-soluble acetate, using 40-min heating at 80°C for better results. After buffing, the cover slips were unblocked in standing, deionized water over night. This was followed by a rinse in flowing, deionized water to rid the samples of acetate traces. For photoalignment, substrates were spin-coated with Staralign 2100 from Vantico Inc. Photoalignment of coated polymer was achieved using six, UV discharge lamps with maximum wavelength ~ 302 nm (40 nm bandwidth) and a UV linear dichroic polarizer placed in a hermetic box (see Figure 5, right). The photoalignment procedure at ~ 5 mW/cm^2 power density at 302 nm lasted 10 minutes.

We used two types of liquid crystals: Wacker oligomer cholesteric-liquid-crystal powders, and low-molecular-weight E7 + CB15 (chiral additive) monomeric mixtures. For the Wacker oligomer liquid crystal powders, the samples were prepared by mixing different concentrations of two powders with individually known selective-reflection

wavelengths (vendor information). In order to obtain a desired selective-reflection wavelength mixture, mixing rules were empirically found from a set of multiple, different mixtures. To change the pitch of each mixture, powders were dissolved in methanol, mixed for 2 hours under agitation and at elevated temperature, purified through 0.45- μm particle filters, and dried from solvent under vacuum. For planar alignment, an uncoated, cleaned cover slip with a Wacker powder was placed on a hot plate and melted at 118°C. A second cover slip was used to shear the melted oligomer at temperature (and to also form the second window of the liquid-crystal cell). Slowly cooling the cell to room temperature froze in the planar alignment. For some Wacker powders, we used spin coating with polyimide and buffing of substrates. Cells with known and uniform thickness (10 –15 μm) were created by using 4 drops of a UV-cured epoxy mixed with calibrated, glass-bead spacers at the substrates' corners. After that, cells containing Wacker powder were heated into the isotropic phase and slowly cooled.

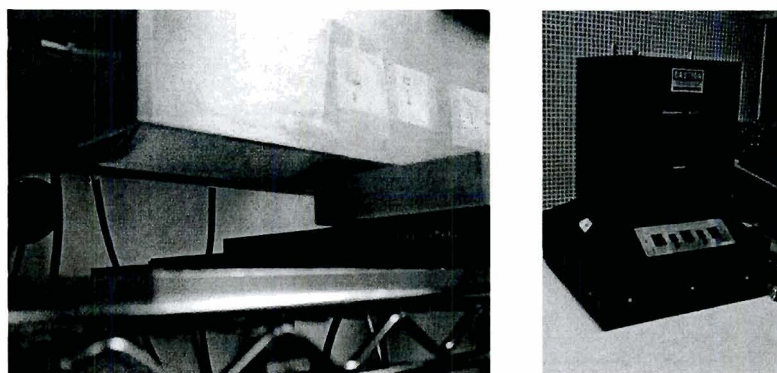


Figure 5. Buffing machine (left) and photoalignment apparatus. (right).

For low-molecular-weight liquid crystals, the coated substrate surfaces were either buffed or photoaligned. Cell thickness was again set by UV-epoxy mixed with glass-bead spacers. To find the weight concentration of the components C in a mixture of

chiral additive and nematic liquid crystal with desired selective reflection wavelength λ_0 we used a well-known relationship

$$C = n_{av}/(\lambda_0 \text{ HTP}), \quad (3)$$

where HTP is the *helical twisting power* of the chiral additive in a nematic liquid crystal. For CB15 in E7, $\text{HTP} \approx 7.3\mu\text{m}^{-1}$. An E7+CB15 liquid crystal mixture with selected concentration was fed through a 0.45- μm particle filter and a stainless-steel syringe into the assembled cell *parallel* to the polymer-alignment direction encribed in the cell walls.

Typical, prepared samples with 1-D photonic-bandgap liquid-crystal structures (both Wacker oligomers and CB15 + E7 mixtures) are depicted in Figure 6.

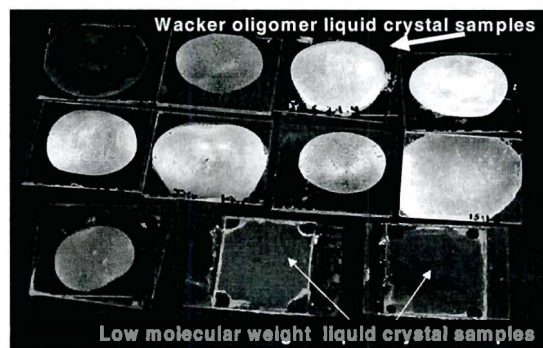


Figure 6. Prepared 1-D photonic bandgap cholesteric liquid crystal cells.

Dye dopants used were, most commonly, *terrylene*, but also *rhodamine B*. We used *terrylene* solution in methylene chloride and *rhodamine B* solution at 10^{-8} M concentration in methanol. Optimized *terrylene* concentration was found empirically by stepwise diluting the starting solution, spin coating each time a cleaned but unaligned substrate, and testing each substrate for presence of predominant single-photon-emission behavior. The final *terrylene* solution was mixed with an equal amount of liquid crystal (by volume) and dried under vacuum.

1.2. Measurements of selective reflection of the 1-D photonic bandgap cholesteric liquid crystal samples in circularly polarized light

We used a Perkin Elmer *Lambda 900* spectrophotometer to measure the wavelength response of each prepared sample, thereby determining the specific selective reflection (photonic bandgap) for each sample. A zero-order quarter wave plate and a thin-film linear polarizer were used in both spectrophotometer channels to create circularly polarized incident light of the desired handedness. Samples were tested in unpolarized, as well as in left-handed and right-handed circularly polarized incident light. Figure 7 shows transmittance of Wacker oligomer cholesteric-liquid-crystal samples versus wavelength in left-handed circularly polarized light. Two mixtures (dotted lines) exhibit a bandgap edge around 579 nm, the fluorescence maximum of terrylene dye (vertical dotted line).

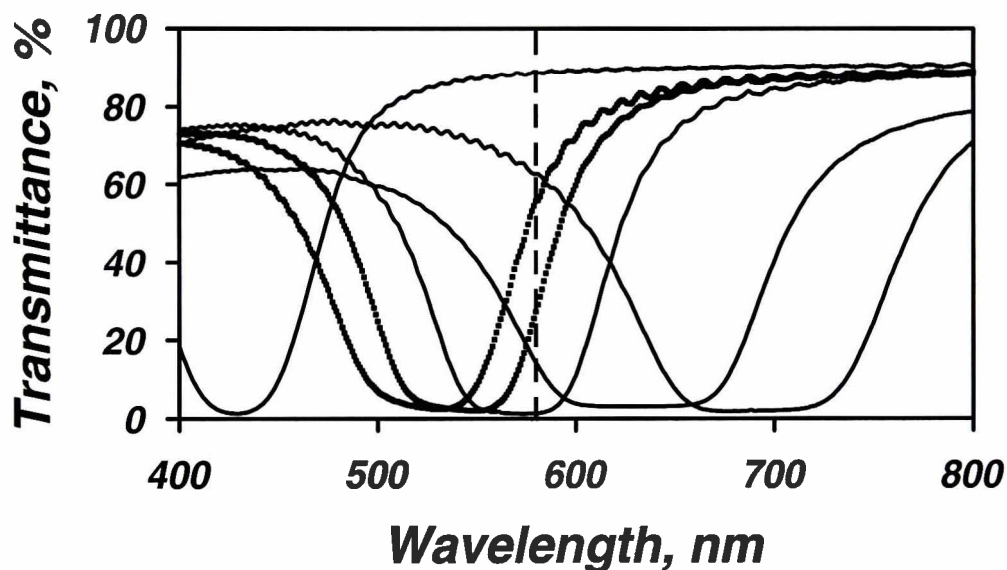


Figure 7. Transmittance curves of different Wacker oligomer 1-D photonic bandgap cholesteric liquid crystal structures. Planar alignment was made with substrates' shearing.

Similar results were achieved with the E7 + CB15 mixtures, both with buffed polyimid/nylon (Figure 8) and with photoalignment (Figure 9), in right-handed circularly polarized light (handedness strictly determined by the CB15 structure).

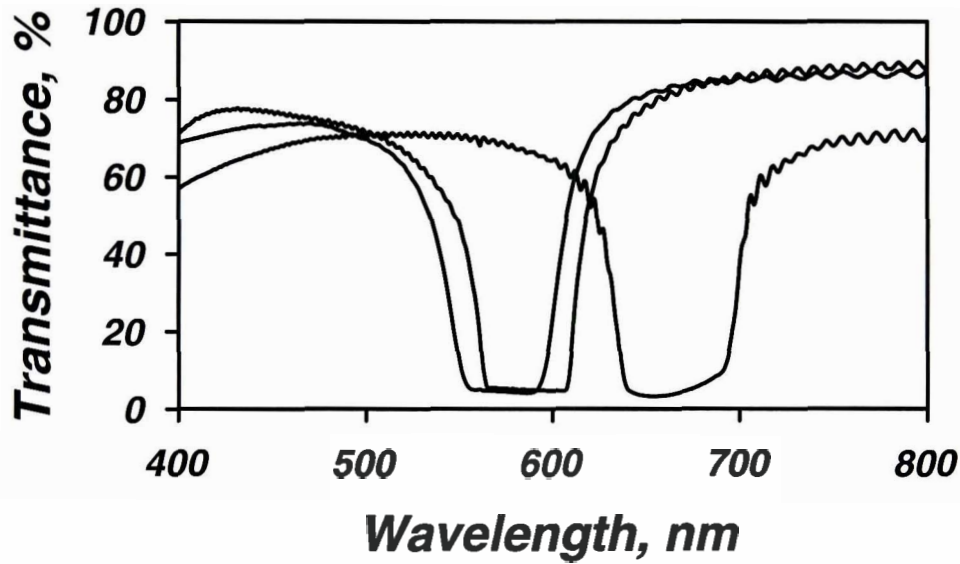


Figure 8. Transmittance curves of different E7 + CB15 mixture 1-D photonic bandgap cholesteric liquid crystal structures. Planar alignment was made with substrates' buffing.

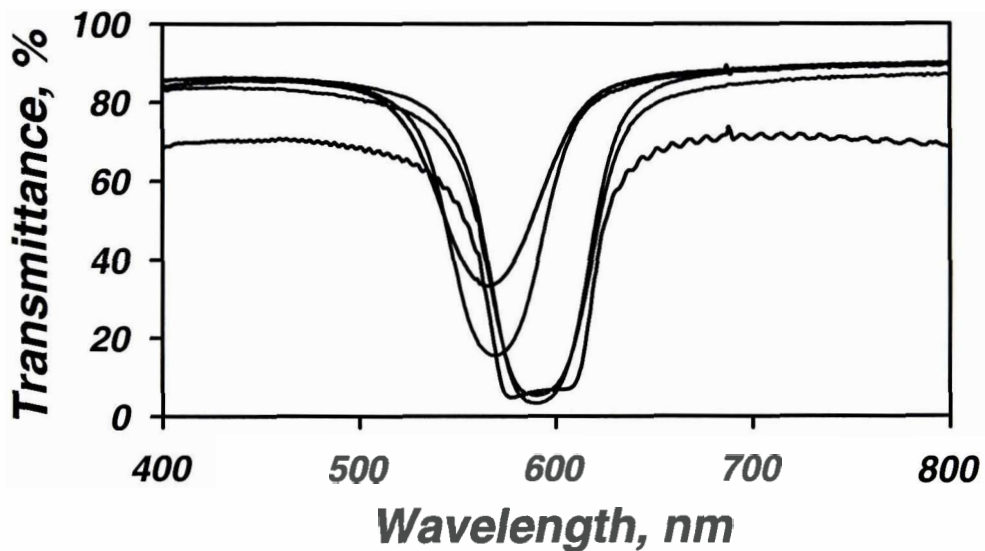


Figure 9. Transmittance curves of different E7+CB15 mixture 1-D photonic bandgap cholesteric liquid crystal structures. Planar alignment was made with photoalignment.

2. OPTICAL RADIATION SCIENCE PART: SINGLE-DYE MOLECULE FLUORESCENCE MICROSCOPY AND PHOTON STATISTICS MEASUREMENTS

2.1. Experimental setup

The experimental setup to test whether or not emission from a single emitter took place is shown in Figure 10. A 532-nm CW laser was focused by the 60x, 0.8 N. A. objective of an Alpha-SNOM confocal microscope of Witec (Figure 11) onto each doped sample. A second 100x, 1.4 N.A. infinity-corrected objective collected transmitted and emitted light contributions. Two interference filters rejected the laser light at 532-nm. A 25 μm /125 μm diameter (core/cladding) optical fiber formed the confocal aperture, and transported the light to a fiber 50:50, nonpolarizing beamsplitter of a Hanbury Brown and Twiss correlation setup [27]. Two avalanche photodiodes (Perkin Elmer SPCM-14 modules) registered the photons.

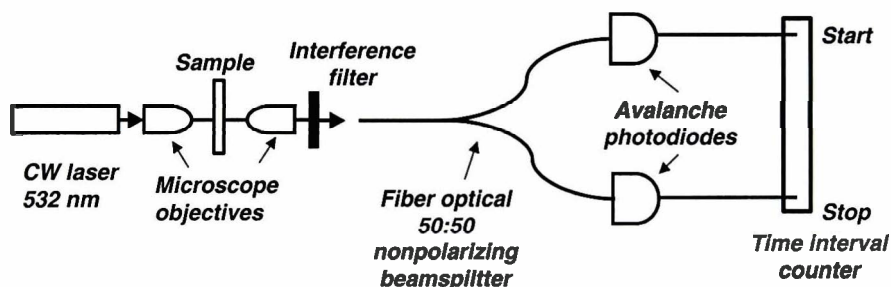


Figure 10. Experimental setup schematics for single-molecule fluorescence microscopy and photon statistics measurements.

For photon statistics measurements (see Chapter 2.3 for details), a CAMAC-based time to digital converter (Philips Scientific model 7186) controlled through the Internet or a time interval counter (Stanford Research Systems model SR620) with a pulse generator

and an oscilloscope (see Figure 12) were used to collect histograms of coincidence events.

For the purpose of observing more than one sample focal volume ($\sim 0.5 \mu\text{m}$ diameter laser beam, diffraction limit), the microscope offered a piezo-controlled stage that enabled raster scanning in the x-y directions for up to $100 \mu\text{m} \times 100 \mu\text{m}$ range. Ultimately there were two tests for single-emitter presence: (i) scanned images showing single-molecule blinking and bleaching events as well as (ii) antibunching histograms.

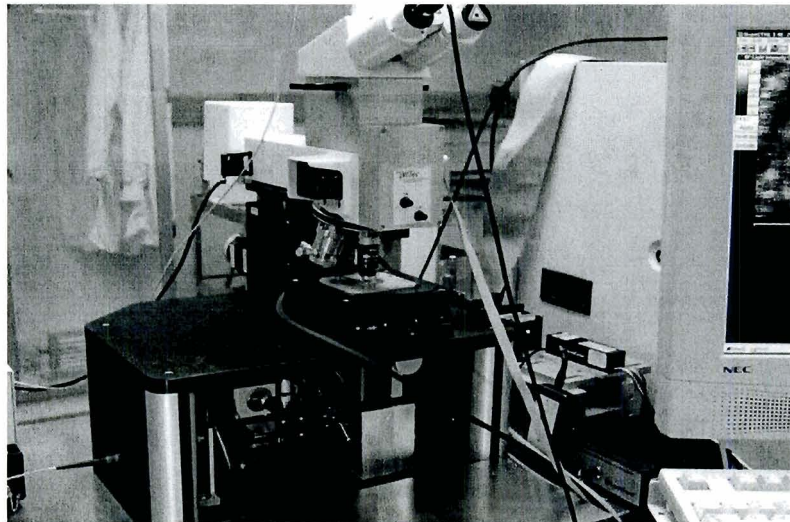


Figure 11. Photograph of the Alpha SNOM microscope.

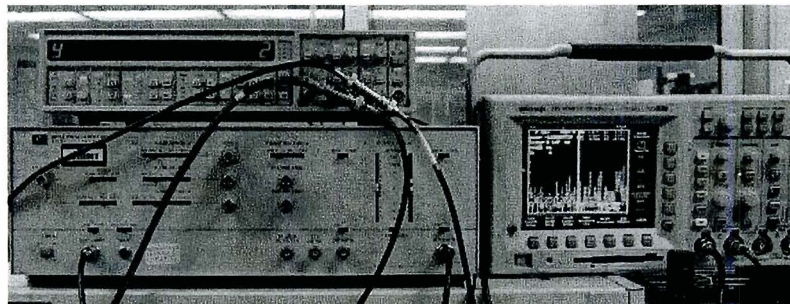


Figure 12. Equipment for photon statistics measurements: the time interval counter (top left corner) with the pulse generator (bottom left corner) and the oscilloscope with a histogram on the screen.

2.2. Experimental results on confocal fluorescence microscopy of single dye molecules

Typical fluorescence scans had dimensions of $10\ \mu\text{m} \times 10\ \mu\text{m}$, but sometimes ranged from $5\ \mu\text{m}$ to $30\ \mu\text{m}$, generally of 512×512 pixel resolution. Times taken for each of the 512 scanning lines were usually between 2.0 s and 8.0 s, producing images of varying contrast.



Figure 13. Confocal fluorescence microscopy images of single terrylene molecules ($10\ \mu\text{m} \times 10\ \mu\text{m}$ scans).

The results of confocal fluorescence microscopy of single dye molecules are visible in the images of Figure 13 obtained from Alpha SNOM. Single dye molecules are visible and show characteristic phenomena: “bleaching” and “blinking.” At the employed excitation power densities of $\sim 5\ \text{kW}/\text{cm}^2$, the finite probability for molecular dissociation in the intense photon field becomes experimentally observable. As the scan progresses, a certain number of molecules will suddenly cease emitting without ever recovering. This is generally referred to as “bleaching” (photolytic dissociation). Since no two emitters will dissociate at exactly the same moment, the observation of bleaching is accepted proof that whatever bleached was indeed a single molecule only. In addition, it was essential to assign the actual scan area a safe distance away from the laser $x = 0, y = 0$ parking position, because, with the laser at rest, massive, accumulative bleaching quickly

occurs during setup prior to the scan. “Blinking” is also evident in Figure 13. There are single lines within the molecule image that are not lit, showing that the fluorescence stopped for some time periods and later resumed, a phenomenon widely accepted as proof for the presence of single molecule fluorescence. Any two or more uncorrelated emitters would, at room temperature, not blink exactly in phase. The period of visible blinking ranges from several ms to several seconds. The detailed explanation of this long-time blinking remains controversial and subject to debate in the current literature [28].

2.3. Photon statistics measurements

Photon statistics measurements were taken with the time-to-digital converter or with the time interval counter. They detect the time interval τ between any “start” photon, which is detected by the first avalanche photodiode, and a “stop” photon, detected by the second avalanche photodiode. The time interval counter is attached to an oscilloscope for graphical presentation of the output data in a form of histogram of coincidence events versus τ . Photon statistics is defined from this histogram (Figure 14). The total number of events for time interval 1s is 10^6 , time resolution is 25 ps.

The photon-statistics measurements varied. In the group’s previous samples, antibunching was evident. In Figure 14 an absence of antibunching is encountered in recent samples, two reasons for this tend to dominate. The first is simply an overabundance of emitters, such that no single emitter is found alone, i.e., the dye concentration is still too high. Another potential contributor to polluted emission is background from impurities that the substrate-buffing process deposited. At 10 – 15 μm cell thickness, the fluorescence contributions from the substrate interfaces cannot be

completely eliminated by the confocal imaging approach. In addition, not all samples were tested yet. Because of the large amount of samples it is necessary to pursue this experiment further to attain more accurate and reliable results.

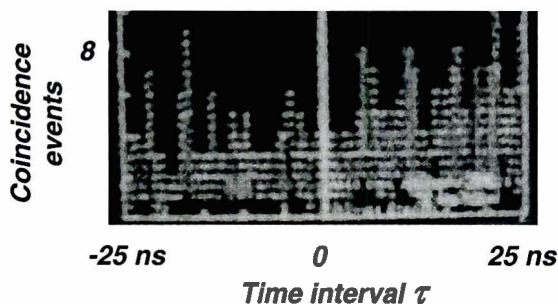


Figure 14. The photon statistics histogram of terrylene fluorescence from one of the prepared samples.

3. CONCLUSION AND FUTURE STEPS

Taken together, these results demonstrate that the cholesteric liquid-crystal system in conjunction with terrylene dopant constitutes a suitable and very promising room-temperature, single photon source. What needs to be further demonstrated, however, is the issue of high reliability emission *on demand*. This will require replacing the CW laser source used throughout this effort with a short-pulse excitation laser. Only under such excitation will it become clear whether or not single dye molecules exceed in performance the Swisscom source by emitting one and one photon only *for each excitation pulse*.

4. ACKNOWLEDGEMENTS

The author acknowledges Dr. A. Schmid and Dr. S. Lukishova for advising the project, and Dr. S. Craxton for organizing the research program. The author thanks also the Optical Materials Laboratory personnel at the LLE, especially K. Marshall and J.

Starowitz for their support and help, C. Supranowitz for the help, Prof. S. Chen's Laboratory for the loan of waveplates, and D.A. Voloschenko for consultation. Receipt of oligomer cholesteric liquid crystal powders starting material from Dr. F. Kreuzer of Wacker, Munich is also acknowledged.

Special thanks for the financial support of LLE for the summer program. The whole SPS project is supported by the U.S. Army Research Office under Award No. DAAD19-02-1-0285. Some equipment used is by the support of the U.S. Department of Energy Office of Inertial Confinement Fusion under Cooperative Agreement No. DE-FC03-92SF19460, the University of Rochester, and the New York State Energy Research and Development Authority. The support of DOE does not constitute an endorsement by DOE of the views expressed in this presentation.

REFERENCES

1. Solid state sources for single photons, www.iota.u-psud.fr/~S4P/.
2. P. Jonsson, "Generation, detection and applications of single photons", *Doctoral Dissertation*, Stockholm, Royal Inst. of Technology, 101 pp. (2002).
3. S. Benjamin, "Single photons "on demand"", *Science*, **290**, 2273-2274 (2000).
4. M. A. Nielsen and I. L. Chuang, *Quantum computation and quantum information*, Cambridge: Cambridge Univ. Press, 676 pp. (2001).
5. D. Bouwmeester, A. Ekert, A. Zeilinger, Eds., *The physics of quantum information: quantum cryptography, quantum teleportation, quantum computation*, Springer: Berlin, 314 pp. (2000).
6. The Center for Quantum Computation *Web site* (Oxford): www.qubit.org.
7. M.A. Nielsen, "Rules for a complex quantum world", *Scient. Amer.*, 67-75, Nov. (2002).

8. H.J. Kimble, M. Dagenais, L. Mandel, "Photon antibunching in resonance fluorescence", *Phys. Rev. Lett.*, **39**, 691-695 (1977).
9. D.F. Walls and G.J. Milburn, *Quantum Optics*, p.42, Springer-Verl., Berlin-NY, 351 pp. (1995).
10. U. Mets, "Antibunching and rotational diffusion in FCS", 346-359, in R. Rigler and E.S. Elson, Eds., *Fluorescence correlation spectroscopy. Theory and applications*, Springer, Berlin-NY (2001).
11. N. Gisin, G. Ribordy, W. Tittel, and H. Zbinden, "Quantum cryptography", *Rev. Mod. Phys.*, **74**, 145-195 (2002).
12. W.P. Risk and D.S. Bethune, "Quantum cryptography", *Opt. & Phot. News*, 26, July (2002).
13. A. Hart-Davis, "Can you keep a secret?" *Nature*, **418**, 270-272 (2002).
14. Company *MagiQ Technologies*, see <http://www.magiqtech.com>
15. Company *id Quantique*, see <http://www.idquantique.com>
16. E. Knill, R. Laflamme, and G.J. Milburn, "A scheme for efficient quantum computation with linear optics", *Nature*, **409**, 46-52 (2001).
17. A. Shields, "Quantum logic with light, glass and mirrors", *Science*, **297**, 1821-1822 (2002).
18. S.G. Lukishova, A.W. Schmid, A.J. McNamara, R.W. Boyd, and C. Stroud, Jr., "Demonstration of a room-temperature single-photon source for quantum information: single-dye-molecule fluorescence in a cholesteric liquid crystal host", *LLE Review*, Quarterly Report, **94**, 97-106, DOE/SF/19460-485, January – March (2003).
19. S.G. Lukishova, A.W. Schmid, A.J. McNamara, R.W. Boyd, and C. Stroud, Jr., "Room temperature single photon source: single dye molecule fluorescence in liquid crystal host", *IEEE J. Selected Topics in Quantum Electronics*, Special Issue on Quantum Internet Technologies, Nov-Dec. (2003), accepted for publication.

20. S.G. Lukishova, A.W. Schmid, C.M. Supranowitz, N. Lippa, A.J. McNamara, R.W. Boyd, and C.R. Stroud Jr., *J. Modern Optics*, Special issue on Single Photons, accepted for publication.
21. C. Santori, Fattal, D., Vuckovic, J., Solomon, G. & Yamamoto, Y. "Indistinguishable photons from a single-photon source," *Nature*, **419**, 594-597 (2002).
22. C. Kurtsiefer, S. Mayer, P. Zarda, H. Weinfurter, "Stable solid-state source of single photons", *Phys. Rev. Lett.*, **85**, 290-293 (2000).
23. B. Lounis and W.E. Moerner, "Single photons on demand from a single molecules at room temperature", *Nature*, **407**, 491-493 (2000).
24. E. Yablonovitch, "Inhibited spontaneous emission in solid-state physics and electronics", *Phys. Rev. Lett.*, **58**, 2059-2062 (1987).
25. S. Chandrasekhar, *Liquid Crystals*, Cambridge: Cambridge Univ. Press (1977).
26. V.P. Kopp, B. Fan, H.K.M. Vithana and A.Z. Genack, "Low threshold lasing at the edge of a photonic stop band in cholesteric liquid crystals", *Opt. Lett.*, **23**, 1707-1709 (1998).
27. R. Hanbury Brown, R.Q. Twiss, "Correlation between photons in two coherent beams of light, *Nature*, **177**, 27-29 (1956).
28. F. Vargas, O. Hollricher, O. Marti, G. de Schaetzen, G. Tarrach, "Influence of protective layers on the blinking of fluorescent single-molecules observed by confocal microscopy and scanning near field optical microscopy", *J. Chem. Phys.*, **117**, 866-871 (2002).

**Development of Weighted Chirality Indices: Their Use in Modeling Nickel
Dithiolene Systems**

Anthony Noto

***Development of Weighted Chirality Indices:
Their Use in Modeling Nickel Dithiolene Systems***

Anthony Gerald Noto
Greece Athena High School
Advisor: Mr. Kenneth Marshall

ABSTRACT

Weighed, scaled chirality indices have been calculated for a group of chiral nickel dithiolene dyes based on an intrinsic molecular chirality tensor. To improve the accuracy of the index, each atom in a given molecule was weighted according to its atomic mass. The index was scaled to allow comparison of molecules with different atom counts. Assigning weights can reduce the effect of lighter elements on the chirality index while preserving the general trend of the index. This method permits the relationship between individual atoms and the chirality index to be better modeled. The results for chiral nickel dithiolene dyes, a relatively rigid system of molecules, show an increase in the chirality index when the chiral centers are in close proximity to one another. The most promising dyes of this class reach their maximum chirality index when their carbon spacers are three atoms long.

I. INTRODUCTION

Since Louis Pasteur's discovery of molecular chirality in 1848¹, scientists have mainly classified chiral molecules qualitatively, in terms of their absolute configuration or the direction in which they rotate the plane of polarized light. A chiral molecule is classified as being in a *sinister* (S) or *rectus* (R) configuration. It is also classified as positive or negative according to the direction that polarized light is rotated. There is no definite correlation between the two classification systems. Recently, scientists have taken an interest in representing chirality quantitatively. A quantitative measurement of chirality could be used in applications ranging from pharmacology to the prediction of optical properties.

The main application for chiral molecules is found in the pharmaceutical industry. The action of certain chiral drugs depends on the configuration. For example, one chiral form of Ritalin is pharmacologically active, while its mirror image form is not. One chiral form of thalidomide can prevent nausea, while its mirror image form can cause birth defects. The use of chiral drugs in pharmacology can also cause a decrease in the dosage, a decrease in the likelihood of side effects and an increase in the speed of production.

Until recently, scientists were unable to accurately predict with any certainty a molecule's handedness with respect to optical rotation. Accordingly, they were also unable to predict the molecular structures that gave rise to chiral properties. Generally, chiral compounds were formed through the study of existing compounds and groups based on previous literature and intuition. This method was considered to be an educated trial and error process. To then synthesize and characterize the compound was the only way one could ascertain a molecule's chirality. However, experimentation tends to be a

very time consuming and costly process. If this step can be eliminated through the use of a theoretical chirality index, the speed at which chiral compounds can be created will increase significantly. The increase in speed of molecular design can greatly benefit the pharmaceutical industry in particular. If molecular properties can be accurately predicted through the use of this index, drugs can be developed with less cost for the consumer.

For a theoretical chirality measure to be effective it must exhibit certain properties. First, the index must be invariant under rotation and translation. Also, a sign change should be observed for the two optical isomers of a chiral molecule. To make the index meaningful it must be invariant of the molecular size, in terms of the number of atoms. Finally, an ideal index could be used to predict a desirable property that is difficult to calculate empirically.

The two main methods that are currently used to compute chirality are innately different from each other in their level of development, ease of use and efficiency. The first method, explored in 1995 by Zabrodsky and Avnir,^{2,3} attempts to find the absolute distance between the two configurations of a chiral molecule if they were to be superimposed over one another. This method is well developed and has been explored thoroughly. However, due to the multiple iterations necessary to make this value meaningful, Osipov, Pickup and Dunmar in 1995 proposed a simpler method⁴.

The chirality index proposed by Osipov *et al* follows the aforementioned conditions for an effective index far better than all previous models. Recently, Solymosi *et al* improved the chirality index by introducing a scaling factor that allows comparison between molecules with different numbers of atoms.⁵ Also, their scaled chirality index has been used to find the contributions of individual atoms and atom groups to the overall

chirality of the molecule. This scaled chirality index is useful even in its abstract form; however, preliminary work has been completed by Neal *et al*⁶ that shows a promising correlation between helical twisting power and the scaled chirality index for rigid molecules. Helical twisting power is defined as one divided by the pitch length of the chiral medium, where the pitch length is the distance needed for polarized light to rotate 360° through the medium. This correlation is valid based on the research conducted by Osipov and Kuball⁷ which lays the foundation for the relationship between circular dichroism and helical twisting power. Circular dichroism is observed when optically active matter absorbs left and right hand circular polarized light differently. Correlation to helical twisting power is important because it allows for comparison to a tangible property. Helical twisting power is used in optics for selective light reflection of circularly polarized light with a defined wavelength depending on helical pitch.

This research improves upon the scaled chirality index by introducing the atomic mass of the individual atoms into the calculation to form a weighted index. The effect of using the weighted index is illustrated for a simple chiral system. This index is then applied to a relatively new set of organometallic dyes known as nickel dithiolenes. The largest index is found when the spacers, between the core group and the terminal groups, contain three carbons, thereby identifying the most promising candidate for synthesis. The results of this experiment are explained in terms of steric factors and confirmed by modeling a hypothetical biphenyl system.

II. THE WEIGHTED, SCALED CHIRALITY INDEX

The basis for the scaled chirality index is the gyration tensor \mathbf{G} . Modifying a simple model for optical activity, Osipov *et al*⁴ created the gyration tensor which is defined as

$$\mathbf{G} = \int d\mathbf{r}_1 d\mathbf{r}_2 d\mathbf{r}_3 d\mathbf{r}_4 \rho(\mathbf{r}_1) \rho(\mathbf{r}_2) \rho(\mathbf{r}_3) \rho(\mathbf{r}_4) \times \frac{[(\mathbf{r}_{12} \times \mathbf{r}_{34}) \otimes \mathbf{r}_{14}](\mathbf{r}_{12} \cdot \mathbf{r}_{23})(\mathbf{r}_{23} \cdot \mathbf{r}_{34})}{(r_{12} r_{23} r_{34})^n r_{14}^m} \quad (2.1)$$

where $\mathbf{r}_{ij} = \mathbf{r}_i - \mathbf{r}_j$, $\hat{\mathbf{r}}_{ij} = \mathbf{r}_{ij} / r_{ij}$, m and n are arbitrary integers and ρ is the density concentration. The density concentration is a sum of weighted δ functions representing the locations of the N atoms in the molecule. The unscaled chirality index G_O is given by 1/3 the trace of the gyration tensor \mathbf{G} :

$$G_O = \frac{1}{3} \int d\mathbf{r}_1 d\mathbf{r}_2 d\mathbf{r}_3 d\mathbf{r}_4 \rho(\mathbf{r}_1) \rho(\mathbf{r}_2) \rho(\mathbf{r}_3) \rho(\mathbf{r}_4) \times \frac{[(\mathbf{r}_{12} \times \mathbf{r}_{34}) \cdot \mathbf{r}_{14}](\mathbf{r}_{12} \cdot \mathbf{r}_{23})(\mathbf{r}_{23} \cdot \mathbf{r}_{34})}{(r_{12} r_{23} r_{34})^n r_{14}^m}. \quad (2.2)$$

This chirality index is invariant of translation and rotation. If $n = 2$ and $m = 1$ the index is invariant of dilation as well. With these values of n and m the index becomes dimensionless and it is in this form that the index will be used throughout this paper. Since the chirality index G_O scales as N^4 where N is the number of atoms, a scale factor is applied to enable comparison between molecules of different atom counts. The scaled chirality index $G_{OS} = (4! / N^4) G_O$ is a more useful value. Despite its apparent usefulness, G_{OS} does not determine any measurable property such as optical rotation. It is constructed to be large for a molecule with a strong helical structure and to vanish for a

molecule with any symmetry that precludes chiral behavior. The numerical expression for the scaled chirality index is⁵

$$G_{OS} = \frac{4!}{N^4} \frac{1}{3} \left[\sum_{\substack{\text{all permutations of} \\ i, j, k, l=1}}^N w_i w_j w_k w_l \times \frac{[(\mathbf{r}_{ij} \times \mathbf{r}_{kl}) \cdot \mathbf{r}_{il}](\mathbf{r}_{ij} \cdot \mathbf{r}_{jk})(\mathbf{r}_{jk} \cdot \mathbf{r}_{kl})}{(r_{ij} r_{jk} r_{kl})^n r_{il}^m} \right] \quad (3.1)$$

where w_i , w_j , w_k , w_l are values that represent the weights of the individual atoms i thru l . While Solymosi *et al*⁵ suggested using the atomic mass as the weight, the weights have been set to 1.0 in their work and in all previous research. However this may not accurately model a real world situation since all atoms do not contribute equally to the chirality of the molecule. Substituting the atomic mass into the calculation as the weight, as first suggested by Solymosi *et al*⁵ is a viable approach. The calculations presented here are the first to use atomic mass as the weight. The effects of this substitution will be discussed further in section IV.

III. METHODS

To facilitate this research, a computer program was written using Microsoft Visual C++ 5.0. This program is used to compute the chirality index and the scaled chirality index. The program takes input in the Protein Data Bank format from data generated by many available computational chemistry modeling software packages (e.g., Hyperchem, Spartan and Mopac). The data comprises the atomic symbol, atomic number, atom number (in the molecule) and the Cartesian coordinates of the atom.

The program then allows the user to choose how the atoms will be weighted: all atoms can be given a weight of one, the program can automatically set the weight to the atomic mass, or the user can input each atom's weight individually. This allows many

types of weighting systems to be explored without changing the code. Finally, the program allows the user to enter the arbitrary integer values n and m to change the dimensionality of the index.

Currently, the computational algorithm requires a runtime of $O(N^4)$ and it can, therefore, take some time for large molecules to run on a single thread. To decrease the actual runtime, a multithreaded version was written to run 16 parallel threads on a 64-processor SGI Origin 2000 UNIX computational server. The code has been optimized and executed on computers running Microsoft Windows 2000, Microsoft Windows XP and SGI IRIX 6.5.

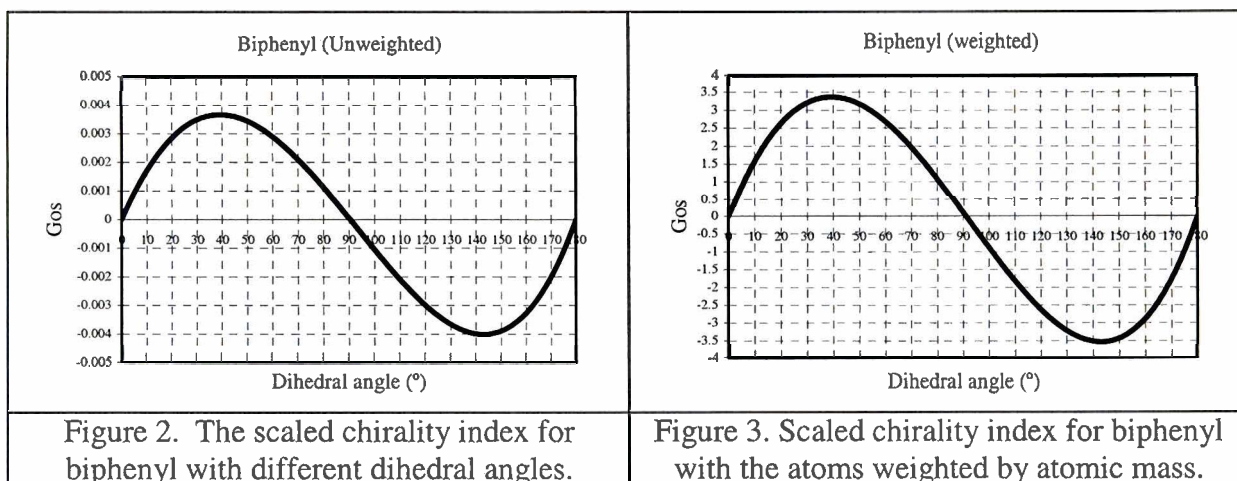
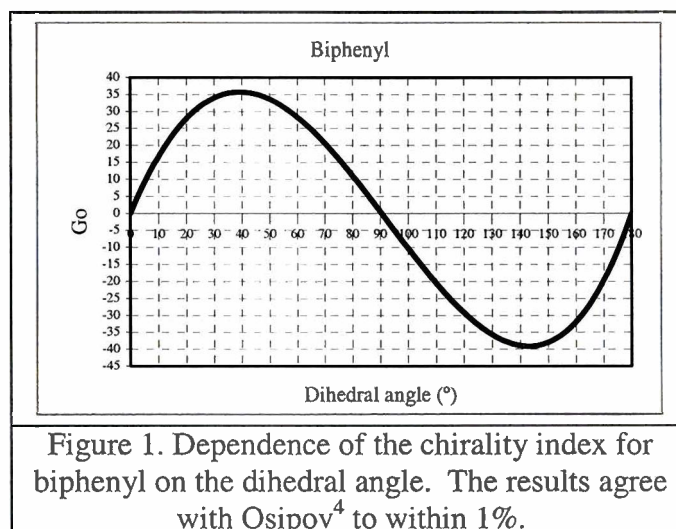
Multithreading effectively decreased the runtime to a reasonable level for average sized molecules with approximately 200 – 300 atoms. For molecules larger than 500 atoms, the algorithm is not efficient enough to finish the computation in a reasonable time of approximately one week. The algorithm will continue to be analyzed for efficiency improvements.

After the program has finished computing the indices, the results are sent to an external text file whose location is specified at the beginning of the program. The text file is formatted for easy importation into Microsoft Excel or an alternate spreadsheet program for analysis.

IV. APPLICATION TO BIPHENYL

Biphenyl was utilized previously as a test molecule for the chirality index⁴ and the scaled chirality index⁵. As in previous papers, this research used the biphenyl system with different dihedral angles between the rings as an assessment of the program's functionality and accuracy. The molecules were constructed using Hyperchem 7.1, from

Hypercube, and modeled on a Microsoft Windows 2000 Pentium 4. The molecules were then energy minimized using the MM+ force field. The MM+ force field is a basic calculation completed through Hyperchem to manipulate the molecular structure based on the interactions between atoms and bonding groups. The results are presented in Figures 1 and 2. Reassuringly, the program computed the chirality index to within two decimal places of the results attained by Osipov *et al*⁴. However, the scaled index computed by the program was approximately one third of the result attained by Solymosi *et al*⁵, although it followed the same general trend. Applying the scale factor to Osipov's chirality index should result in the scaled chirality index of Solymosi *et al*⁵.

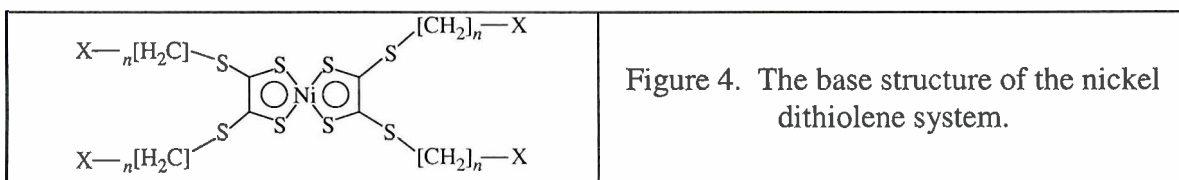


After the program was thoroughly tested using previous results, the individual atoms of the biphenyl series were weighted according to the atomic mass. The results are shown in Figure 3. The differences in trend between the weighted and un-weighted system were negligible. The y-scales were different due to the substitution of the atomic mass for the weight in the calculation. However, the trend was preserved and therefore can theoretically still be used in applications such as correlation to helical twisting power as explored by Neal *et al.*⁶

The true benefit of introducing the weights is in the overall model flexibility. This flexibility may potentially lead to a chiral index that correlates well with experimental data of helical twisting power or another desirable molecular property.

V. APPLICATION TO THE NICKEL DITHIOLENE SYSTEM

The nickel dithiolene system is a relatively new group of organometallic dyes that absorb light in the near infrared region. These molecules are based on a rigid dithiolene core centered on a nickel atom (see Fig. 4).



From the core extend four flexible carbon spacers indicated as $[CH_2]_n$. The spacers can contain $n = 0, 3, 6,$ or 9 carbons. Either a chiral or a non-chiral terminal (x) group can be attached to each of the spacers (see Fig. 4). Each x-group can contain 1 to 3 chiral centers for a total of 4 to 12 chiral centers in each molecule. A chiral center is defined as an atom in a molecule that is bonded to four different chemical species, thus

creating an optical isomer. Optical isomers can rotate the plane of polarized light in either direction depending on the configuration of the molecule. The x-groups and the nomenclature used throughout this research are shown in Figure 5.


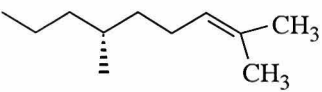
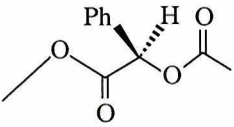
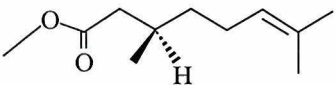
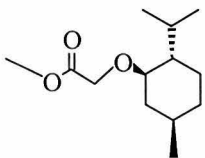
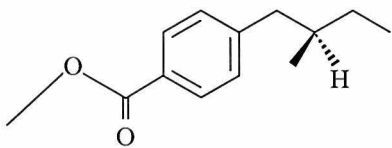
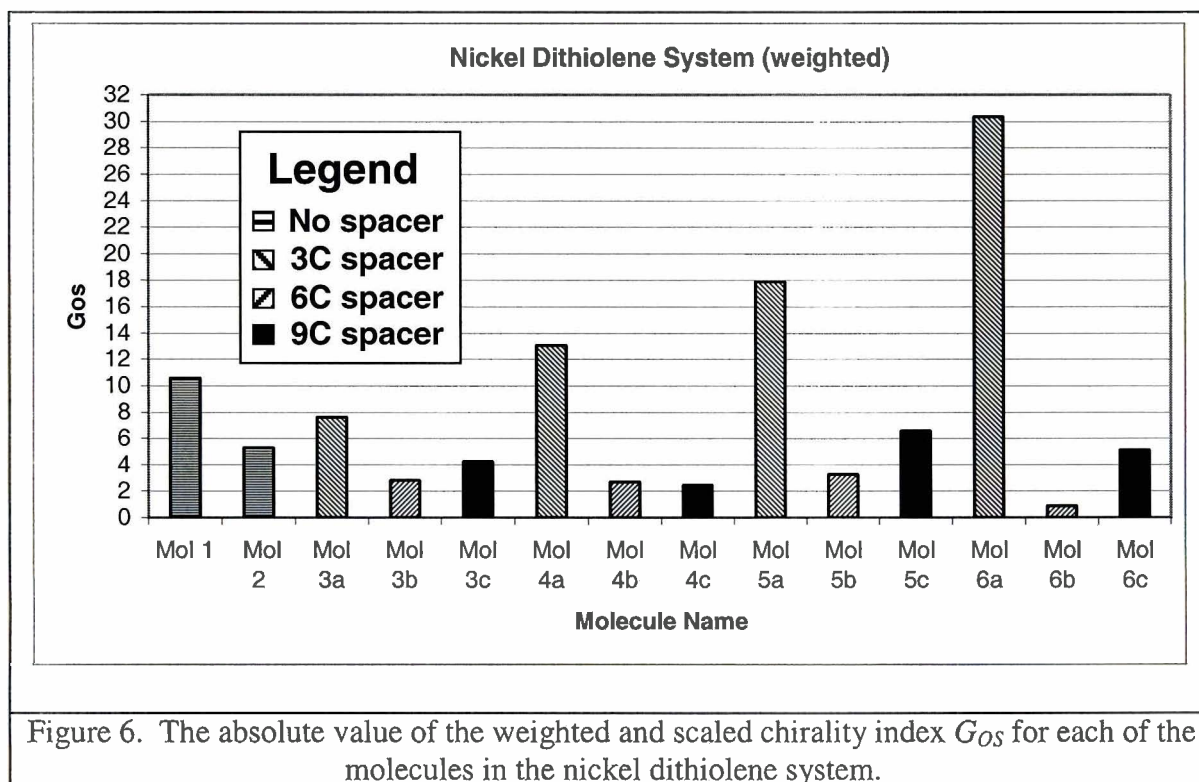
Nomenclature		X-group	Spacer (<i>n</i>)	Weighted and Scaled Chiral Index
Mol 1			0	10.56
Mol 2			0	5.28
Mol 3	a		3	7.60
	b		6	2.81
	c		9	4.24
Mol 4	a		3	13.08
	b		6	2.72
	c		9	2.48
Mol 5	a		3	17.90
	b		6	3.26
	c		9	6.56
Mol 6	a		3	30.35
	b		6	0.87
	c		9	5.13

Figure 5. The chiral X-groups and the nomenclature for the nickel dithiolene system. The largest values of the weighted and scaled chirality indices are found for molecules with spacers containing $n = 3$ carbon atoms.

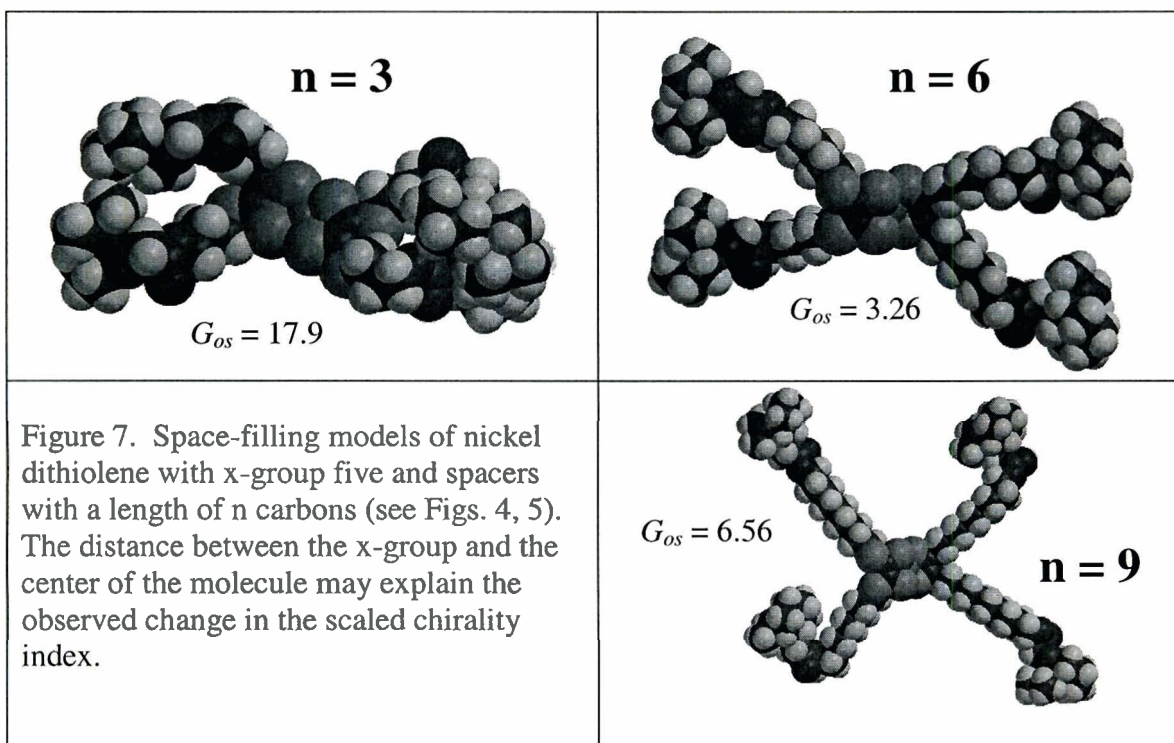
Weighted and scaled chirality indices were calculated for each of the compounds shown in Figure 5. Interesting trends were observed in the chirality index of the molecules.

Figure 6 shows the absolute value of the chirality index for each of the molecules in the nickel dithiolene system. The overall trend shows that with each of the molecules that have a flexible spacer, the chirality index is the greatest when the spacer has three carbons. The scaled chirality index is lowest when there are six carbons in the spacer and increases slightly as the spacer grows to nine carbons.



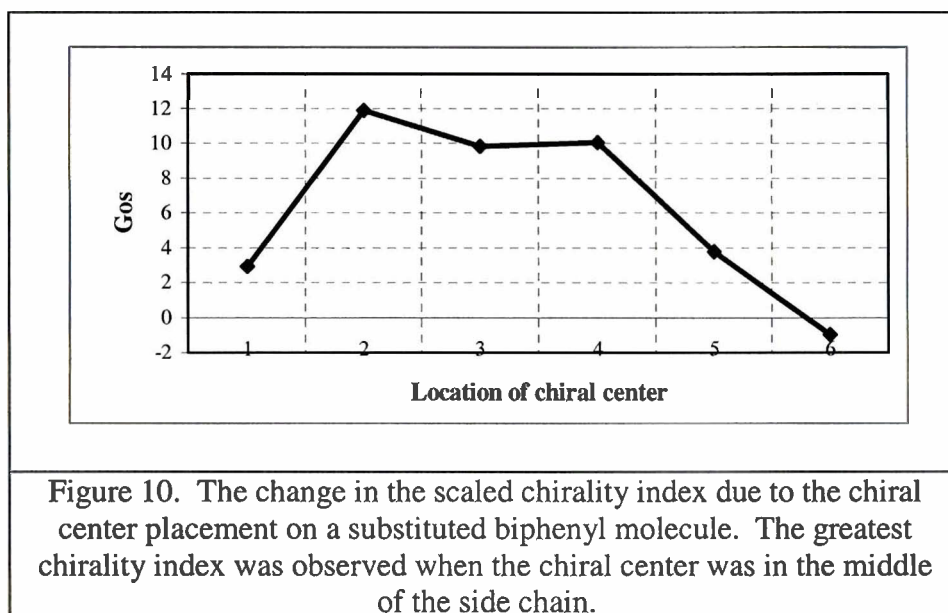
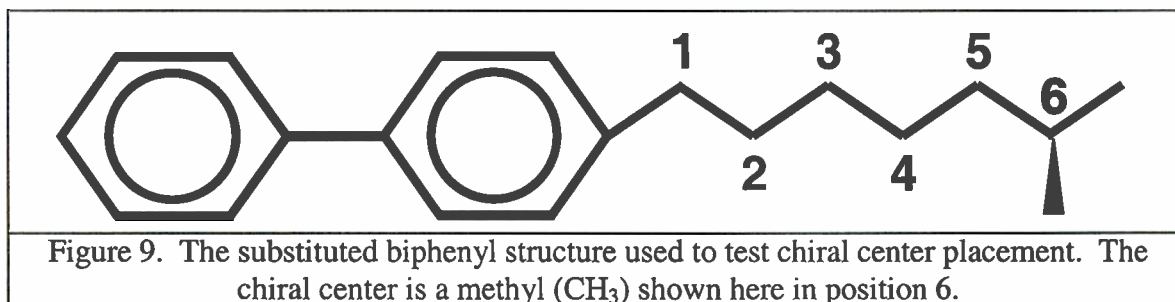
One possible explanation for this pattern is the interactions between the atoms in a molecule. These interactions are known as steric factors and may have a large effect on the chirality index. When the chiral centers of the x-groups are in close proximity to the core, a large stress occurs and thus the chirality increases. When the spacer has six

carbons, the x-groups are at the maximum possible distance from one another in the energy-minimized form. Consequently, the stress on the rings is lessened and the chirality index is smaller. When the flexible spacer has nine carbons, the x-groups begin to wrap back towards the core causing the distance between the groups to shrink and the stress to increase. This is one possible explanation for the observed increase in the chirality index. Figure 7 shows the molecules with x-group five as an example of this occurrence. These space-filling models were exported from the molecular modeling package Spartan 2002, from Wavefunction, and the index was calculated on a SGI Origin 2000 UNIX server with the IRIX 6.5 operating system. They were minimized using the MM2 force field, a version of the MM+ force field discussed earlier.



VI. EFFECT OF MOVING THE CHIRAL CENTER

To test the hypothesis that the scaled chirality index for the nickel dithiolene system depends strongly on the length of the carbon spacers, a modified biphenyl structure was created with a seven-carbon chain attached to one side of the rings (see Fig. 9). To negate the effect of the biphenyl itself, the bond between the rings was frozen at a 0° dihedral angle during energy minimization. A chiral center consisting of a methyl (CH_3) group was moved down the chiral chain from position 6 to position 1, as shown in Figure 9. The graph depicted in Figure 10 shows the result of this movement: the scaled chirality index is the largest when the methyl group is in positions 2 through 4.



One possible explanation for this result is the stresses exerted on the biphenyl rings. When the chiral center was close to the ring structure, little stress occurred because the torque on the rings was not large. One can think of this effect in terms of a lever. If the fulcrum of the lever is close to where the force is applied, it is much harder to do work. In the same way, when the chiral center is close to the rings, a lower chirality index is observed because the force of the chain is less. Likewise, as the chiral center is moved out from the inner rings, a greater chirality index is observed. However, if the chiral center becomes too far away, as observed in the nickel dithiolenes when the spacer had six carbons, the chirality index begins to decrease.

VI. CONCLUSION

A program was written to provide a usable engine to calculate the chirality index for a variety of molecules based on Osipov's initial equations.⁴ This program produced the same results as Osipov *et al*⁴ for a test biphenyl system and scaled these results based on the scale developed by Solymosi *et al*⁵. Functionality was added to allow the weighting of the molecules before calculation. The program was then used to calculate the weighted chirality index for the nickel dithiolene system of molecules. The greatest chirality index was found when the spacers contained three carbons. This result may be explained by the steric factors present in the molecule caused by the location of the chiral centers. This explanation was then confirmed using a substituted biphenyl system.

The weighting system for the chirality index was used to increase the chance of finding a good correlation with, as yet unmeasured, physical properties. As helical twisting power data becomes available for the nickel dithiolene system, a correlation between the weighted scaled chirality index and helical twisting power will be attempted.

Also, to test the weighted calculation of the scaled chirality index, correlations to molecules with known helical twisting power will be made. If substantiated through experimental measurements, this weighted algorithm could be applied to other systems of molecules and enhance the methods of chemical development for industries such as pharmaceuticals and optics.

VII. ACKNOWLEDGEMENTS

I would like to thank Dr. Craxton for providing me with the opportunity to participate in the Laboratory for Laser Energetics Summer Research Program. I would like to thank my advisor Mr. Kenneth Marshall for assisting me with my research throughout the summer. Also, I would like to thank the other students in the research program for being so supportive and making the entire summer enjoyable.

REFERENCES

1. Keinan S, Zabrodsky H, Avnir D. How Much Chirality was there in Pasteur's Tartrate Crystals? The Quantitative Evaluation of the Chirality of Crystals. *Enantiomer*. 1996; Vol. 1(4-6): 351-7.
2. Zabrodsky H, Avnir D. Continuous Symmetry Measures. 4. Chirality. *J. Am. Chem. Soc.* 1995; 117, 462-473.
3. Zabrodsky H, Peleg S, Avnir D. Continuous Symmetry Measures. *J. Am. Chem. Soc.* 1992; 114, 7843-7851.
4. Osipov M, Pickup B, Dunmar D. A new twist to molecular chirality: intrinsic chirality indices. *Molecular Physics*. 1995; Vol. 84(6): 1193-1206.
5. Solymosi M, Low R. A generalized scaling of a chiral index for molecules. *J. Chem. Phys.* June 2002; Vol. 116(22): 9875-81.
6. Neal M, Solymosi M. Helical twisting power and scaled chiral indices. *J. Chem. Phys.* August 2003; Vol. 119(6): 3567-73.
7. Osipov M, Kuball H. Helical twisting power and circular dichroism in nematic liquid crystals doped with chiral molecules. *J. Eur. Phys.* 2001; Vol. 5: 589-598.

X-Ray Microscope Mirror Characterization

Benjamin Schmitt

X-Ray Microscope Mirror Characterization

Benjamin Schmitt
Greece Arcadia High School
LLE Advisor: Frederic J. Marshall

Abstract

Kirkpatrick-Baez (KB) microscopes are used in inertial confinement fusion research to obtain images of plasma x-ray emission. Current KB microscopes used on OMEGA produce a four-image output. A new 16-image KB system is being designed for implementation on OMEGA. Mirror components of the 16-image KB optic were characterized by measuring their precise dimensions, surface roughness, and radius of curvature. A KB optic with a fundamentally smooth surface, built to proper dimensional specifications with an ideal radius of curvature, will allow the mirrors to not only fit into place in the existing microscopes, but also will allow the microscope itself to capture images at optimum focusing performance with minimized aberration. Results have been obtained by using an optical micrometer-measuring microscope, a Taylor Hobson Form Taly Surf 2.0 Profilometer, and a Zygo NewView 5000 white-light interferometer. Raw data output obtained from these instruments has been analyzed using the PV-Wave programming language.

I. Introduction

Inertial confinement fusion (ICF) physics is the study of matter in the plasma state, at ultra-high densities and temperatures, produced by compressing a target (generally comprised of deuterium) using high intensity laser or particle beams¹. To gain a greater understanding of the physical properties of ICF plasmas, direct observation is essential. First developed by physicists Kirkpatrick and Baez in 1948², the Kirkpatrick-Baez (KB) x-ray microscope has since been adapted for use in laser plasma research. On the University of Rochester's OMEGA laser system, KB microscopes are used as a primary means for imaging laser plasma x-ray emission^{3,4,5}. The high density and small scale of the imploding fusion target places unique demands on x-ray diagnostics. An imaging system such as the KB microscope having sufficient spatial resolution, is ideal for understanding the behavior and characteristics of the compressed ICF target core (i.e. density, shape and size.) These instruments are able to produce images of target implosions resulting from ablation of the target outer surface by the intense ultraviolet laser illumination. The KB's currently used on OMEGA produce a four images of target x-ray emission^{3,4,5}. Each x-ray image is produced by the reflection of x rays, striking pairs of perpendicular KB mirrors, which focus the image in both the x and y dimensions, respectively (Fig. 1). For optimum focus to be reached for a given x-ray image, the equation

$$\frac{1}{p} + \frac{1}{q} = \frac{2}{R \sin i} \quad (1)$$

must be satisfied, where p is the source-to-mirror distance, q is the mirror-to-image distance, R is the mirror radius of curvature and i is the angle of incidence of incoming x rays². For enhanced efficiency during optic manufacturing, each mirror is produced with an identical radius of curvature, thus requiring an offset to be introduced between the two mirrors³.

Without additional instrumentation, the KB microscope would produce an output of four identical x-ray images. More useful information may be obtained, however, by

using an x-ray framing camera⁶. An x-ray framing camera is able to introduce temporal resolution to the KB system, thereby allowing each of the four images to be resolved on x-ray film or a digital charged coupled display (CCD) in a chronologically increasing fashion. Consequently, each image is able to directly portray a different discrete stage of the evolution of the target implosion. This is essential to directly observe and record information relating to the dynamically changing implosion process.

Recent efforts at the Laboratory for Laser Energetics have resulted in the design of a KB microscope capable of producing 16-images of the target implosion process⁷. This KB design employs an optic, constructed to dimensions able to replace the existing optical assembly, (Fig. 2). As with the four-mirror system, each mirror is produced with an identical radius of curvature, again making it necessary for a slight offset to be introduced between each pair, with reflective surfaces perpendicular to one another, as illustrated in (Fig. 3). This will allow the images to be cofocal. This design will also incorporate an x-ray framing camera and will require modification to the existing design that can frame four KB images⁸. Mirrors forming the KB x-ray optic must be precisely constructed in order to obtain well-focused images. This work describes the ideal mirror specifications, method of characterization, and resulting measurements gathered throughout the investigation.

II. Characterization of the 16-Image KB Microscope Mirror

Mirror characteristics such as dimension, radius of curvature and surface roughness must all be determined when constructing a functional mirror system for the 16-image KB microscope. For this reason, direct measurement and characterization of each of the 32 KB mirrors is essential.

A. Mirror Dimensions

An optical micrometer-measuring microscope was used to measure the mirror dimensions. This microscope, with its three adjustable axes and lighted stage, permitted

focusing on the mirror through its plastic container. Viewing the mirror surface through the ocular, the x- and y-axes of the stage were adjusted until the ocular crosshair was centered above a given vertex of the mirror. The specific x and y coordinate values of that mirror vertex were then recorded from the primary and vernier analog measurement dials of the microscope. Figure 4 depicts the coordinate labels given to each of the mirror vertices. The mirror side BC refers to the mirror's curved reflective surface. To ensure that this measuring microscope would offer reasonable results, initial coordinate data for a mirror with known dimensions was gathered. Using these coordinates, length measurements for the dimensions of the mirror were calculated using the equation:

$$L = \sqrt{(x_2 - x_1)^2 + (y_2 - y_1)^2} \quad (2)$$

where L is the distance between two vertices, x_2 is the x-coordinate of the first vertex, y_2 is the y-coordinate of the first vertex, x_1 is the x-coordinate of the second vertex, and y_1 is the y-coordinate of the second vertex. Upon confirmation of reasonable mirror coordinate values, the remaining 38 mirrors were measured. With these coordinate values, a fitting program was developed to analyze the measurements written in the PV-Wave computer programming language⁹. This program fit a set of ideal mirror coordinates to the input measured data. This was accomplished first by translating the ideal coordinates such that the midpoint of the base AD was superimposed over the measured base midpoint. This midpoint was determined using the equation:

$$m = \left(\left(\frac{x_1 + x_2}{2} \right), \left(\frac{y_1 + y_2}{2} \right) \right) \quad (3)$$

where m is the midpoint between two vertices, and (x_1, y_1) , (x_2, y_2) are as defined above. The midpoint of BC was also determined using Equation 3. The ideal coordinates were then rotated a determined angle found using the equation:

$$\theta = \arctan\left(\frac{y_t - y_c}{x_t - x_c}\right) \quad (4)$$

where θ is the angle to be rotated, y_t is the y-coordinate of the midpoint of BC, y_c is the y-coordinate of the midpoint of AD, x_t is the x-coordinate of the midpoint of BC, and x_c is the x-coordinate of the midpoint of AD. Finally, the position of the ideal data was adjusted to minimize the deviation between the measured and ideal coordinates. This was accomplished by using the PV-Wave NLINLSQ function, which uses a modified Levenberg-Mardquardt algorithm¹⁰ to solve the non-linear least squares problem. The algorithm takes as input the estimates of the three parameters x_c , y_c , and θ , and minimizes the square deviation between the points. The least squares deviation is determined using the equation:

$$\sigma^2 = \sum_{i=1}^4 |(f_i - x_i)^2 + (g_i - y_i)^2| \quad (5)$$

where f_i and g_i are given by:

$$f_i = x_i \cos \theta - y_i \sin \theta + x_c \quad (6)$$

$$g_i = x_i \sin \theta + y_i \cos \theta + y_c \quad (7)$$

With this calculation, the deviation of each measured mirror from ideal specification was determined.

B. Radius of Curvature:

Given a fixed image plane, any variation from the ideal mirror radius of curvature will degrade the apparent resolution of the microscope. Geometrical object resolution was determined for mirrors of various radii of curvature, using the ray tracing software Zemax¹¹. Figure 5 shows the object resolution for a mirror with an ideal radius of curvature of 25.6 meters, as well as the degraded resolution for a mirror with a 5% deviation in radius of curvature, with the other focus parameters held fixed (i.e. same

source and image distance.) The importance of keeping the mirror curvature the same for multiple pair KB microscopes, such as the 16-image KB, is evident. Two instruments were used to measure radius of curvature of the KB mirrors: a Taylor Hobson Form Taly Surf 2.0 Profilometer¹², and a Zygo NewView White Light Interferometer¹³. A sample of 16 mirrors were selected for measurement. The mirrors were placed in a protective fixture that was constructed to expose only the desired surface of each mirror to be measured. The Taylor Hobson profilometer measures the surface depth by moving a precision diamond-tipped stylus across the surface of the mirror. These measurements were analyzed using a PV-Wave program designed to fit this data to a curve. Using the PV-Wave routine NLINLSQ (see section II(a)) this program was able to determine deviation of the measured radius of curvature from the ideal, through the equation:

$$\sigma^2 = \frac{1}{N} \sum_i f_i^2 \quad (8)$$

where σ^2 is the calculated curvature deviation from ideal, f_i is defined by the function:

$$f_i = R^2 - (x_i - x_c)^2 - (y_i - y_c)^2 \quad (9)$$

where R is the ideal radius of curvature, x_i is the x value of a measured mirror coordinate, x_c is the x value of the calculated center of curvature, y_i is the y value of a measured mirror coordinate, and y_c is the y value of the calculated center of curvature. The Zygo interferometer was used to verify these results. Using the connected Zygo MetroPro software program¹³, the depth measurements obtained from the surface scan could then be displayed. An internal software function was then used to determine a calculated radius of curvature value for the scanned mirror surface (circular.) While both of these instruments offered reasonable results for the mirror radius of curvature measurements, the Zygo interferometer was deemed a superior measuring tool for mirror radius of curvature, as it offered a non-contact method of measurement and also displayed results that were accurate to the one Angstrom level for vertical resolution, while the Taylor Hobson Profilometer was accurate to the 12 nm level (120 times less resolution).

C. Surface Roughness

In order to attain good image focus, microscopic surface features of the KB microscope's reflecting surface must be taken into account. Any deviations from a constant radius of curvature found on the surface of the mirror, could degrade image quality. The Zygo NewView 5000 white light interferometer with a 20x ocular was used to measure the surface roughness of each mirror. The larger magnification revealed a higher degree of detail regarding the surface roughness. Through the built in Zygo MetroPro software¹³, the root mean squared (rms) value of the degree of surface roughness was generated, again accurate to the one Angstrom level. This rms value represented the mean degree of deviation of each surface scan from an ideal curve (circular).

III. Results

A. Mirror Dimensions

The root mean square (RMS) output of the PV-Wave dimensional best-fit program, both cumulative and for individual vertices, is found in Table 1. Here, it is found that mirror C06 was the least in deviation from ideal, with a RMS of 21.8 microns while mirror B18 was greatest in deviation with a RMS value of 43.0 microns. Cumulative measured mirror coordinate offsets from ideal are also depicted in Fig. 6. A contributing source of measurement error was noticed that the mirrors were measured with their protective casings on, leading to distortion.

B. Radius of Curvature

As was described in section II(B), a 16-image KB mirror with a precise radius of curvature is necessary for ideal x-ray image focus and resolution. The 16-image KB

microscope, is designed with a mirror radius of curvature of 25.6 m. A larger four-image KB mirror with a sufficient curvature to be measured by both the Taylor Hobson and the Zygo was used to substantiate the measurements of the new mirrors (Fig. 7). It was therefore concluded that the measurements from these instruments were indeed reliable. When test 16-image mirror measurements were completed, varied results were obtained. Using the PV-Wave NLINLSQ curve-fitting program, the test measurements obtained by the Taylor Hobson Profilometer for mirror B08, offered a radius of curvature of 25.65 m, which is nearly ideal. However, the Zygo interferometer produced a surface profile not spherical in nature, with a much smaller radius of curvature (Fig. 8.) Due to this inconsistency, the usefulness of these mirrors has been brought into question. As a result, a sample mirror (KB_B08) was returned to the manufacturer (Research Electro-Optics¹⁴).

C. Surface Roughness

As was mentioned in section II(C), a fundamentally smooth reflective mirror surface is needed for optimum image resolution. With the 16-image KB mirror, surface roughness should not exceed 5.0 Angstroms. The RMS roughness values that were measured using the Zygo interferometer generally fell within a range to the order of 5.0 Angstroms or less. As a result, it was concluded that these mirrors were sufficiently smooth and within specification.

IV. Conclusions

The Kirkpatrick-Baez x-ray microscope is an essential instrument for laser driven ICF diagnostics. While current KB microscopes in use on OMEGA produce four-images of the target x-ray emission, a new design produces a 16-images, which can be used for high resolution, temporally resolved (framed) imaging of target implosions. This work describes the method and results of characterizing mirrors that comprise the 16-image microscope (i.e. measuring the dimensions, radius of curvature, and surface roughness.) The microscope used has sufficient resolution to determine the dimensions to $\pm 5 \mu\text{m}$. Mirror curvature was determined using both a white light interferometer and a surface

profilometer. The interferometer had superior resolution and could best determine the curvature and surface roughness. Deviation of the mirrors from the desired ideal concave surface was significant and means that they may not produce usable images. This will require further investigation, both at the University of Rochester and Research Electro-Optics.

Acknowledgements

I would like to thank my advisor F. J. Marshall for his direction and support of my work, R. S. Craxton for giving me the opportunity to join such a unique and worthwhile program, and also J. Laine, R. Forties, L. Gregg, E. Fess, M. Bonino, G. Mitchell, and fellow students in the summer research program for their role in assisting my efforts throughout this investigation. Their continued guidance and encouragement was greatly appreciated, and the experience that I have acquired working with each of them will be an invaluable resource in future scientific, technological, and business endeavors.

Figure Captions

FIG. 1. Isometric view of a four-image KB optic.

FIG. 2. Isometric view of a four-image KB microscope assembly as used on OMEGA.

FIG. 3. Schematic diagram of a completed 16-image KB mirror pair. (a) Offset mirror pair with reflective surfaces at a perpendicular. (b) Side view of KB mirror pair with mirror offset indicated.

FIG. 4. Schematic diagram of a single 16-image KB mirror with measured coordinates A, B, C, and D labeled. Note: BC indicates the mirror reflective surface location.

FIG. 5. ZEMAX ray tracing simulations of KB image resolution. Solid line indicates resolution of mirrors with an ideal radius of curvature. Dotted lines indicates resolution of mirrors with a +/- 5.0 % radius of curvature deviation.

FIG. 6. Frequency histogram of mirror dimensional root mean square (RMS) offset from ideal.

FIG. 7. Surface profile of four-image KB mirror. (a) 3D surface profile of mirror measured using a Zygo NewView 5000 white light interferometer. (b) Plot of mirror surface profile obtained using a Taylor-Hobson Form Taly Surf 2.0 profilometer; fitted to an ideal curve using PV-Wave NLINLSQ command.

FIG. 8. Surface profile of 16-image KB mirror. (a) 3D surface profile of mirror measured using a Zygo NewView 5000 white light interferometer. (b) Plot of mirror surface profile obtained using a Taylor-Hobson Form Taly Surf 2.0 profilometer; fitted to an ideal curve using PV-Wave NLINLSQ command.

Table Captions

Table 1. Table of measured 16-image KB mirrors individual and cumulative deviation from ideal coordinate dimensions.

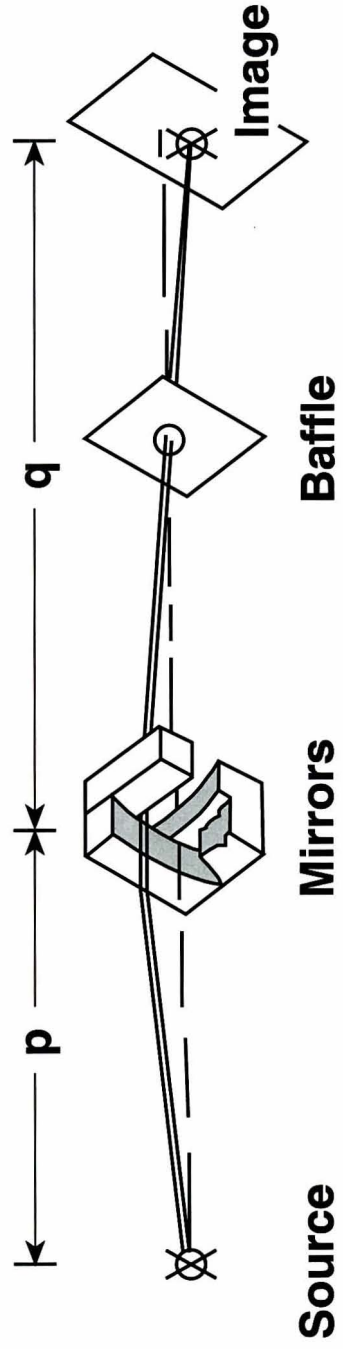
References

1. J. D. Lindl, *Inertial Confinement Fusion: The Quest for Ignition and Energy Gain Using Indirect Drive* (Springer-Verlag, New York, 1998).
2. P. Kirkpatrick and A. V. Baez, *J. Opt. Soc. Am.* **38**, 766 (1948)
3. F. J. Marshall and Q. Su, *Rev. Sci. Instrum.* **66**, 725–727 (1995).
4. F. J. Marshall, J. A. Oertel, *Rev. Sci. Instrum.* **68**, 735-739 (1997).
5. F. J. Marshall, M. M. Allen, J. P. Knauer, J. A. Oertel, and T. Archuleta, *Phys. Plasmas*, **5**, 1118-1124 (1998).
6. D. K. Bradley, P. M. Bell, O. L. Landen, J. D. Kirkenny, and J. A. Oertel, *Rev. Sci. Instrum.* **66**, 716 (1995).
7. Dr. F. J. Marshall, Senior Scientist, University of Rochester, Laboratory for Laser Energetics, 250 East River Road, Rochester, NY 14623
8. J. A. Oertel, T. Archuleta, C. G. Peterson, and F. J. Marshall, *Rev. Sci. Instrum.* **68**, 789 (1997)
9. PV-Wave, Version 7.00, Visual Numerics, Inc., 2000 Crow Canyon Place Suite 270, San Ramon, CA 94583 (1999)
10. Levenberg, K. (1944), A method for the solution of certain problems in least squares, *Quarterly of Applied Mathematics*, **2**, 164-168.

Marquardt, D. (1963), An algorithm for least-squares estimation of nonlinear parameters, SIAM Journal on Applied Mathematics, **11**, 431-441

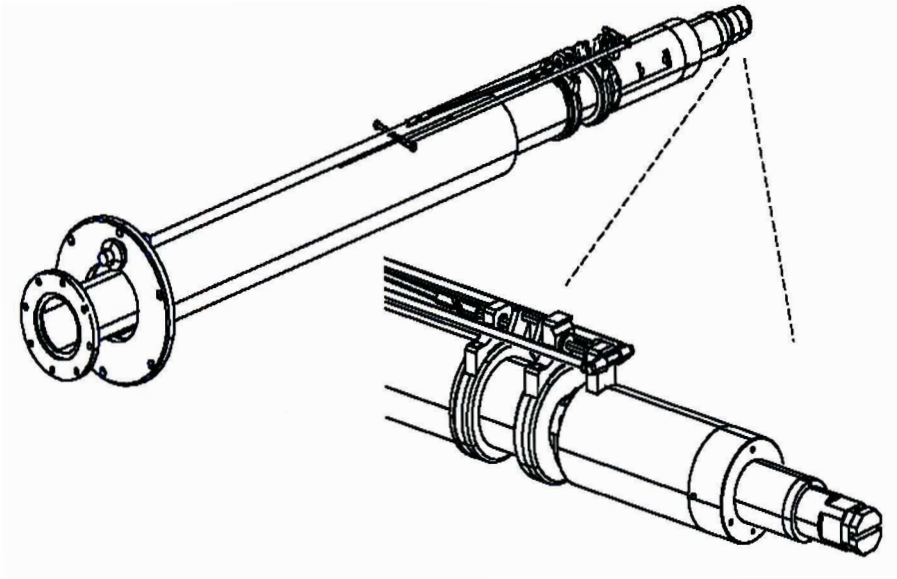
11. ZEMAX-XE Optical Design Program, Version 8.1, S.N. 102-7180, Focus Software Inc., Tucson, Arizona, (©1990-1999)
12. Taylor Hobson Precision Form Taly Surf Series 2 Operators Handbook, Taylor Hobson Precision, Leicster, England, Pub. No. K505/9, software version 06.xx
13. Zygo Interferometry and Data Analysis Mark N XP Operation Manual, Zygo Corporation, Middlefield, Connecticut, OMP-0287C (Feb. 1991)
14. Research Electro-Optics, Inc., 5505 Airport Blvd, Boulder, Colorado 80301 USA

Fig 1



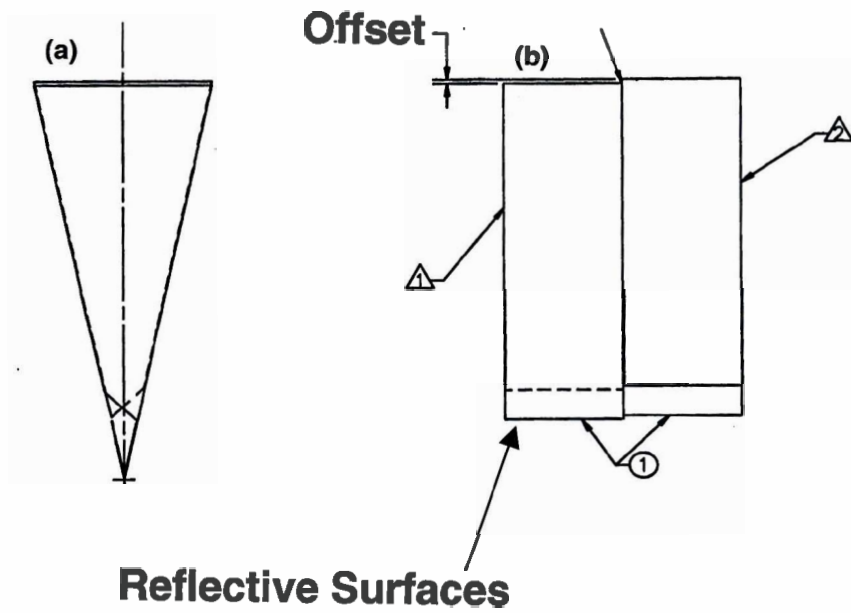
E8640

(Figure 2)

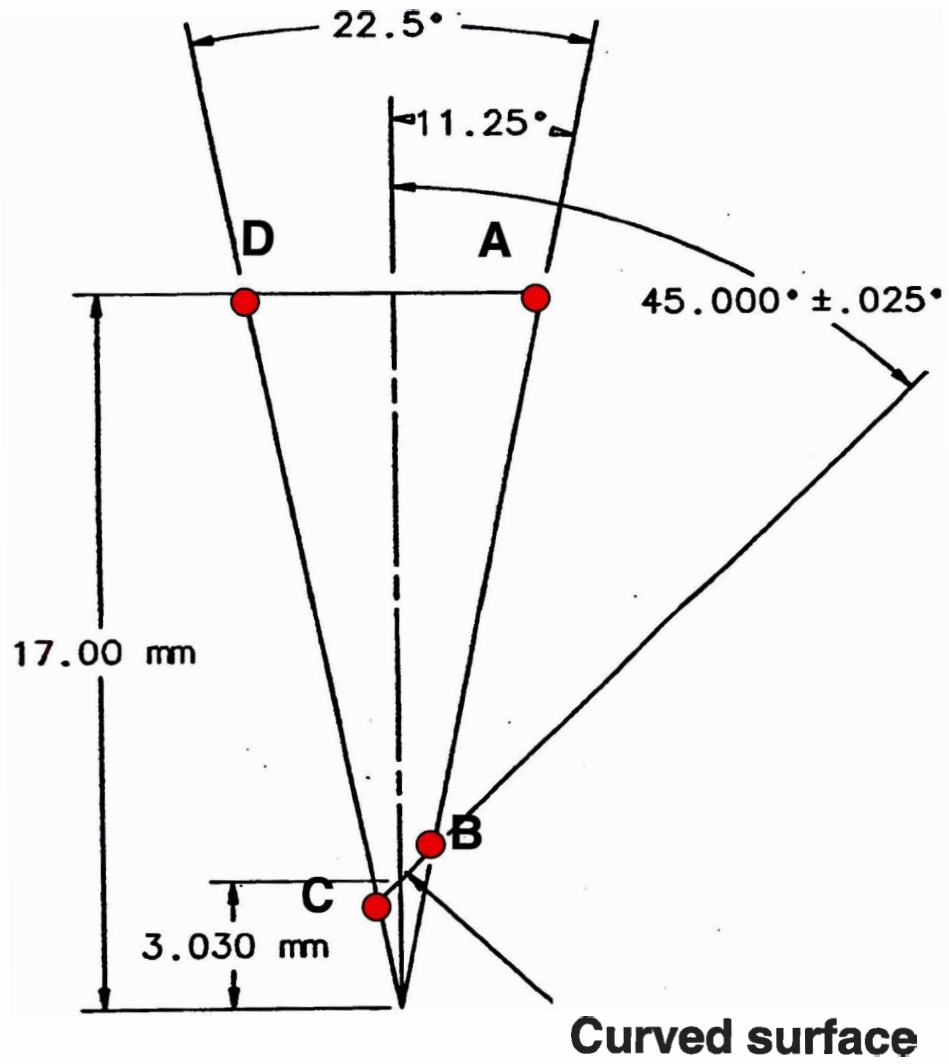


4-image KB optic

(Figure 3)

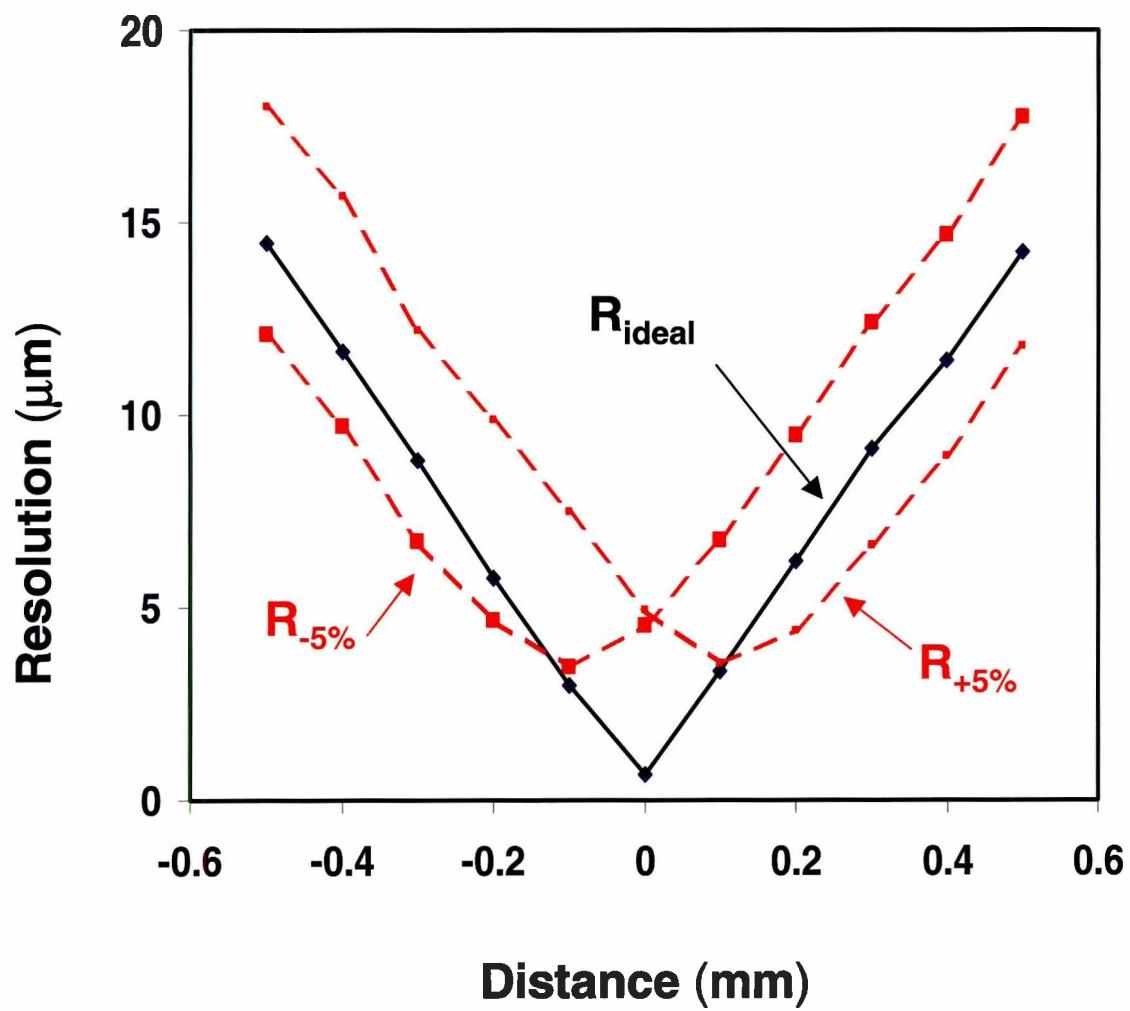


(Figure 4)

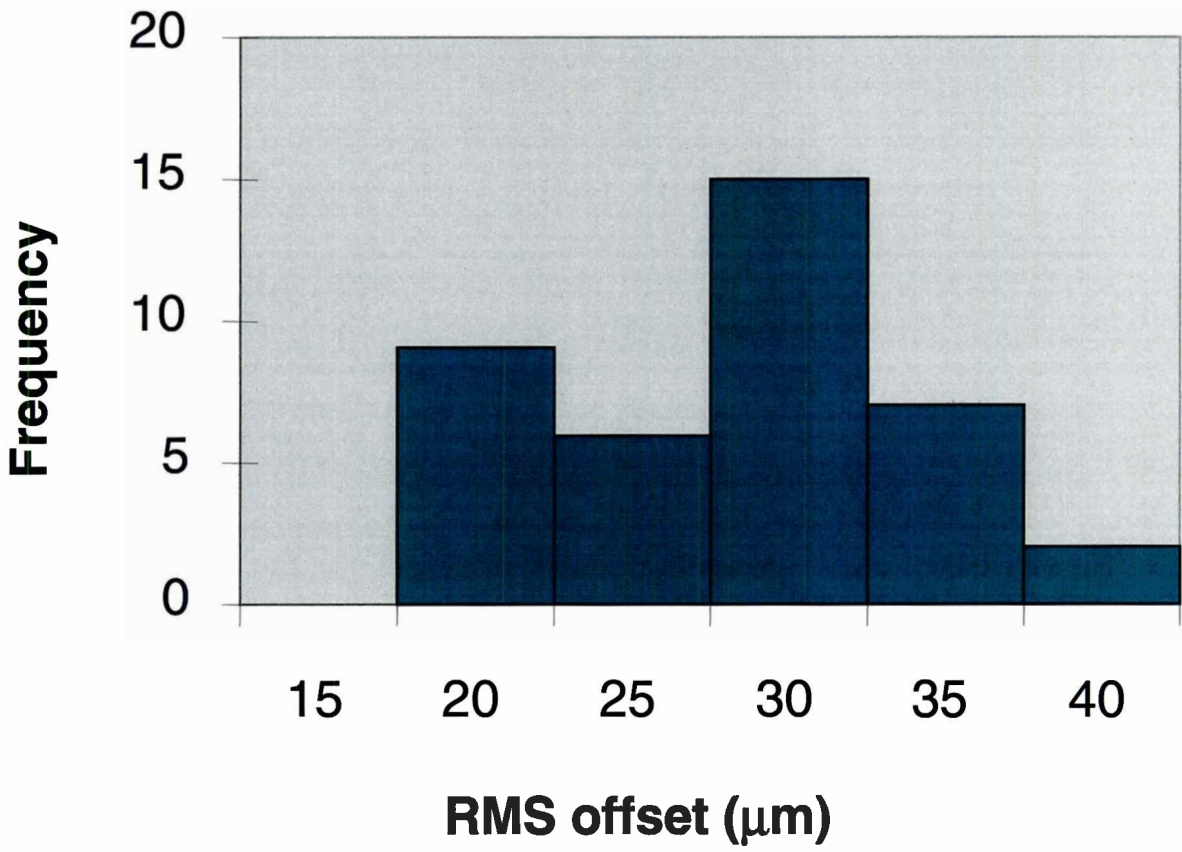


(Figure 5)

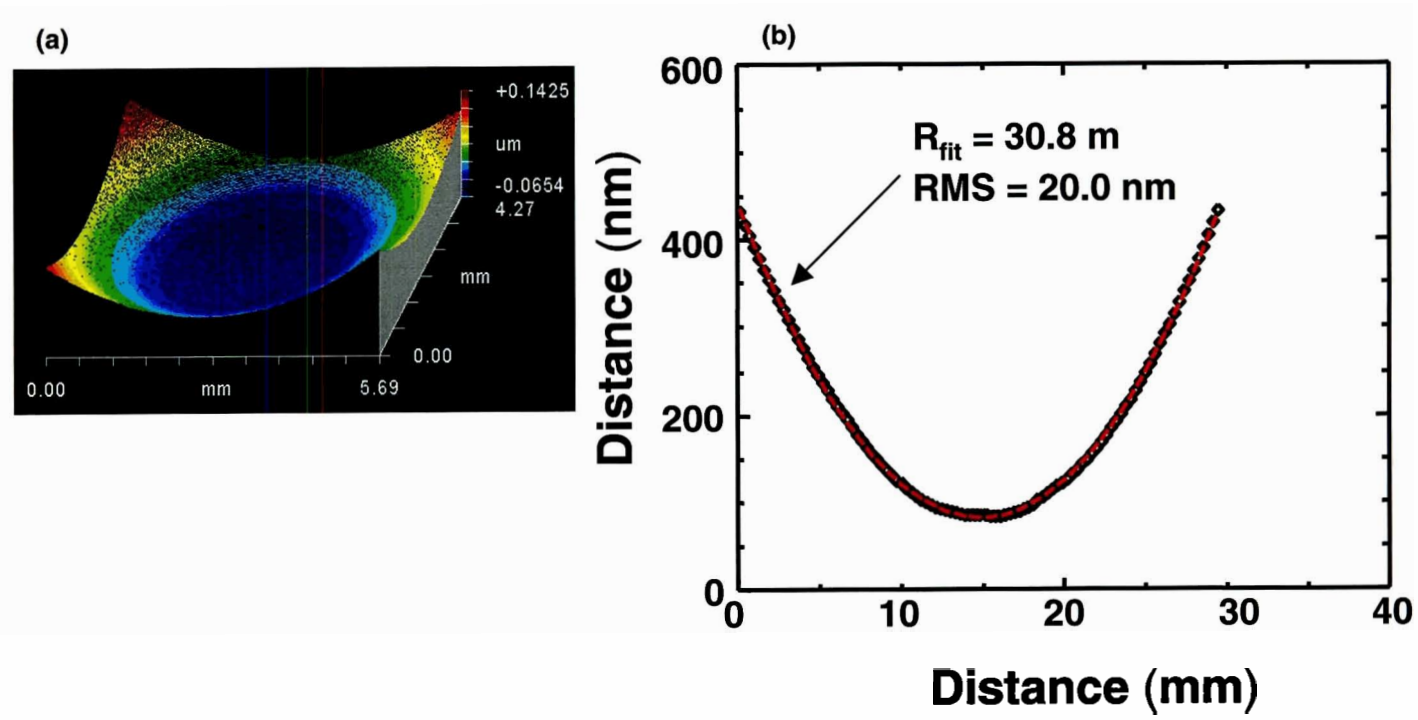
ZEMAX simulations



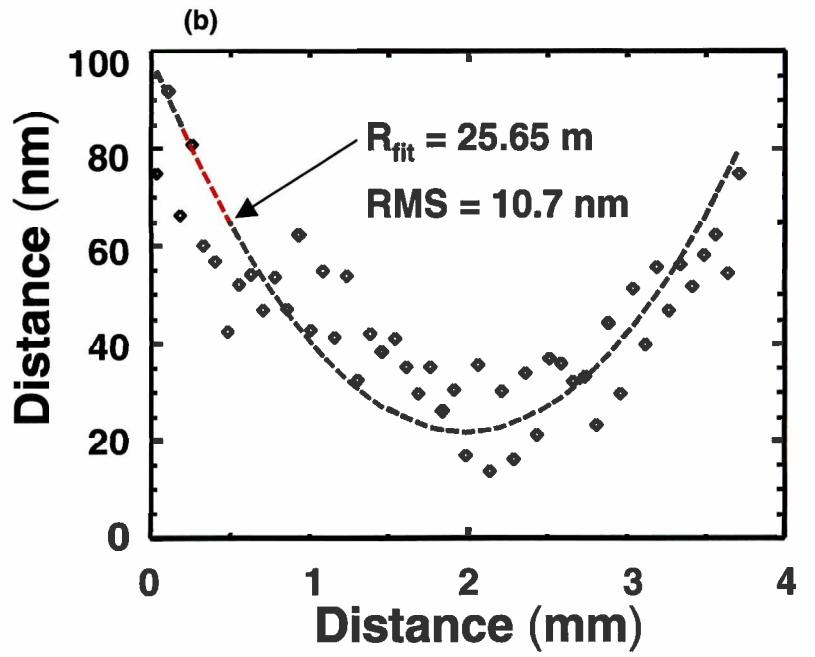
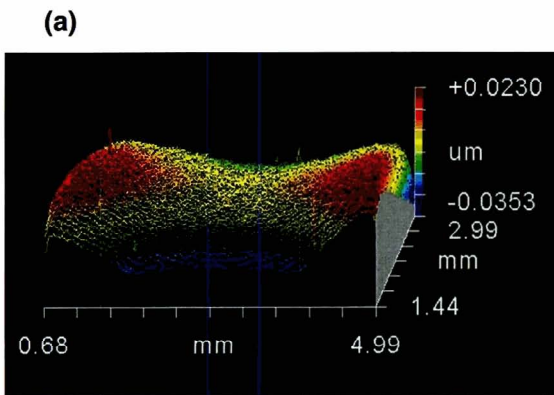
(Figure 6)



(Figure 7)



(Figure 8)



(Table 1)

Deviation of Measured Coordinates from Ideal Coordinates (microns)					
Serial #	Deviation from A	Deviation from B	Deviation from C	Deviation from D	Root Mean Square
C06	22	21	22	23	21.8
C17	24	10	26	26	22.3
C10	20	17	30	20	22.4
A05	18	23	31	18	23.0
C01	14	23	36	12	23.2
C15	22	23	30	19	24.0
C18	31	20	24	20	24.2
B08	12	18	30	32	24.4
C03	25	14	35	20	24.8
B12	17	20	39	22	25.9
B17	28	16	30	29	26.4
C08	24	14	41	21	26.8
B04	22	24	36	30	28.3
C02	32	20	35	25	28.5
A11	30	24	34	26	28.7
B11	26	20	42	28	30.1
C04	19	30	41	25	30.1
B10	31	17	41	28	30.1
C05	36	13	35	35	31.3
B07	25	29	41	28	31.5
C09	34	22	35	35	31.7
C14	34	30	37	25	31.8
B06	36	16	41	30	32.2
C12	37	22	40	27	32.3
B13	29	19	41	35	32.3
B14	33	16	42	34	32.7
A16	32	27	35	37	33.1
A06	30	31	46	24	33.6
C13	17	33	55	18	34.2
A12	37	22	45	30	34.6
C11	23	49	39	24	35.3
B01	43	15	38	40	35.5
B15	38	28	47	36	38.0
B05	26	34	56	30	38.2
B03	44	26	45	36	38.5
A07	34	33	55	30	39.1
B16	44	18	55	33	39.8
B09	39	24	59	36	41.7
B18	36	15	67	38	43.0

**Compressed Core Characterization of a Cryogenic D₂ Target at Peak
Neutron Production**

Nicole Toscano

Nicole Toscano

**Compressed Core Characterization of a Cryogenic D₂ Target at
Peak Neutron Production**

Nicole C. Toscano
Greece Arcadia High School
Rochester, N.Y.

Advisor: Vladimir A. Smalyuk
Research Scientist

Laboratory for Laser Energetics
University of Rochester
Rochester, N.Y.

Compressed Core Characterization of a Cryogenic D₂ Target at Peak Neutron Production

Abstract

The accurate characterization of compressed targets uniformly irradiated by laser beams is of highest importance for the success of inertial confinement fusion (ICF). Computer programs have been developed and used to make such a characterization based on a number of experimental measurements of the target core near peak compression. The temperature and density profiles of the hot compressed core of a cryogenic deuterium target have been characterized using measured fusion neutron yields, the neutron-averaged ion temperature, and the x-ray image at peak compression.

I. Introduction

The society in which we live is dependent upon natural resources for our survival as well as technical and intellectual progress. However, the consequences of burning fossil fuels such as natural gas, coal, and oil are devastating to the environment and humanity. The burning of these energy sources produces large amounts of carbon dioxide and sulfur. Nitrous oxides already present in the air combine with sulfur producing sulfuric acid and nitric acid forming acid rain. Acid rain damages trees and depletes the soil of nutrients, causing the soil to become more toxic. In industrialized nations such as the United States red spruce forests have become

more susceptible to damage as a result of acid rain. Acid rain also affects the pH of bodies of water, lowering their pH enough to alter the reproductive activities of certain fish species. Global warming, widely believed to be due to the presence of excessive amounts of carbon dioxide in the atmosphere is another prime example of how burning fossil fuels can impact the environment. Potentially the consequences of burning natural resources could dramatically change the climate of Earth if it is not stopped. Many are concerned with the amount of fossil fuels that are left for consumption. Oil is expected to run out in about 50 years at the current rate of consumption. As a result it is imperative for alternative energy sources to be produced in the near future.

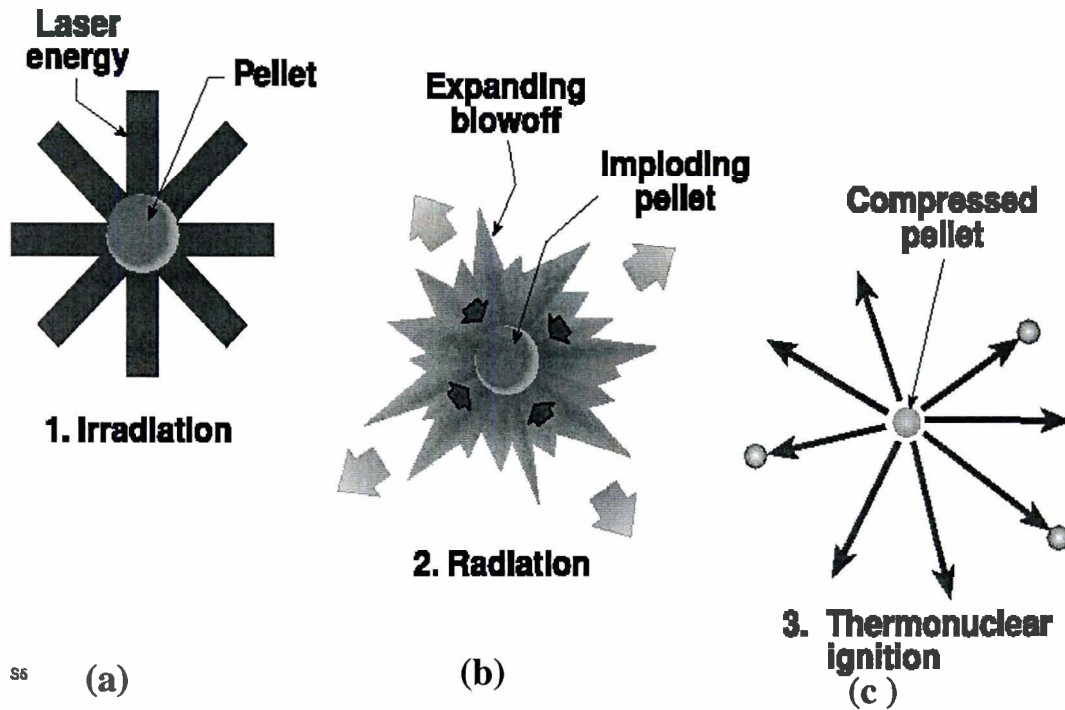
To ensure the survival of humanity and the stability of the environment it is necessary for the scientists of today to develop an alternate means of energy production. For the past 50 years fission has been viewed as a promising method for producing energy. In fission nuclear reactions, high Z-elements split. As the atoms breakdown into less complex elements energy is released. However, this process produces highly radioactive materials which are harmful for both animal and plant life. As a result, many nuclear fission programs have been suspended internationally.

An alternative to this process is fusion. In fusion nuclear reactions, lighter elements are combined to form heavier ones with a release of energy. Fusion is a very promising source of energy as compared to fission and especially to the burning of fossil fuels. Neither the reactants nor the products in a fusion reaction are significantly radioactive, making fusion much safer for the environment. Additionally the resources are abundant. 1 km³ of ocean water provides enough of the hydrogen isotope deuterium to replace the rest of the world's supply of oil which

amounts to roughly 500 billion barrels. Fusion already plays a vital role in life on Earth. The energy produced in the sun and the stars occurs as a result of fusion reactions.

As on the sun, hot and dense plasma needs to be produced in order for the fusion reactions to take place. In the sun fusion occurs at high temperatures $\sim 10,000,000^\circ\text{K}$ and high densities of $\sim 10^{25}$ electrons/cm³. Therefore it is a challenge for scientists to create and control plasma at such critical conditions in the laboratory. There are different approaches to achieve this, including magnetic confinement fusion (MCF) and inertial confinement fusion (ICF). MCF uses a magnetic field to retain the plasma, allowing for the nuclear reactions to take place. In ICF, lasers and charged particle beams are used to create high temperatures and densities within the central parts of the pellet (target core) creating nuclear reactions. In direct-drive ICF, a large number of laser beams are focused uniformly on the target to achieve uniform compression and heating.¹

Laser-driven ICF is a three step process and can be seen in Fig.1. The pellet containing fusion fuel, typically the hydrogen isotopes of deuterium and tritium, is first irradiated using laser energy. A large number of beams is necessary for uniform irradiation [see Fig.1 (a)]. The target reaches an extreme temperature causing the outer portion to expand and blowoff. As a result of Newton's Third Law the pellet then implodes, compressing the fuel within it [see Fig.1 (b)]. At peak compression, when high temperatures and densities are achieved in the target core, the deuterium (D) and tritium (T) of the fuel are able to react releasing neutrons and charged particles as shown in Fig. 1(c). A large amount of energy is released in each fusion reaction. Currently, ICF is a leading area of research in scientific laboratories throughout the world.²



56

Figure 1: Schematic of the target implosion in laser driven ICF.
 (a) Irradiation. Many laser beams directly illuminate the target for uniform compression.
 (b) Radiation. While the outer part of the target is ablated the inner part moves to the center.
 (c) At peak compression fusion reactions occur in high temperature and high density plasma.

The Laboratory for Laser Energetics (LLE), in Rochester, NY currently possesses the most powerful laser system (the OMEGA laser) in the world, used for ICF research. The OMEGA laser, which is the size of a football field, has 60 beams allowing for a uniform heating of small, ~1mm diameter targets. The more laser beams there are the more the more uniform the target is heated. One of the goals of ICF research and of the OMEGA laser³ program in particular is to study, approach, and achieve ignition using cryogenic DT and D₂ capsules.

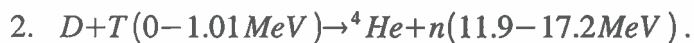
Scientists have not yet met this goal but they are on their way to achieving it.

In order for ignition to occur the energy that is produced from fusion must be equivalent to or greater than the laser energy that is input into the system. The most energetically favorable fusion reaction for energy production is $D+T \rightarrow He^4(3.5\text{ MeV})+n(14.1\text{ MeV})$. Each reaction releases 2.8×10^{-12} J of energy (or 17.6 MeV). In the case of the OMEGA laser, 30 kJ of energy is input into the target through the 60 beams in laser light; therefore, to ignite the target, it is necessary to achieve a total yield of $\sim 1.0 \times 10^{16}$ fusion reactions in one implosion. The target on OMEGA is 1 mm in diameter containing $\sim 100 \mu\text{m}$ thick deuterium-tritium (DT) ice.⁴ The ice is created at a cryogenic temperature of $\sim 18^\circ\text{K}$.

While DT fuel will be used primarily for energy production, targets with cryogenic D_2 fuel are very helpful for hot core characterization at peak compression. Ion temperature, areal density, and convergence ratio are more easily measured in D_2 fuel than in DT fuel.⁵ There are two primary fusion reactions in D_2 fuel:



Each of these reactions has a 50% chance of occurring. The first primary reaction produces a triton, T, which can react with a deuteron, D, through the secondary reaction



The yields of both DD primary and DT secondary reactions depend on the temperature and density of the compressed core.

One of the most critical aspects of the ICF program is a characterization of the fuel during peak compression. It is necessary to access the efficiency of implosion and to guide

future experiments. Such comprehensive characterization is very challenging because the implosion happens during a very short period of time (~ 1 ns) and the size of the fuel core at peak compression is very small, about ~ 100 μm . The primary goal of this project was to find out if the experimental observations such as neutron yields of fusion reactions, core x-ray images could provide comprehensive information about the structure (temperature and density distribution) of the hot core at peak compression. It was found that the temperature and density profiles can be inferred from the measured primary DD and secondary DT neutron yield, the measured neutron-averaged ion temperature, and the measured x-ray images of core emission, as presented in this article. These profiles will be used to optimize the target designs of the ignition experiments planned in the near future.

During the target implosion, any perturbations present grow due to Rayleigh-Taylor (RT) instability⁶, compromising target performance and reducing fusion yield. To overcome this obstacle, more stable target designs are proposed which include using bigger, more massive targets driven with more powerful laser systems. The effect of detrimental perturbation growth due to RT instability is much less in bigger targets.⁵ To support the goal of ignition and high gain, the National Ignition Facility (NIF) is currently being built in Livermore, California. This 1.8 MJ, 192 beam laser system is expected to ignite cryogenic DT targets. To achieve ignition on NIF, the experiments on OMEGA study physics of various aspects of ICF. The project that I was involved, presented in this article, is directly related to the most important physics aspect of ICF – characterization of the hot core at peak compression of spherical implosion.⁷

II. Experimental Conditions

The schematic for the cryogenic capsule used in shot 28900 is shown in Fig. 2. The 1-mm diameter target has a shell with an outer $\sim 5\text{-}\mu\text{m}$ -thick CD layer and an inner layer of $\sim 100\ \mu\text{m}$ thick D_2 ice, made at a temperature of $\sim 18\ \text{K}$. The target was driven with a 23-kJ, 1-ns pulse by the 60-beam OMEGA laser system containing $\sim 23\ \text{kJ}$ of on-target energy. The laser beams were smoothed using a series of two processes including spectral dispersion (2-D SSD)⁸ and polarization smoothing (PS)⁹. The primary DD neutron yield was $1.24 \times 10^{11} \pm 7.64 \times 10^8$ with a neutron-averaged ion temperature (measured with neutron time of flight) of $3.6 \pm 0.5\ \text{keV}$ and the measured neutron burn width was $\sim 170 \pm 25\ \text{ps}$. The secondary DT yield was $1.17 \times 10^9 \pm 3.17 \times 10^7$. Images of the target at peak neutron production were measured using an x-ray framing camera. The camera has a spatial resolution of $\sim 10\ \mu\text{m}$, a temporal resolution of $\sim 40\ \text{ps}$. The temperature and density profiles of the target core at peak compression can be inferred using these experimentally measured values and time-resolved target x-ray images.

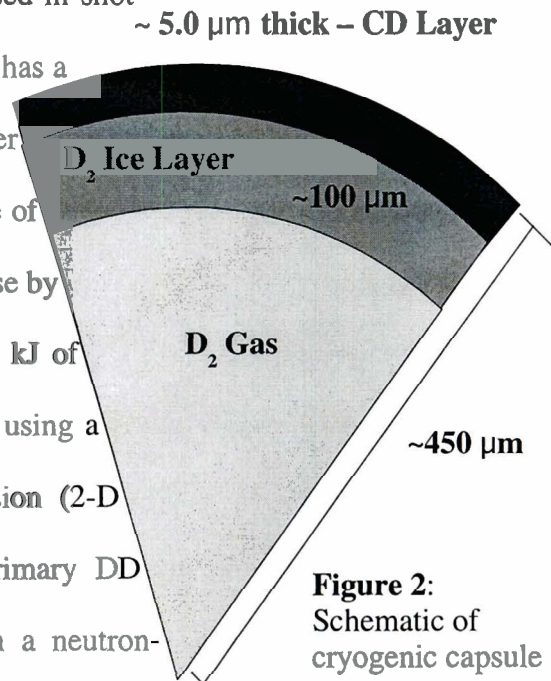


Figure 2:
Schematic of
cryogenic capsule

III. Program Description

Since neutron yields and core x-ray images depend on temperature and density profiles inside the core, the goal of this project was to determine these profiles from the measured neutron and x-ray emissions. Modeling of the target was based on computer programs which varied core temperature and density profiles and then calculated neutron yields, neutron-averaged ion temperature, and x-ray images. Only those profiles which generated neutron and x-ray data consistent with experimentally measured observations were chosen.⁷

The program was set up into four stages. The first stage produced a series of temperature and density profiles that were consistent with the primary DD neutron yield and neutron-averaged ion temperature. Results from this stage were carried over into stage two. Profiles that matched the secondary DT neutron yield were chosen for further analysis. Similar calculations were carried out for a number of core electron pressures ranging from 1 to 10 Gbar in the third stage. Finally the temperature and density profiles consistent with the measured core x-ray image were chosen in the fourth stage of modeling. A series of assumptions were made when modeling the core. First it was assumed that the core of the target was made completely of ionized deuterium ideal gas and that the pressure within the core remained constant. Temperature and density profiles produced were based on a spherically-symmetric target. The core was assumed to be not evolving during peak neutron production.

Figure 3(a) shows two possible temperatures profiles out of about 10^{10} considered in the first stage modeling. Only monotonically decreasing temperature profiles were considered for analysis. The grid used in this modeling had distance increments of 20 μm and temperature increments of 250 eV. Additional grids were produced for distance steps of 15, 10, and 5 μm .

More detailed grids were used for calculations at higher electron pressures. These more specific grids increased the time it took for the program to analyze the $\sim 10^{10}$ temperatures profiles. It was determined that for higher resolutions the program would run for days and sometimes even years before it had completed its necessary task. So we spent a lot of time looking for computation conditions which produced accurate results during a reasonable period of time. Most major physical processes were already incorporated into the programs. These processes included 1) charge particle propagation in plasmas (for triton slowing down and the secondary DT yield calculations), 2) radiation transport of x-rays in plasma, 3) primary DD yield calculations for every particular temperature-density profile, 4) x-ray image construction. In order to perform calculations in a reasonable time, a lot of programming and optimization was performed to optimize calculations, which vary different parameters to understand the sensitivity of results from various physical parameters.

Corresponding density profiles were produced using an ideal gas relationship between temperature $T(\mathbf{r})$ and density $n(\mathbf{r})$. For any given temperature profile the corresponding density profile was determined using this ideal gas equation, $P_e(\mathbf{r})=n(\mathbf{r})T(\mathbf{r})$. The results of stage 1 calculations for a particular electron pressure of 2.6 Gbar are shown in the gray

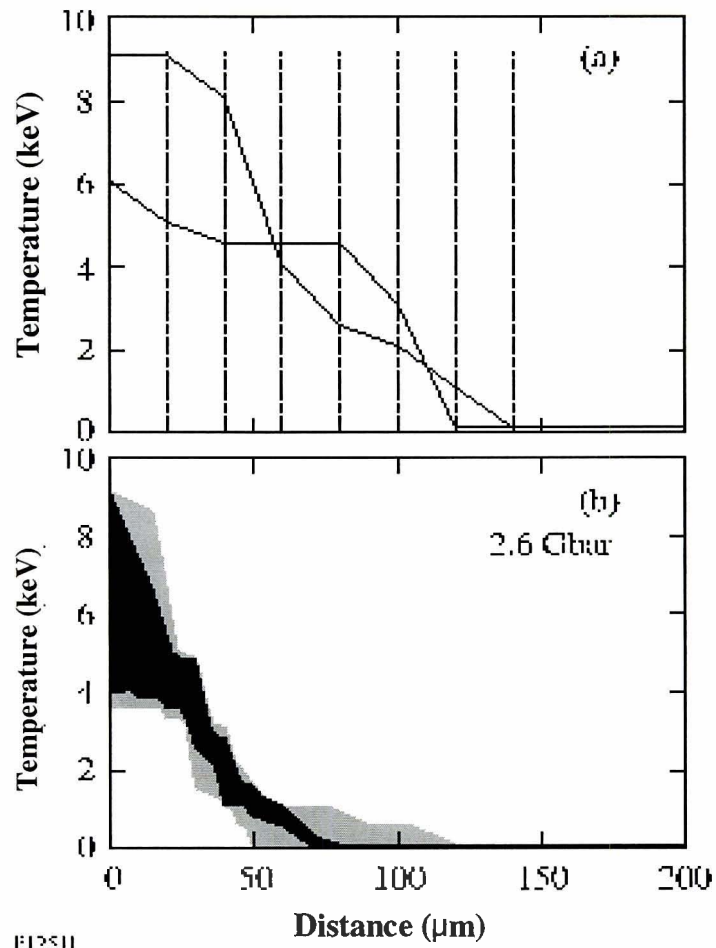


Figure 3: (a) The temperature grid with 250 eV temperature steps and a distance step of $20 \mu\text{m}$ as shown by the dots. The two lines represent monotonically decreasing temperature profiles produced as a function of distance and were used in core modeling.

(b) Temperature profiles in the light-shaded region that satisfy primary DD yield and neutron-averaged ion temperature and in addition secondary DT yield in the dark-shaded region are calculated at an electron pressure of 2.6 Gbar.

region of Fig. 3(b). This corresponds to temperature profiles that are consistent with the

measured DD neutron yield and neutron-averaged ion temperature. These profiles were passed on to the second stage, which eliminated all profiles inconsistent with the measured DT neutron yields. The black region in Fig. 3(b) indicates the results of the second stage calculations. These profiles are consistent with all neutron measurements, i.e. DD and DT neutron yields and the neutron-averaged ion temperature.

In the third stage of modeling similar profiles (as shown in Fig. 3) were constructed at different electron pressures ranging between 1 and 10 Gbar. It was found that only at pressures above 1.3 Gbar there are solutions which can produce the desired yields and ion temperatures. Examples of these solutions for particular pressures of 1.3, 2.6, 5.1 Gbar are shown in Fig. 4(a). It was found that the sizes of x-ray images are different for different pressures and therefore can be used to finally determine the temperature-density profiles consistent with all neutron and x-ray measurements.

The fourth stage of modeling was to compare calculated sizes of x-ray emission for different electron pressures and compare those with the experimentally measured core size. This is necessary to finally determine temperature and density profiles consistent with experimental x-ray images. Since it takes a significant amount of time to calculate the x-ray image from the given temperature and density profiles, only one representative x-ray image was calculated for each particular electron pressure. The examples of radial lineouts calculated for electron pressure 1.3, 2.6, and 5.2 Gbar [the same pressures shown in Fig. 4(a)] are shown in Fig. 4(b). The size of x-ray image is very sensitive to electron pressure. At a higher pressure the core size is smaller. The radii produced for 1.3, 2.6, and 5.1 Gbar were 130, 80, and 40 μm , respectively. This enabled us to narrow down the large range of temperature and density profiles (consistent

with neutron data) to a relatively narrow range consistent also with measured x-ray image.

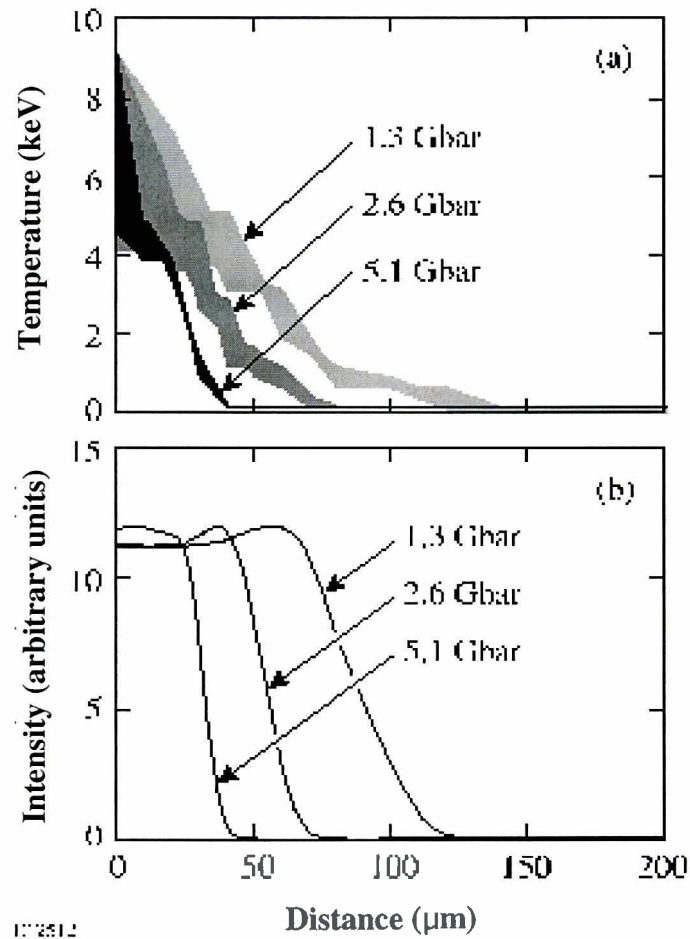


Figure 4: (a) Temperature profiles that match primary DD, secondary DT yields, and measured average-ion temperature at 1.3 (light), 2.6 (medium), and 5.1 Gbar (dark).
 (b) Examples of radial lineouts calculated for electron pressures of 1.3, 2.6 5.2 Gbar.

Figure 5(a) shows the image of the target in the shot 28900 at peak neutron production.

This image also shows lineouts through the center in two perpendicular directions.

Calculated radial lineouts that are most similar to the experimental ones are represented by the shaded region which corresponds to a range of electron pressures between 2.3 and 3.1 Gbar. Finally, the temperature and density profiles that most accurately correspond to the primary DD yield, the secondary DT yield, the neutron-averaged ion temperature, and the x-ray images can be seen in Fig. 5(b). Profiles in the light shaded region are the temperature profiles while those in the dark are the density profiles. As can be seen in Fig. 5(b), only a narrow range of the billions of temperature and density profiles that were originally generated by the computer program remained consistent with all neutron and x-ray measurements.

IV. Conclusion

For the first time, the density and temperature profiles of the compressed core of a cryogenic target at peak neutron production have been characterized. The core pressure was inferred to be between 2.3 and 3.1 Gbar based on experimentally measured primary DD and secondary DT yields, the average ion temperature, and core x-ray images. It is very important to understand these temperature and density profiles and their variations on neutron production. By measuring details of the core structure at peak neutron production scientists can adjust their target designs to achieve ignition in future experiments.

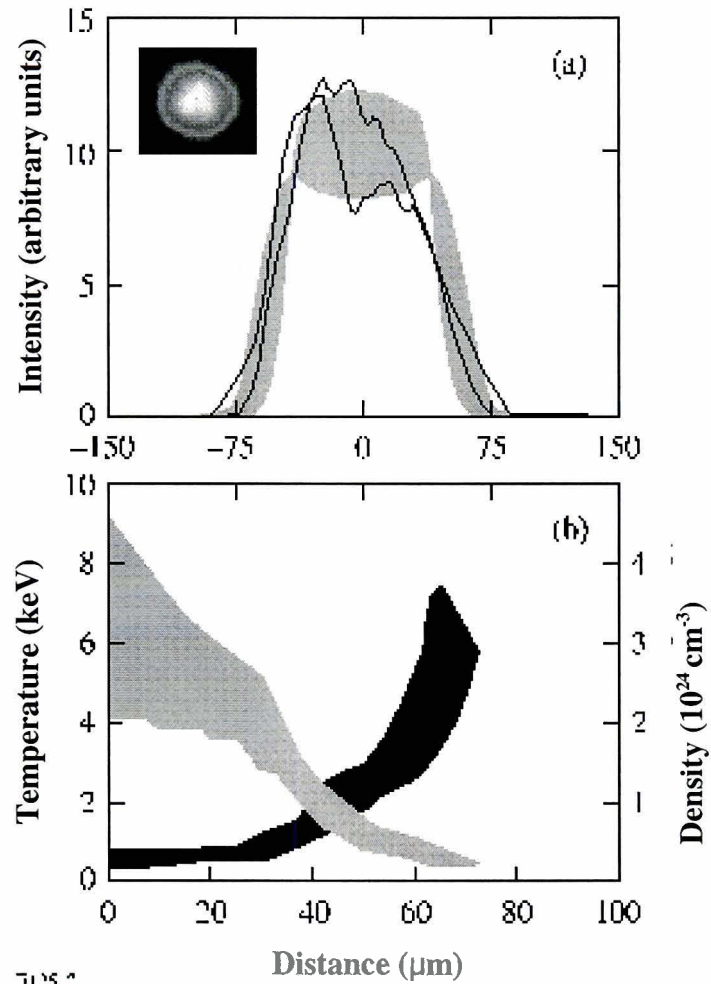


Figure 5: (a) The measured image of the target core at peak neutron production by the x-ray framing camera can be seen in the upper left quadrant. Thick and thin lines represent the horizontal and vertical radial lineouts of the experimental data while the shaded region corresponds to lineouts calculated at electron pressures of 2.3 and 3.1 Gbar. All lineouts were normalized to the same area under the curve.

(b) Core temperature (light-shaded) and density (dark-shaded) profiles that correspond to electron pressures from 2.3 to 3.1 Gbar that are consistent with the x-ray emission of the core image.

VI. Acknowledgments

Most importantly I would like to recognize my advisor Vladimir A. Smalyuk for his guidance and patience throughout this summer. His countless hours of assistance were greatly appreciated and allowed me to successfully complete my project and grow in a knowledgeable environment. Greatly appreciated was the assistance Sonya B. Dumanis gave to me on a daily basis. I would also like to show my appreciation to those who assisted me in completing my project including J. Delettrez, R. Epstein, V. Glebov, B. Radha, and C. Stoeckl. I would also like to thank Dr. Stephen Craxton for allowing me to participate in the Summer Research Program at the Laboratory for Laser Energetics and for reviewing this manuscript. Thank you.

VII. References

¹S. E. Bodner, D. G. Colombant, J. H. Gardner, R. H. Lehmborg, S. P. Obenschain, L. Phillips, A. J. Schmitt, J. D. Sethian, R. L. McCrory, W. Sekra, C. P. Verdon, J. P. Knauer, B. B. Afeyan, and H. T. Powell, *Phys. Plasmas* **5**, 1901 (1998).

²J. D. Lindl, *Inertial Confinement Fusion: The Quest for Ignition and Energy Gain Using Indirect Drive* (Springster, New York, 1998).

³T. R. Boehly, D. L. Brown, R. S. Craxton, R. L. Keck, J. P. Knauer, J. H. Kelly, T. J. Kessler, S. A. Kumpan, S. J. Loucks, S. A. Letzring, F.J. Marshall, R. L. McCrory, S. F. B. Morse, W. Seka, J. M. Soures, and C. P. Verdon, *Opt. Commun.* **133**, 495 (1997).

⁴T. C. Sangster, J.A. Delettrez, R. Epstein, V. Yu. Glebov, V. N. Goncharov, D. R. Harding, J. P. Knauer, R. L. Keck, J. D. Kilkenny, S. J. Loucks, L. D. Lund, R. L. McCrory, P. W. McKethy, F. J. Marshall, D. D. Meyerhofer, S. F. B. Morse, S. P. Regan, P. B. Radha, S. Roberts, W. Seka, S. Skupsky, V. A. Smalyuk, C. Sorce, J. M. Soures, C. Stoeckl, and K. Thorp, *Phys. Plasmas* **10**, 1937 (2003).

⁵P. W. McKentry, V. N. Goncharov, R. P. J. Town, S. Skupsky, R. Betti, and R. L. McCrory, *Phys. Plasmas* **8**, 2315 (2001).

⁶V. A. Smalyuk, J. A. Delettrez, V. N. Goncharov, F. J. Marshall, D. D. Meyerhofer, S. P. Regan, R. C. Sangster, R. P. J. Town, and B. Yaakobi, *Phys. Plasmas* **9**, 2738 (2002).

⁷V. A. Smalyuk, J.A. Delettrez, S.B. Dumanis, R. Epstein, V. Yu. Glebov, P. W. McKenty, D. D. Meyerhofer, P. B. Radha, T. C. Sangster, C. Stoeckl, N. C. Toscano, J. A. Frenjie, C. K. Li, R. D. Petrasso, F. H. Seguin, and J. A. Koch, “*Hot-Core Characterization of the Cryogenic D₂ Targets at Peak Neutron Production in Direct-Drive Spherical Implosion*”, submitted to Phys. Rev. Lett. (2003).

⁸S.P. Regan, J. A. Marozas, J. H. Kelly, T. R. Boehly, W. R. Donaldson, R. A. Jaanimagi, R. L. Keck, R. J. Kessler, D. D. Meyerhofer, W. Seka, S. Skupsky, and V. A. Smalyuk, J. Opt. Soc. Am. B **17**, 1483 (2000).

⁹T.R. Boehly, V. A. Smalyuk, D. D. Meyerhofer, J. P. Knauer, D. K. Bradley, R. S. Craxton, M. J. Guardalben, S. Skupsky, and T. J. Kessler, J. Appl. Phys. Plasmas **85**, 3444 (1999).

Photochemically Induced Alignment of Liquid Crystals on a Polymer Surface

Cam Tran

Photochemically Induced Alignment of Liquid Crystals on a Polymer Surface

Cam Yen Tran
Wilson Magnet High School

Advisor: Kenneth L. Marshall

University of Rochester
Laboratory for Laser Energetics
2003 Summer High School Research Program

1. Abstract

In the past, the accepted procedure of aligning liquid crystals on a polymer surface has been mechanical buffing, which is an inherently dirty process. In recent years, much research has been performed to discover a non-contacting way to photochemically align liquid crystals using linearly polarized light. The term “photobuffing” has been coined to describe this process. The goal of this research is to make liquid crystal alignment using the photobuffing technique as high quality as the alignment produced by the standard mechanical buffing technique. Using the linearly photopolymerizable polymer Staralign™ 2100 CP, which is manufactured by Vantico, and the nematic liquid crystal Merck E7, which is manufactured by EM Industries Inc., photobuffing experiments were performed in order to evaluate the capability of the photoalignment process. At this point, the quality of photoalignment does match that of the alignment due to mechanical buffing on a macroscopic scale, but because of the presence of light scattering features on the surface of the substrates, the quality of photoalignment on a microscopic scale is less than that of alignment produced by the mechanical buffing technique. Further research will need to be done before the photobuffing technique can be applied to laser and photonics applications.

2. Introduction

Liquid crystal alignment on polymer surfaces can be used for various device applications and thus it is a very important process in many fields of research and development. Mechanical buffing, also known as the rubbing technique, has been the standard procedure for aligning liquid crystals on polymer surfaces.¹⁻⁸ The coated substrate is moved back and forth underneath a buffing wheel covered in a velvet cloth. This cloth scratches the surface of the substrate and forces the polymers on the surface to align. Although mechanical buffing has been used for many years, this technique is inherently flawed in that it is a very dirty process. The buffing wheel embeds dirt particles on the surfaces with which it comes into contact and causes an electrostatic charging that attracts even more particles. It is also a time-consuming trial and error process in which the buffing wheel must be adjusted to a height where it barely touches the surface of the substrate. Photochemically induced alignment, or “photobuffing,” is a technique that could potentially replace mechanical buffing as the standard technique of alignment. It is a non-contacting way of aligning liquid crystals in which the only thing that comes into contact with the polymer surface is light, which does not leave any particulate matter at all. This could save a great deal of time and money in manufacturing liquid crystal devices and could potentially change the way that all LC devices are assembled.

3. Experimental⁹

Glass substrates were cut from glass cover slides and ITO substrates were obtained. They were then cleaned in the ultrasonic bath, hand-scrubbed using Texwipe[®] MiracleWipes[™] and deionized water, dried off with a nitrogen air gun, and heated at 110°C for 90 minutes in order to remove any left over solvent. Approximately 2 ml of the linearly photopolymerizable

polymer Staralign™ 2100 CP was placed on the spin coater and a crystallization dish was placed over it in order to trap the vapors and saturate the surrounding air with the solvent. Each substrate was then flooded with Staralign™ 2100 CP, left to sit for 30 seconds, and spun at 3000 RPM for 60 seconds. The substrates were then hard baked at 130°C for 10 minutes. They were allowed to cool off for about 5 minutes and were then placed inside of a polarizer box equipped with an Oriel dichroic polarizer. The polarizer box was placed into a Rayonet chamber and the substrate was exposed to vertically polarized 300 nm UV-light for 10 minutes.¹⁰ When each substrate was removed from the polarizer box, a mark was made on the upper right hand edge of the substrate. Each time an ITO cell was assembled, two substrates were obtained and were glued together anti-parallel to one another with the mark serving as an indicator to the orientation of the substrate. UV-epoxy containing 22 μm spacers, a cell assembly mount, and a mercury vapor lamp were used to assemble the cells. The cells were left underneath the mercury vapor lamp for 60 seconds to harden the UV-epoxy. The glass cells were assembled in the same fashion using the same materials, except, instead of the cell assembly mount, the cells were put together manually. After the cells were assembled, they were filled vertically with the nematic liquid crystal Merck E7. The cells were then sealed with 5-minute epoxy and left to dry. After the cells dried off, they were cleaned with acetone and labeled.

A few photobuffing experiments were performed using a Nissan 610 polyimide in order to see if the polyimide would photochemically align. First the ITO substrate was flooded with a polyimide solvent, left to sit for 30 seconds, and spun at 3500 RPM for 60 seconds. Each substrate was then flooded with a polyimide solution made out of a 1:2.5 ratio of polyimide solute to polyimide solvent, left to sit for 60 seconds, spun at 3500 RPM for 120 seconds, soft

baked at 80°C for 10 minutes, and then hard baked at 250°C for 60 minutes. The irradiation and assembly procedures were the same as for the Staralign material.

4. Results

The initial results of this experiment were very poor, but at this point in time, the quality of photoalignment matches that of the mechanical buffing technique on a macroscopic scale only. As can be seen in Figure 1 and Figure 2, the quality of alignment of the photobuffing and mechanical buffing technique are almost equal to one another. The photobuffed cells show good contrast, which means that there is a well-defined transition between polarization states and that

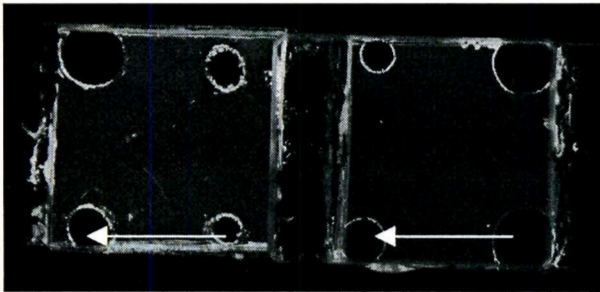


Figure 1: Photobuffed cell (left) and mechanically buffed cell (right) aligned with one of the axes of the crossed polarizers.

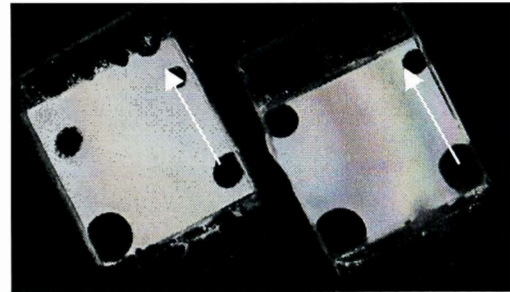


Figure 2: Photobuffed cell (left) and mechanically buffed cell (right) tilted 45° to one of the axes of the crossed polarizers.

the liquid crystals are aligned. (White arrows indicate direction of polarization or rub direction depending on the cell being observed.) The various colors seen in the cells in Figure 2 indicate that there is a disparity in the thickness of the cell gap across the cells. Other than this problem, the quality of the cells is very high and macroscopically, the buffed and photobuffed cells are identical. Microscopically, there are still some defects with the photobuffed cells that need to be fixed. The presence of light scattering features, such as ridges in the polymer coating, prevents the microscopic quality of photoalignment to equal that of mechanical buffing. As can be seen

in the following pictures, the mechanically buffed cell is relatively smooth. Other than a few specs of dust and the scratches caused from rubbing the surface with the velvet buffing cloth, the buffed cell has no major defects on its surface as can be seen in Figure 3 below. The photobuffed cell, on the other hand, has microscopic ridges on the surface that disrupts the alignment in those areas as can be seen in Figure 4.

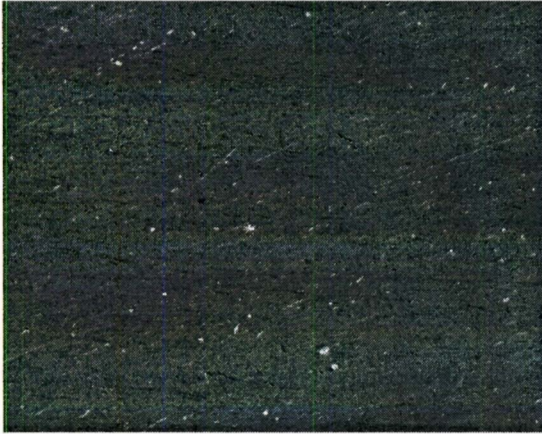


Figure 3: Microscopic surface of a rubbed polyimide cell.

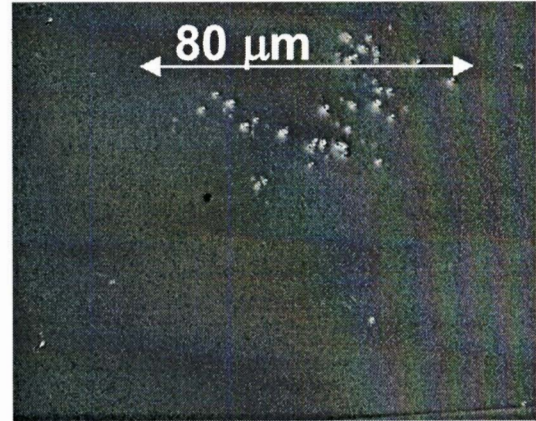


Figure 4: Microscopic surface of a photobuffed Staralign cell.

5. Discussion and Conclusions

The photobuffed cells were of poor quality due to the rapid evaporation of the Staralign solvent. In certain areas of the cells, the solvent was evaporating too quickly and so ridges of the solvent formed from the uneven evaporation. In order to make the solvent less volatile, a small amount of the solvent was placed on the spin coater and then the spin coater was covered in a crystallization dish. This would allow for the solvent to saturate the surrounding air, which would prevent the solvent later placed on the substrates themselves from evaporating too quickly. This resulted in a much smoother surface as opposed to the types of surfaces seen in Figure 4 above.

In any case, alignment can be obtained photochemically. The quality of alignment of the nematic liquid crystals produced by the photobuffing technique was equal to that of the alignment produced by the rubbing technique macroscopically. At this point, the process can be used for low power applications that do not require the cells to be perfectly aligned. Microscopically, there are more defects that must be removed before the photobuffing process can be used for photonics and laser applications.

6. Future Studies

More research will need to be performed in order to achieve the same high level of alignment on a microscopic scale. Experiments will also be performed using other liquid crystals, including smectic, chiral, and cholesteric liquid crystals, in order to ensure that the process can be used for a wide range of applications.

7. Acknowledgements

The author would like to thank everyone who has made this research possible. The author would like to first thank the University of Rochester's Laboratory for Laser Energetics, for their generosity in running the Summer Research Program for High School Juniors. She would also like to thank Dr. R. Stephen Craxton for giving her this opportunity to be a part of such cutting edge research. Special thanks go to Kenneth L. Marshall for his supervision and guidance throughout the entire duration of the program. The author is also very grateful to the Materials Optics Lab staff and students who worked with her on a day-to-day basis: Jennifer Jung, Brett Klehn, Benjamin Kolodzie, Benjamin Schudel, Joann Starowitz, and Elizabeth Wolcott. Without the help of all of you, this project would not have been possible.

References

1. M. E. Becker, R. A. Kilian, B. B. Kosmowski and D. A. Milynski, *Mol. Cryst. Liq. Cryst.*, **130**, 167 (1986).
2. J. M. Geary, J. W. Goodby, A. R. Kmetz and J. S. Patel. *J. Appl. Phys.*, **62**, 4100 (1987).
3. A. Moseley, B. M. Nicholas and P. A. Gass. *Displays*, **8**, 142 (1987).
4. R. W. Filas and J. S. Patel, *Appl. Phys. Lett.*, **50**, 142 (1987).
5. K. Yoshida, H. Fukuro and S. Kobayashi. *Proc. Of the SID*, **28**, 755 (1987).
6. S. Kuniyashu, H. Fukuro, S. Maeda, K. Nakaya, M. Nitta, N. Ozaki and S. Kobayashi. *JPN. J. Appl. Phys.*, **27**, 827 (1988).
7. H. Fukuro and S. Kobayashi, *Mol. Cryst. Liq. Cryst.*, **163**, 157 (1988).
8. T. Sugiyama, S. Kuniyasu, D. S. Seo, H. Fukuro and S. Kobayashi, *Jpn. J. Appl. Phys.*, **29**, 2045 (1990).
9. B. P. Kolodzie (private communication).
10. *Technical Data Sheet Staralign™ 2100*, Vantico AG, Division Optronics, VS OPAL, Optical Performance Alignment Layers, Switzerland.

The Effect of Nonuniform Illumination on the Shape of Deuterium Ice Layers

Michael Wozniak

The Effect of Nonuniform Illumination on the Shape of Deuterium Ice Layers

Michael Wozniak
Greece Athena High School
Rochester, NY

Advisors: R. Stephen Craxton, David Harding
Laboratory for Laser Energetics
University of Rochester
Rochester, NY

The Effect of Nonuniform Illumination on the Shape of Deuterium Ice Layers

Abstract

Inertial confinement fusion requires the use of a uniformly thick target for best efficiency. Cryogenic targets are used in this process because deuterium ice has a higher density than deuterium gas, allowing more fuel in the target. These cryogenic targets are formed in a device called the layering sphere, which freezes the deuterium target to about 18 Kelvin, initially in a nonuniform layer. The target is then heated several millikelvin with a fiber-optic light source. This light is reflected throughout the layering sphere and deposited in the ice causing the thicker ice to vaporize and accumulate on the thinner parts. This process continues until the ice is uniformly thick with an isothermal inner surface. A problem associated with this layering process is that the illumination is not uniform because there is a “keyhole” in the layering sphere that is used to insert and extract the target. This nonuniformity in the illumination causes perturbations in the ice layer. The nonuniformities were modeled by first calculating the energy deposited in the ice due to a single beam of light using a PV-Wave code. The calculated energy deposition was then used in a computational fluid dynamics program called FLUENT, which was used to find the shape of the ice layer due to the keyhole. These perturbations due to the keyhole have been calculated to be about $5 \mu\text{m}$ (rms) in a 1-mm-diameter shell with an ice thickness of $100 \mu\text{m}$.

1. Introduction

Fusion occurs when two atoms are compressed close enough together that their nuclei collide and combine to form a single atom.¹ This reaction releases energy,

which is due to a conversion of mass into energy. The ideal fuel source for fusion is deuterium-tritium due to its high energy yield, but it is not used in most experiments because it is radioactive. Because of this, most fusion experiments use a deuterium-deuterium fuel source. Fusion is beneficial because the fuel source can be extracted from seawater, the product of the reaction is a nonradioactive inert gas, and fusion has the potential to produce a lot of energy.

One type of fusion is inertial confinement fusion, which uses an immense amount of power to rapidly heat a target to very high temperatures where fusion can occur. At the University of Rochester, this is done with the 60-beam Omega laser system. There are two types of targets that are used in this system: gas targets and cryogenic targets. The gas targets are easier to make, but they do not provide as much fuel and they are less dense. Cryogenic targets are deuterium-filled targets that have been frozen. Cryogenic targets are used in inertial confinement fusion because deuterium ice is a denser fuel source than deuterium gas. The fusion process is most efficient if the fuel source is compressed as much as possible, because the atoms are closer together and so more fusion collisions occur. The targets must be uniform to be compressed efficiently. The purpose of this research was to model one source of ice layer nonuniformity that had previously been ignored.

Cryogenic targets are created by filling a 3 micron thick plastic shell (1-mm diameter) with deuterium gas to several thousand atmospheres by permeating the gas through the shell. The temperature of the target is then dropped to about 18 Kelvin, which causes the deuterium gas to solidify.² The deuterium ice forms a layer, which is initially nonuniform due to gravity: the bottom of the target has a much thicker layer than

the top. This nonuniform ice layer is then modified using a device called the layering sphere (see Fig.1). The layering sphere has a rough surface, which is gold plated so that it reflects the light very well. The layering sphere uses an infrared laser source aimed at the rough surface, which causes the light to be scattered throughout the layering sphere which allows the target to be illuminated from nearly all angles.

This illumination heats the deuterium ice several millikelvin. The thicker portions of the deuterium ice become

hotter than the thinner portions, and because the target is kept very close to the triple point of deuterium, the deuterium sublimates from the hotter (thicker) portions and deposits on the cooler (thinner) portions. With perfect illumination uniformity, this process will lead to a perfect cryogenic target, which will have a uniformly thick ice layer³ (see Fig.2)

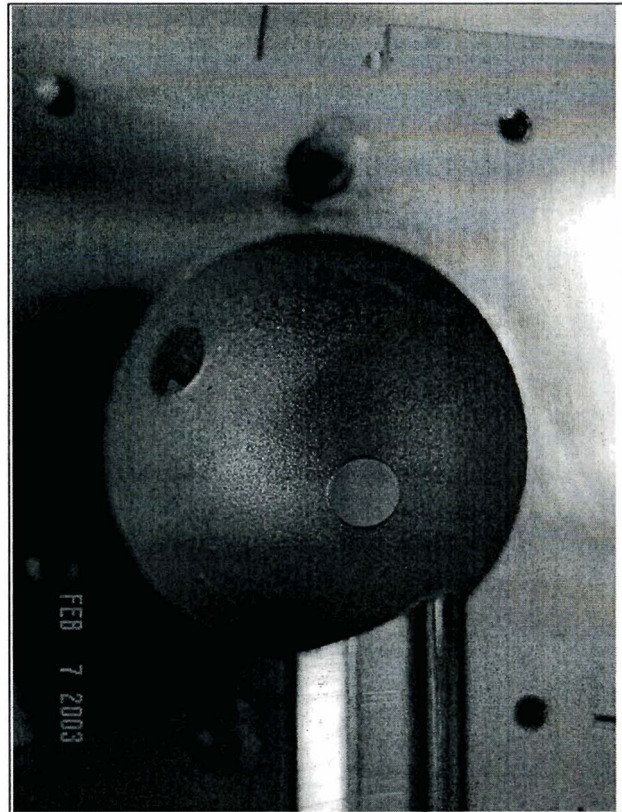


Figure 1: Picture of half of the layering sphere (diameter = 1 inch). The two holes are viewing windows. The keyhole is the shiny part at the bottom of the picture and the shadow created by x rays can be seen at the top of the picture.

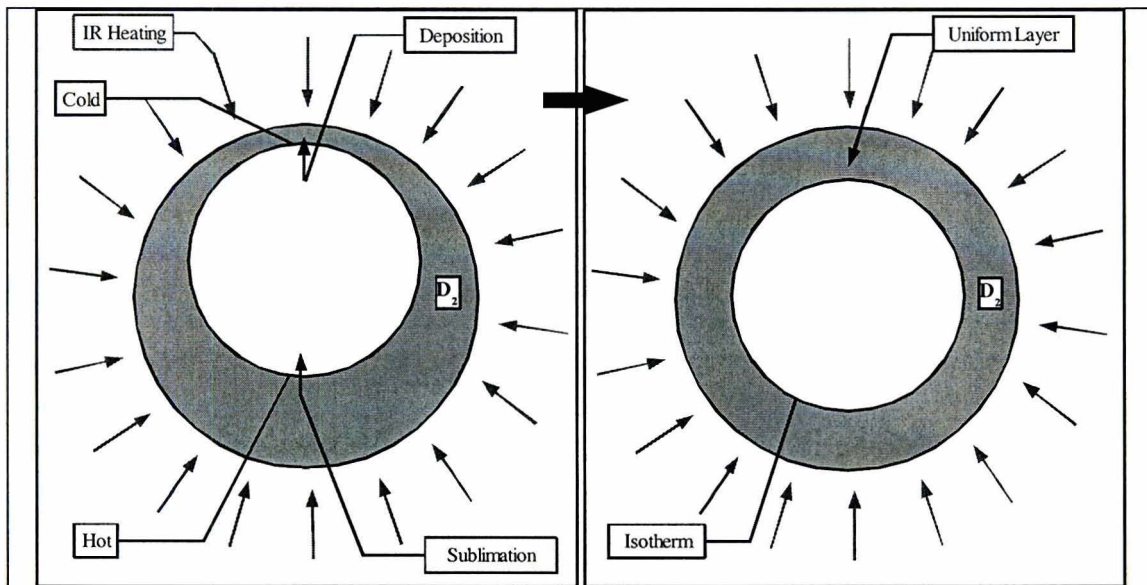


Figure 2: Uniform ice layers are formed using infrared heating. This infrared illumination is absorbed by the deuterium ice in the target. The thicker portions of the ice absorb more energy, creating a hotter surface. The thinner portions of the ice absorb less energy, creating a colder surface. The temperature difference between the hotter and colder portions of the ice is enough to cause the ice to sublime from the hot portions and deposit on the cold portions. This process continues until the entire inner ice surface is an isotherm. With perfect illumination uniformity, the result is a perfect target.

The layering sphere does not provide perfect illumination uniformity. The infrared radiation illuminates the target from all angles except from the points where there are nonuniformities in the layering sphere. These nonuniformities include four viewing windows, a keyhole, and the shadow of the keyhole. The viewing windows are used to monitor the progress of the layering of the deuterium ice in the target. The keyhole is a hole in the bottom of the layering sphere, which is used to extract the target just before it is shot by the Omega laser system. The shadow of the keyhole is created by x rays that are emitted during an Omega shot, go through the keyhole, and ablate the gold from the surface at the top of the layering sphere. This creates a region that does not reflect or scatter light as efficiently as other regions.

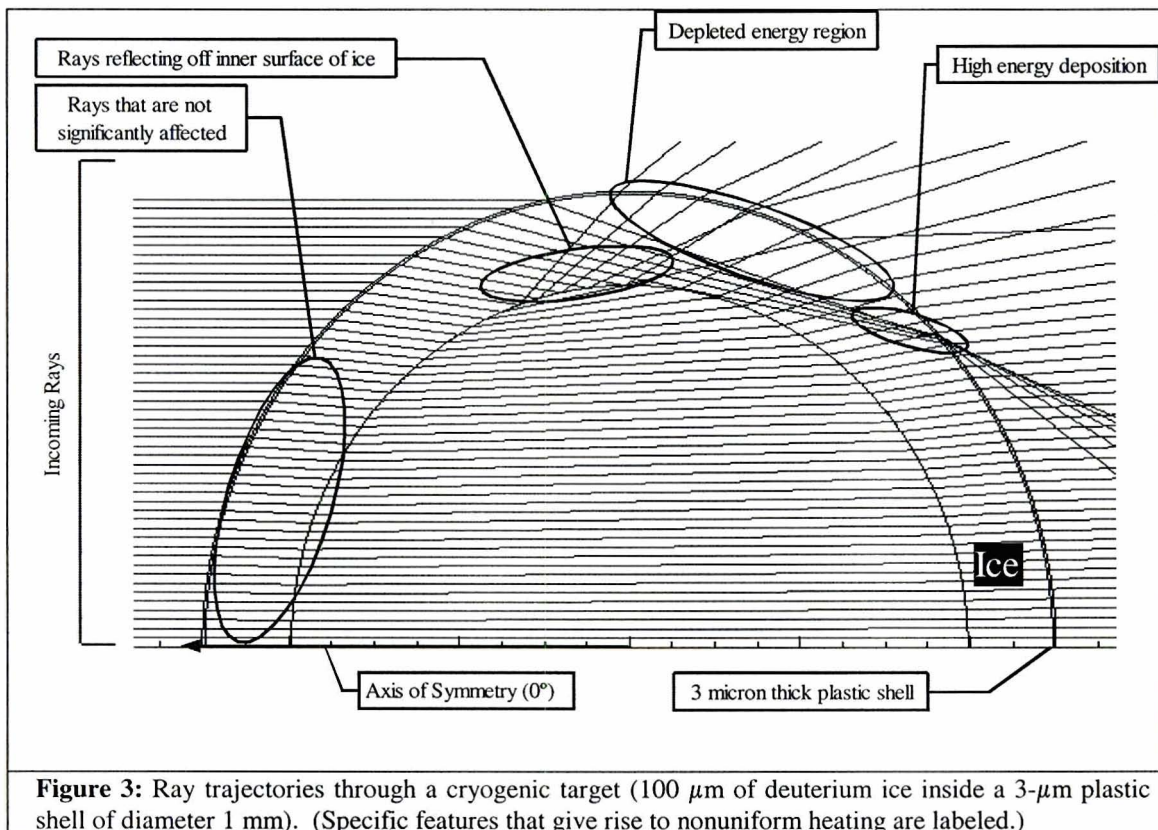
The effect of the keyhole on the ice thickness uniformity was modeled in

two steps. First, a code that calculated the path of light rays through a target was modified to find the energy deposition in the target. Then, a computational fluid dynamics code called FLUENT was used to model the thermal conduction and calculate the final ice layer thickness nonuniformity. Previously, it was assumed that a perfect ice layer could be achieved if the target was placed in the layering sphere for a long enough time in the absence of other sources of nonuniformity. This model has shown that the best possible ice thickness uniformity is about $5 \mu\text{m}$ in a target with ice that is $100 \mu\text{m}$ thick and 1 mm in diameter.

2. Modeling the energy deposition

The effect of the keyhole was modeled by calculating the energy absorbed by the target for the case of uniform illumination and then subtracting the energy distribution due to a single ray trace (see Fig.3). The energy due to the ray trace was scaled to account for the size of the keyhole. This model assumed that the energy distributed into the target was axisymmetric and that the windows and shadow of the keyhole had no effect on the illumination uniformity. The keyhole represents the dominant nonuniformity in the layering sphere as its solid angle (2.141% of the total surface area) is approximately equal to the total solid angles of the four viewing windows. The model was based on a target that was 1 mm in diameter, had an ice thickness of $100 \mu\text{m}$, and a shell thickness of $3 \mu\text{m}$. The amount of energy absorbed by the target was assumed to be approximately the same as is produced through radioactive (beta) decay by a deuterium-tritium target of the same size ($5 \times 10^4 \text{ W/m}^3$).⁴

At each interface in the target, the light rays are refracted (see Fig.3). The light refraction was modeled with a computer program written in PV-Wave, based on the program described in Ref. 5. The model was based on a single beam of light aimed at the target. The beam was separated into many rays that were each calculated separately. The path of each ray of light was calculated using Snell's Law to find the angle through which the light was refracted. The program also calculated the reflection of some of the rays from the inner surface of the ice layer. These rays were reflected because when a



ray strikes the inner surface of the ice at an angle close to that which would cause the ray to be totally internally reflected, the Fresnel coefficients show that the majority of the energy of the light ray is reflected.⁵

From Fig. 3 it is seen that the energy from a single beam of light is not deposited uniformly throughout the ice layer. Three regions of nonuniform energy deposition are indicated in Fig. 3: a region where rays reflect off the inner surface of the ice, a depleted energy region, and a region where there is focusing of the light rays. The rays that reflect off the surface of the ice cause a higher energy deposition in that region of the ice because it is being heated from two separate sets of rays. The depleted energy region only receives energy from a few rays that are reflected off the inner surface of the ice; these rays are spaced out, which causes less energy to be deposited. The region where light rays are focused has rays that overlap and cause a high energy deposition.

A calculation of the energy deposited by the light rays was added to the ray-trace program. Each ray that was traced was assigned an extra parameter, which holds the amount of energy that the ray represents. Each ray represents an area of the light beam, and carries an amount of energy proportional to this area. The energy that is deposited in the ice by each ray is then calculated based on the absorption coefficient of deuterium ice, which is 4 cm^{-1} for the wavelength of the light source ($3.16 \text{ }\mu\text{m}$) used in the layering sphere. The energy from each ray is then added to a grid that represents the ice layer. Since each cell on the grid does not represent the same volume, the energy at each point on the grid is divided by the cell volume to give the absorbed energy per unit volume (see Fig.4). The labeled regions from Fig. 3 are labeled again in Fig. 4 to show the effects each feature had on the energy distribution: the focused light rays caused high energy deposition and the depleted energy region had very low energy deposition as expected based on Fig. 3.

The large number of grid cells are then divided into a smaller number of

zones by averaging cells whose energy per unit volume differ by less than 10% (see Fig.5). The absorbed energy in these zones formed the basis for the next stage of modeling.

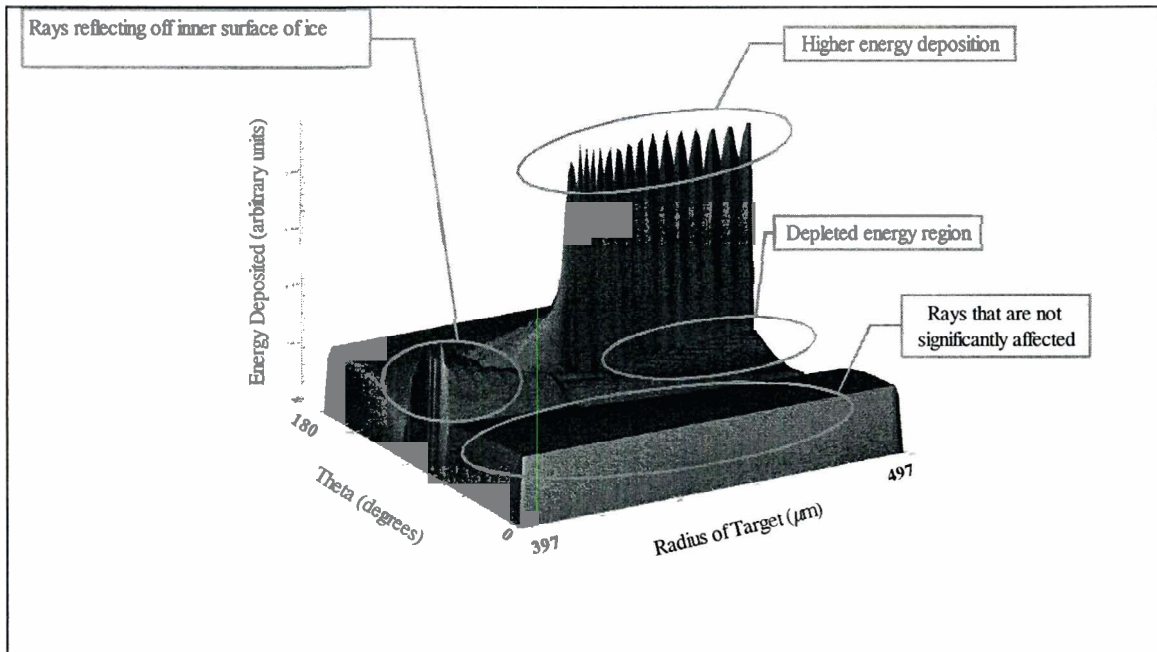


Figure 4: Energy per unit volume deposited in the ice of the target due to the ray trace. As in Fig. 3, the regions experiencing nonuniform heating are labeled.

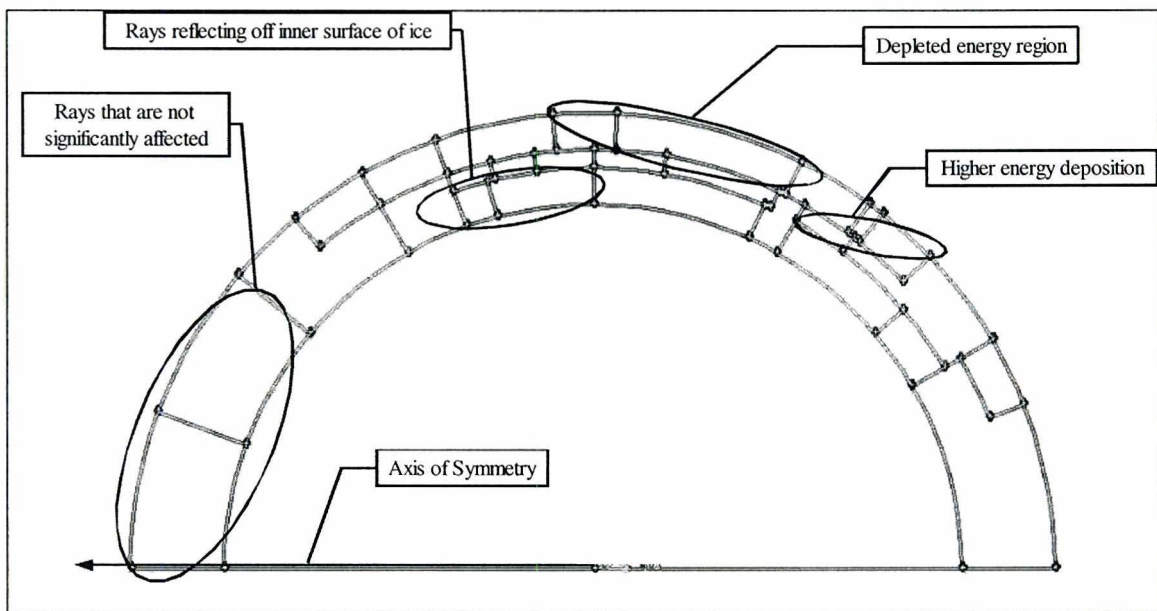


Figure 5: Wireframe created in GAMBIT corresponding to Fig. 3. The zones were created by averaging cells from the energy distribution grid that differed by less than 10%.

3. Modeling the Ice Layer Thickness

In order to determine the shape of the deuterium ice layer due to the energy absorbed in the layering process, an iterative process is used. This process begins with a uniformly thick ice layer, for which the temperature contours resulting from the given absorbed energy are calculated. The temperature along the inner ice surface is then analyzed; the portions of the ice that are relatively hotter are modified to be thinner and the portions of the ice that are relatively colder are modified to be thicker. The relationship between ice thickness and temperature is based on the results of Ref. 6. The temperature contours are recalculated and the process begins again with a new ice shape. When the inner ice surface becomes an isotherm after several iterations, the final ice shape has been achieved. This is because when the ice surface is an isotherm, if any parts of the ice layer sublimate or if there is any deposition, then it will be uniform throughout the target and will not affect the shape.

This process is done manually with the aid of two software packages. GAMBIT⁷, a wireframe mesh generator, was used to create a mesh to represent the cryogenic target. This mesh was exported to FLUENT⁸, a computational fluid dynamics code. FLUENT was used to calculate heat transfer through the cryogenic target and thus the temperature contours.

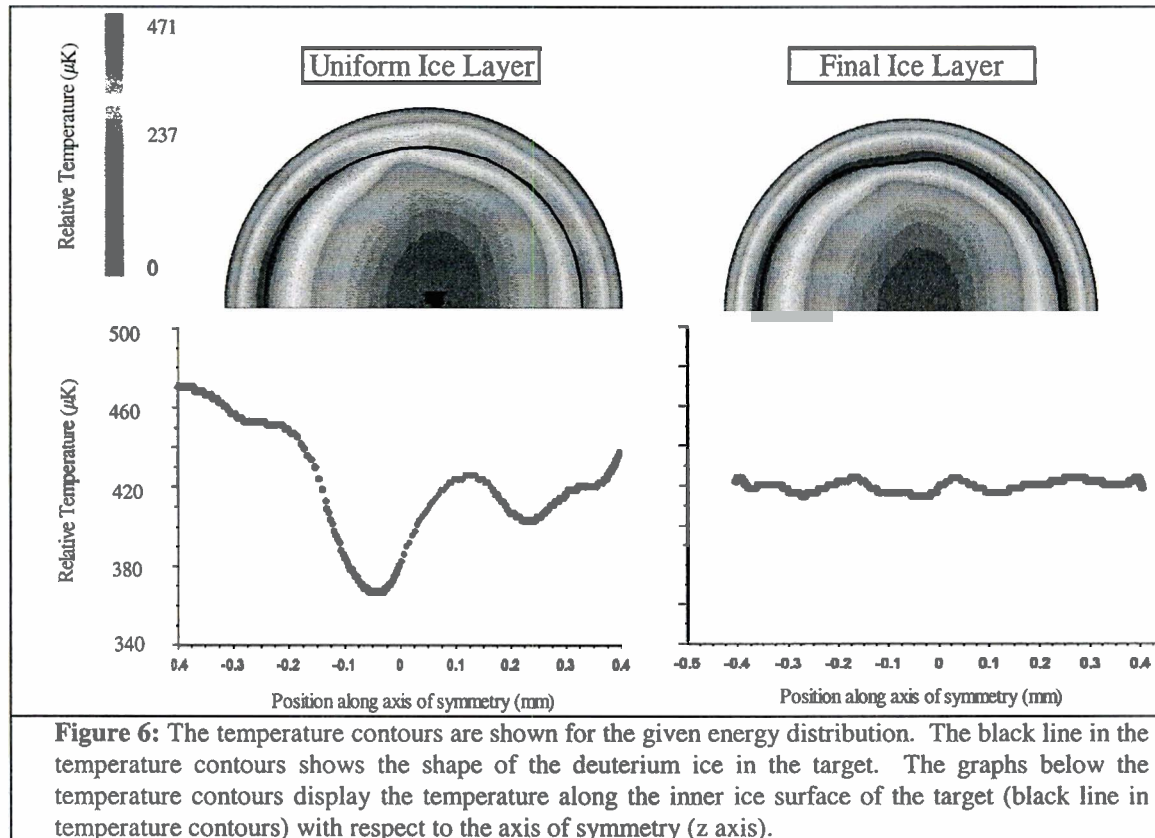
First, GAMBIT is used to create a wireframe mesh that represents a target with a uniformly thick ice layer and zones that correspond to those that were calculated from the energy deposition. GAMBIT then fills in the large zones with small meshes that help FLUENT perform calculations. The mesh that represents the target is then exported

to FLUENT where the values for the energy deposited into the ice are entered. The boundary conditions also have to be entered into the program. These boundary conditions include an isothermal outer layer on the target, which is set at 18K. The inner ice surface is coupled to the outer surface of the deuterium gas on the inside of the target. There is some deuterium gas inside the ice layer because some of the solid deuterium vaporizes. The deuterium gas is given an energy value of 50 W/m^3 , which is the amount of energy that was assumed to be absorbed by the deuterium gas in the target. The physical constants of deuterium ice and deuterium gas are entered into the materials section of FLUENT (see Table 1).

FLUENT first solves (by iterating 500 times) for the temperature contours that result from a uniform ice

	D ₂ ice	D ₂ gas
Density (kg/m ³)	195	0.452
Heat capacity C _p (J/kg K)	2950	5200
Thermal conductivity k (W/m K)	0.38	0.009

layer. FLUENT displays the temperature contours and the temperature along the inner surface of the ice with respect to its position along the z axis, the axis of symmetry (see Fig. 6). The graph of the temperature along the inner surface of the ice is used to determine how the shape of the ice layer should be changed. This process is done manually by trial and error. The areas on the inner ice surface that are hotter are modified to be thinner and the colder areas are modified to be thicker. Using the new ice surface, the wireframe mesh in GAMBIT is changed. It takes about ten iterations of calculating the temperature contours to achieve a nearly isothermal inner ice surface. The temperature of the inner ice surface was considered to be isothermal when it was within a range of 15 to 20 microkelvin. This is illustrated in the right hand portion of Fig. 6.

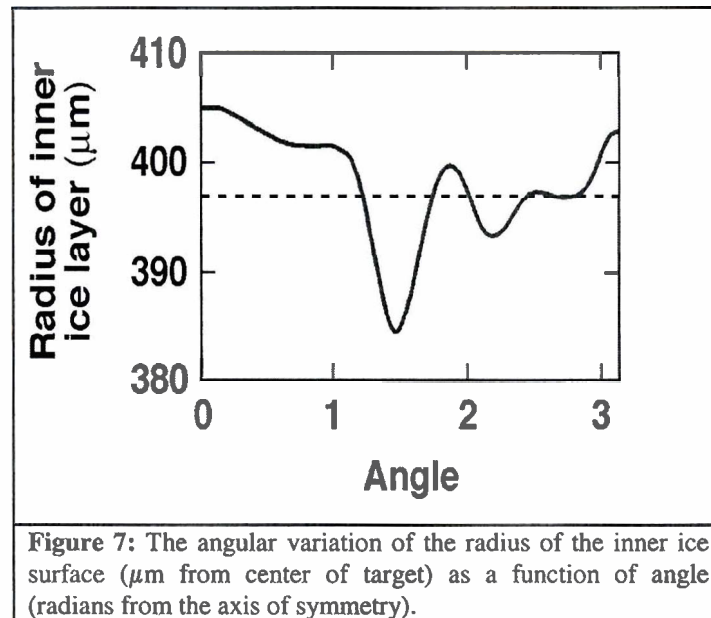


4. Discussion

The final shape of the ice layer in the cryogenic target (see Fig.7) reveals that the nonuniform illumination of the layering sphere has a significant effect on the uniformity of the ice thickness in the target. The effect of the keyhole in the layering sphere induces a $5 \mu\text{m rms}$ ice roughness in the final shape of the ice. This is comparable to the experimentally measured roughness ($2\text{-}3 \mu\text{m rms}$) of the best targets that have been created to date.

The main feature seen in Fig. 7 is a large increase in the ice thickness (smaller inner radius), which occurs near 1.5 radians. The cause of this feature is most likely due to the area shown in Fig. 3 that is heated by two sets of rays, one set that goes through the area directly, and another set that reflects off the inner surface of the ice. This

causes an increase in ice thickness, because the calculated energy distribution was subtracted due to the lack of heating from the keyhole.



The difference between modeled and experimental results is most likely due to the assumptions that were made for this model. One possible explanation is that the energy that would come from the keyhole has a larger angular spread than the calculations assumed. However, this is unlikely to have much of an effect on the uniformity. Alternatively, the viewing windows and the shadow of the keyhole may have some effects that counteract the effects of the keyhole. This is also unlikely because these other features would probably contribute to more nonuniformities in different positions. To model these, a more extensive three-dimensional model must be created that can account for all the nonuniformities of the layering sphere. Also, the empirical results of 2-3 μm rms could be low because the measurement technique does not sample all parts of the target. The empirical measurements may not detect the largest feature shown in Fig. 7. Finally, inaccuracies may be introduced through the way that information is transferred to

FLUENT. The energy values that are imported to FLUENT have a low resolution; a model using a finer wireframe than shown in Fig. 5 would show if this affects the results significantly.

5. Conclusion

The effect of the keyhole in the layering sphere on the ice thickness uniformity of cryogenic targets has been modeled for the first time. The energy that is deposited due to a single beam of light was calculated using a PV-Wave code. The output of this code was then exported to FLUENT, which was used to find the shape of the ice layer due to the keyhole. The model predicted thickness nonuniformities of $5 \mu\text{m}$ rms that are consistent with empirical data considering the assumptions that were made. This shows that there is a limit to the thickness uniformity of a cryogenic target produced in the layering sphere. Because of the importance of uniform targets to inertial confinement fusion, more accurate calculations and further experiments must be done in the future.

6. Acknowledgements

I would like to thank Dr. Craxton for providing me with the opportunity to participate in the University of Rochester's Summer Research Program. I would like to thank my advisors, Dr. Craxton and Dr. Harding for assisting me with my research throughout the summer. Also, I would like to thank the other students in the research program for being so supportive and making the entire summer enjoyable.

7. References

1. Craxton, R. Stephen, Robert L. McCrory, and John M. Soures, *Scientific American*, Volume 225, pp. 68-79, "Progress in Laser Fusion (August 1986)."
2. Laboratory for Laser Energetics Report LLE-02422, October 2001, Section 2.8, "Target Development and Production."
3. Laboratory for Laser Energy Report LLE-02422, October 2001, Section 2.9, "Cryogenic Target Handling System."
4. J. K. Hoffer and L. R. Foreman, *Phys. Rev. Lett.* **60**, 1310 (1988).
5. Sharon Jin, "A Ray-Tracing Model for Cryogenic Target Uniformity Characterization," 2002 Summer High School Research Program for High School Juniors, Laboratory for Laser Energetics Report 329 (2003).
6. E. L. Alfonso, I. Antemy, and D. R. Harding, *LLE Review*, Volume 81, pp.12-20, "Modeling the Temperature and Ice-Thickness Profiles Within OMEGA Cryogenic Targets" (1999).
7. Gambit Version 2.0, produced by Fluent Inc., Lebanon, NH.
8. Version 6.0, Fluent, Inc., Lebanon, NH.